Charged Particle Transverse Momentum Spectra in Positron Proton Collisions at the H1 Experiment

Thesis submitted in accordance with the requirements of the University of Liverpool for the degree of Doctor of Philosophy

by

Theodore Cosmo Holtom

July 1998

Oliver Lodge Laboratory
University of Liverpool

Charged Particle Transverse Momentum Spectra in Positron Proton Collisions at the H1 Experiment

Theodore Cosmo Holtom

Abstract

Charged particle transverse momentum spectra arising from deep inelastic scattering of positrons and protons at a centre of mass energy, $\sqrt{s} = 300.9 GeV$ are presented in the kinematic region ranging from $5 - 50\, GeV^2$ in Q^2 and from $10^{-4} - 10^{-2}$ in Bjorken-x. The data are compared with Monte Carlo predictions using the Matrix Element plus Parton Showers (MEPS) model and the Colour Dipole Model (CDM). It is shown that at low x the data clearly exhibit preference for the CDM predictions. The data are also shown to favour a BFKL calculation towards low x. It is noted that the onset of BFKL effects, and the ensuing non-ordering of partonic k_T, in the low x regime at HERA could explain these results. Predictions based upon the DGLAP formalism fail to describe the spectra in the low x regime.

Acknowledgements

I would like to express deep gratitude to my supervisor “Uncle” Professor Erwin Gabathuler, respected and feared throughout the High Energy Physics community, for this opportunity to study in the fascinating field of particle physics, and for his supervision. Despite the inevitable difficulties and trials which contribute to the value of a PhD the whole experience has been very rewarding and, at the end of it now I know I will look fondly back at my time at Liverpool University and in Hamburg at the DESY laboratory.

I must thank the Particle Physics and Astronomy Research Council for its financial support. I would also like to express appreciation for the British taxpayer, who, demonstrating what must be considered civilisation, ultimately funds fundamental science.

I would like to acknowledge the effort of the whole of the H1 Collaboration of which I have proudly been a member. I must take this opportunity to thank Michael Kuhlen, Stephen Burke and David Cussans in particular who I have had the pleasure of working closely with and who have provided much guidance in the production of this study. The Liverpool H1 group have been very helpful as well and so I would like to thank Steve and Tania McMahon, Girish Patel, Mark Oakden, Julian Phillips, Roland Martin, Tim Greenshaw and especially Steve Maxfield, who have all provided help at various times and have also been a pleasure to work with.

Great thanks to all my office mates for providing help and amusement throughout the course of my PhD. It has been great fun working with you, though rather smelly at times. Big Christopher “Godzilla” Cormack, Mark “the Bear” Smith, Hugh “Telephone Manner” Tallini, Stuart “Database” Cocks, Mike “Animal” McAndrew and “Cheeky” Dave Milstead - I wish you all the best and plenty of physics to come. Greetings also to Julia Cowell, Chris Green, Angela Benelli, Gavin McPherson, Moshe Hanlon, Socrates Kiourkos, Dominic Duxbury, “Hermann the German” Ulrich Parzefall and “Nuclear” Roger Allatt, fellow PhD students at Liverpool.

I would like to thank my family and friends for putting up with the “eternal student” and believing me every time I said that I would be submitting my thesis the following week. Dad, Hannah, Catherine, Christien, Rosie - it has finally happened! Life is going to be strange for a while adjusting from the nocturnal existence of a PhD student, in the office at all hours (though perhaps not at 9 a.m.) and seven days a week. My good friends, “the Boys”, Mr. “Jungle Hair” Leo, Mr. “Moneybags” Richard, Mr. “Perfect” Simon and Mr.(soon Dr. himself no doubt, the copycat) “Logical Spock” Anthony - perhaps I will be able to afford to buy you a beverage of your choice now. In the words of my first year statistics lecturer, Spiros, from Greece: “You are eegnorant! Thees ees treevial!”.

I wish to thank my sweet mother, who, despite not being particularly of the scientific bent (she has trouble with a pocket calculator!), always taught me to read and encouraged me in my education as a child. She has been an inspiration.

Finally, words cannot express how much I owe my long-suffering girlfriend and love of my life. Despite being separated across Europe, in different countries for so long, it is she who, like an angel, has provided endless support, comfort, faith and sacrifice. Lorella, I am coming to you...

The Author's Contribution

The analysis presented in this thesis is part of the *ep* physics program of the H1 experimental collaboration at the Deutsches Elektronen Synchrotron(DESY) laboratory in Hamburg, Germany. The data analysed were collected as part of an international collaborative effort involving many physicists, engineers and support staff working on the HERA collider facility and within H1.

As a member of the H1 Collaboration I participated in collection of data on shift duty, ensuring all detector systems were operating as smoothly as possible in order to utilise beam time optimally. I also contributed to the collection of calibration data. In addition I was responsible for the smooth running of the H1 Forward Tracking Detector systems in particular, acting as expert-on-call to supervise their smooth running, take steps to protect the systems when necessary and to coordinate with the other detector components by reporting to daily run meetings in the experimental hall.

All the analysis presented here was carried out by myself alone. During its evolution it has been presented regularly to meetings of the Flow and Spectra Working Group at DESY, meetings of the Liverpool H1 group and at the Institute of Physics Conference on Particle Physics and the Early Universe (Cavendish Laboratory, Cambridge, 1997). I was involved in the publication of the H1 paper "Measurement of Charged Particle Transverse Momentum Spectra in Deep Inelastic Scattering"[1].

Dedico questa tesi alla Principessa Lorella e a mia madre...

Contents

Chapter 1

Overview of Relevant High Energy Particle Physics Theory

1.1 What is Deep Inelastic Scattering?

Historically, it has always been of benefit to investigate the fundamental particles of matter, their properties and interactions. Modern science has passed through generations of "microscopy" of elementary particles with the increased understanding of chemistry, atomic physics and nuclear physics. High Energy Particle Physics is the study of sub-nuclear particles. We now know that the nucleons have a rich substructure of quarks and gluons but how does one learn more about their nature?

Deep Inelastic Scattering(DIS) investigates the substructure of nucleons by bombarding them with high energy leptons(see Figure 1.1). In the following chapters the nucleons in question are protons and the leptons are positrons/anti-electrons. If the incident lepton energy is known and the energy and direction of the emergent lepton is measured then it may be deduced what 4-momentum was imparted to the nucleon in a collision. This process is understood in the context of Quantum Electrodynamics(QED) as the emission of a virtual photon from the incident lepton which is then absorbed by a constituent quark inside the nucleon. Introduction to elementary particle physics, including QED, may be found elsewhere[2]. The virtual photon is exchanged and the 4-momentum it takes with it may cause the nucleon to break up. If the nucleon breaks up then we say DIS has occurred. Deep structure was revealed because constituents of the nucleon were separated within an inelastic scattering process[1]. In an elastic scattering process where the lepton simply recoiled from the nucleon as a whole

---

[1] Using M_P as the mass of the proton and with other terms defined in the following section the expression "deep" may be understood as $Q^2 \gg M_P^2$ and "inelastic" by $W^2 = (P+q)^2 \gg M_P^2$

we could learn little of any possible substructure.

Finer structure at the elementary particle level may be revealed by collision with smaller wavelength, or higher energy probing radiation(see Figure 1.2). In a lepton-nucleon scattering process the energy scale of the exchanged virtual photon determines whether or not substructure is revealed.

Through studying DIS one is able to test the theory of Quantum Chromodynamics(QCD) which describes interactions between partons, i.e. quarks and gluons, inside the nucleon.

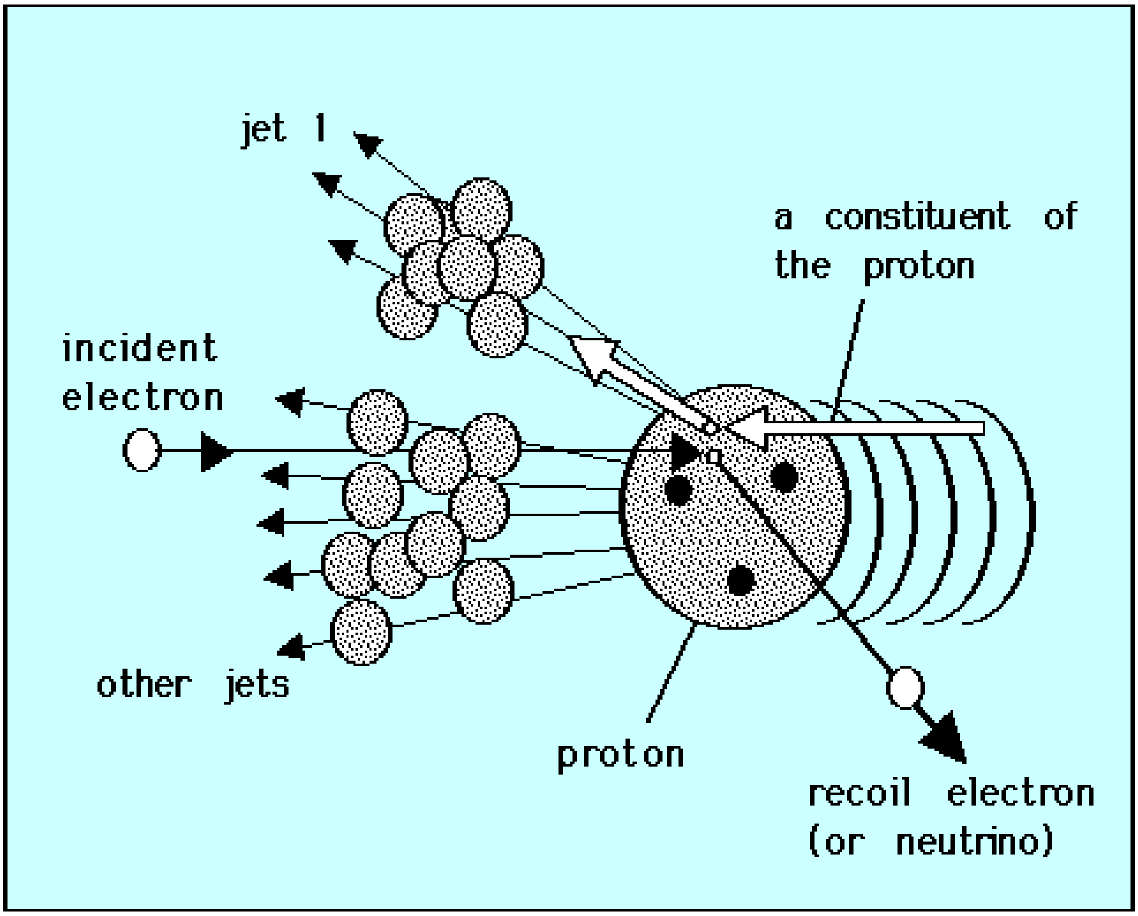

Figure 1.1: Cartoon depicting a deep inelastic scattering process.

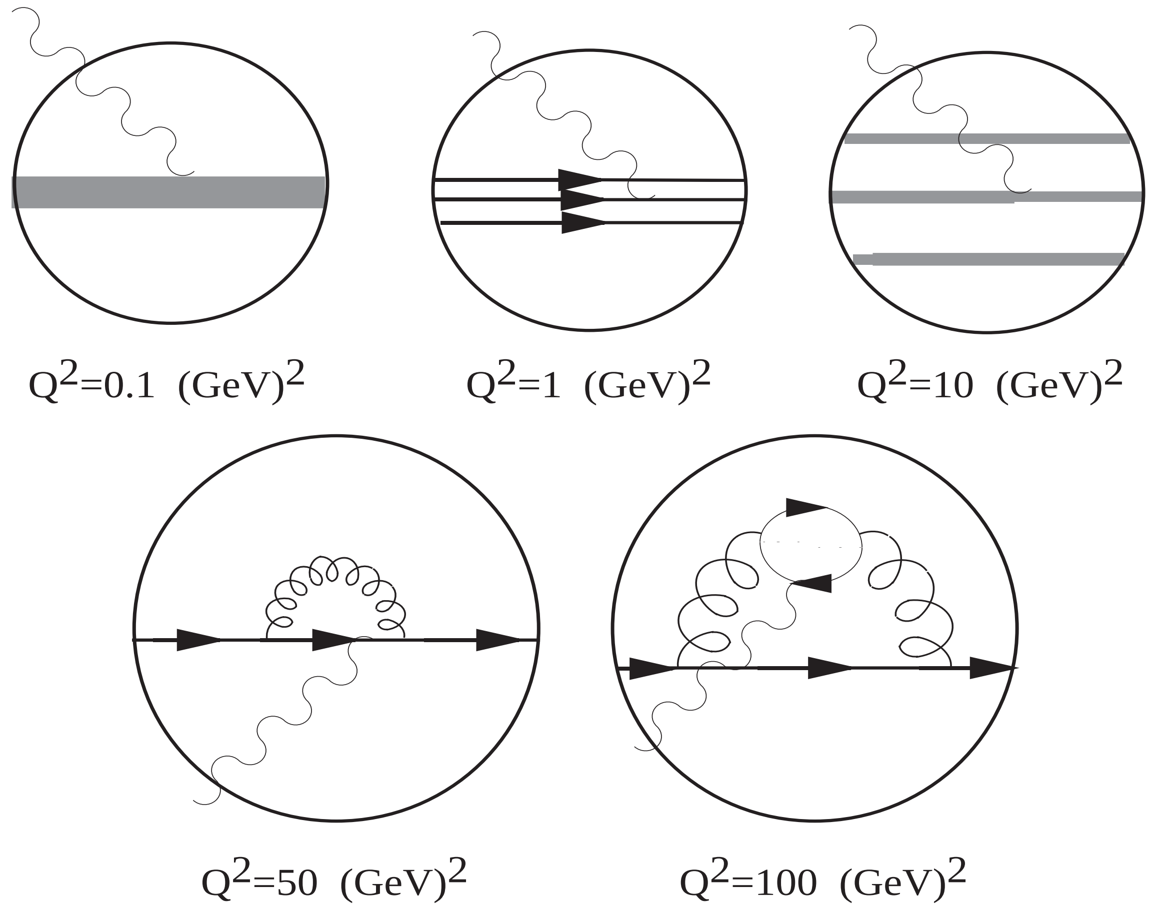

Q^2=0.1 (GeV)^2

Q^2=1 (GeV)^2

Q^2=10 (GeV)^2

Q^2=50 (GeV)^2

Q^2=100 (GeV)^2

Figure 1.2: Resolution of different levels of substructure according to probe energy.

1.2 Kinematics of Deep Inelastic Scattering of Electrons and Protons

A diagram of the basic(lowest order) process of Neutral Current (NC)[2] DIS in electron-proton collisions is shown in Figure 1.3. The incident lepton emits a photon(γ) or Z^0-boson which interacts with a constituent quark within the proton. A "colour" force field exists between the dislodged quark and the proton remnant. The Lorentz invariant quantities x, Q^2, y and W are used to describe Deep Inelastic Scattering events. Both x and y are dimensionless quantities lying in the range $0 \leq x, y \leq 1$. By manipulating their definitions it is easily shown that, at a given centre of mass energy, only two of these variables are independent. Bjorken-x is defined as:

$$x = \frac{Q^2}{2P.q} \tag{1.1}$$

where Q^2, the negative 4-momentum transfer squared, is defined as:

$$Q^2 = -q^2 = -(k^\mu - k'^\mu)^2 \tag{1.2}$$

where q^μ is the 4-momentum of the exchanged virtual photon(γ^*) and k^μ, k'^μ represent the 4-momenta of the incident(e) and scattered lepton(e') respectively. In the Bjorken limit of high Q^2, where Q^2 is much greater than the mass of the struck parton, x may be thought of as the momentum fraction of the proton carried by the struck quark. The variable y, which represents the fractional energy loss of the lepton in the rest frame of the proton(P), is defined as:

$$y = \frac{P.q}{P.k} \tag{1.3}$$

The invariant mass of the $\gamma^* P$ hadronic system is denoted W^2:

$$W^2 = (q^\mu + P^\mu)^2 \tag{1.4}$$

The variables may easily be related to the centre-of-mass energy, s, of the lepton-proton sytem by:

$$Q^2 = sxy \tag{1.5}$$

1.3 The Standard Model

Fuller accounts of the Standard Model of modern Particle Physics may be found elsewhere[3]. It is worth recalling some points which are of relevance to what fol-

---

[2] Charged Current(CC) interactions may also take place whereby the incident lepton exchanges a $W^\pm$-boson and an undetected recoiling neutrino is produced. These events are signified by "missing"(actually undetected) transverse momentum. This thesis is concerned with only virtual photon exchange - NC events with $Q^2 \ll M_Z^2$ - where a recoil lepton is detected.

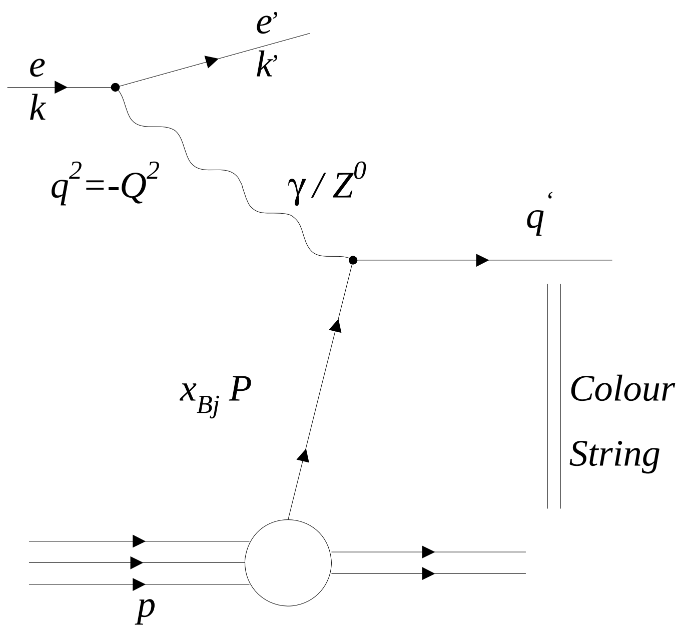

Figure 1.3: Diagram of a deep inelastic scattering event. Bjorken-x, or x_{Bj}, denotes the fraction of the proton's momentum carried by the struck quark.

lows. The fundamental particles are the fermionic leptons, corresponding neutrinos and quarks, along with the gauge bosons. The fermions belong to three generations, similar in many properties but differing in mass. The leptons are the electron(e^-), antielectron/positron(e^+), muon(μ^-), antimuon(μ^+), tau(τ^-) and antitau(τ^+). They all have corresponding neutrinos called electron-neutrino, electron-antineutrino, muon-neutrino, etc. and labelled $\nu_e, \bar{\nu_e}, \nu_\mu$, etc. The six quark "flavours", two in each generation, are denoted down(d), up(u), strange(s), charm(c), beauty/bottom(b) and truth/top(t). The gauge bosons are pictured as mediating the forces of nature by their exchange between interacting particles. The gauge bosons are the photon(γ), the $W^\pm$ and Z particles which mediate the electroweak interaction and the gluon(g) which mediates the strong nuclear force. The probabilities or strengths of interactions between particles are considered in terms of coupling constants, which are not really constant since they change according to energy scale. Interactions, or couplings, may be envisaged as Feynman diagrams[4] with vertices representing interactions.

1.4 Evidence for Colour - Quarks and Gluons

The merit of introducing a new quantum number called "colour" is well documented [2]. The existence of the Δ^{++}, a bound state of three indistinguishable u-quarks sharing the same quantum numbers, seemed to violate the Pauli Exclusion Principle. This problem could be solved by postulating that quarks carry a colour charge, arbitrarily labelled red, green or blue and that all bound states of quarks, or hadrons, must be colourless in the sense that they consist of three quarks carrying a red, green and blue charge between them (in analogy with white light), or a quark and an antiquark carrying any of the three possible colour charges and its corresponding anticolour. The concept of colour has proved very useful in building a model of the strong nuclear interaction involving hadrons.

Further evidence was provided by the well-known measurement of the R-ratio of cross-sections of s-channel quark-antiquark to muon-antimuon production in electron-positron collisions. R is defined at leading order as:

$$R = \frac{\sigma(e^+e^- \longrightarrow hadrons)}{\sigma(e^+e^- \longrightarrow \mu^+\mu^-)} = \frac{N_C \sum_q \left(e_q^2 4\pi\alpha^2/3Q^2\right)}{4\pi\alpha^2/3Q^2} = N_C \sum_q e_q^2 \tag{1.6}$$

where N_C is the number of possible colours and the summation runs over all active quarks, which is to say those whose energy threshold is accessible at the centre of mass energy $\sqrt{s}$ where $s = Q^2$. The electric charge of the quark flavour relative to that of the electron is denoted by e_q and the fine structure constant is related to the electron charge by $\alpha = e^2/4\pi$.

1.5 Quantum Chromodynamics and DIS

Comprehensive texts detailing the derivation of QCD may be found elsewhere[5]. Traditionally, experimentalists have investigated QCD in DIS by measuring the "structure functions", F_i, which parameterise the DIS differential cross section, $d^2\sigma/dxdQ^2$:

$$\frac{d^2\sigma}{dxdQ^2} = \frac{4\pi\alpha^2}{xQ^4}\left[xy^2F_1 + (1-y)F_2 + x\left(y - \frac{y^2}{2}\right)F_3\right] \tag{1.7}$$

But the differential cross-section may also be evaluated as the lepton-parton scattering convoluted with the probability of finding a parton in the nucleon:

$$\frac{d^2\sigma_{ep}}{dxdQ^2} = \Sigma_i \int_0^1 d\epsilon f_i(\epsilon)\frac{d^2\sigma_{eq_i}}{dxdQ^2} \tag{1.8}$$

where, if i denotes the parton type, e_ie its electric charge, and ϵ is the fraction of the parton's momentum carried by the struck parton,

$$\frac{d^2\sigma_{eq_i}}{dxdQ^2} = \frac{2\pi\alpha^2 e_i^2}{Q^4}(1 + (1-y)^2)\delta(x-\epsilon) \tag{1.9}$$

Comparing coefficients of y^2 and $(1-y)$ whilst neglecting F_3 leads to an expression of the structure function, F_2, in terms of the parton distributions $f_i(x)$

$$F_2 = \Sigma_i e_i^2 x f_i(x) \tag{1.10}$$

and the Callan-Gross relation, which arises from the spin-$\frac{1}{2}$ nature of the partons:

$$F_2 = 2xF_1 \tag{1.11}$$

The F_i are functions of x and, as a result of the influence of the gluon, also of Q^2. The Q^2-dependence is referred to as scaling violation since the simple parton model, without gluons, predicted independence of Q^2, or "Bjorken scaling". Bjorken scaling was originally observed and shown to be an approximate experimental fact[6]. Subsequent experiments observed the scaling violation. The term in F_3 corresponds to the weak interaction and is negligible at Q^2-values much less than M_Z^2, the square of the Z^0 mass.

The structure functions are representative of the parton density functions within the nucleon. Within QCD, there is always a probability that a given parton might emit another parton, or "split" the total momentum. The quark and gluon densities for a given momentum depend upon these splitting probabilities integrated in convolution with the parton densities at all other possible momenta(see Equations 1.19 and 1.20).

Feynman diagrams of the splitting vertices are shown in Figure 1.4 where the notation Φ_α^β corresponds to $P_{\beta\alpha}$ and represents the probability of parton β

splitting from a parent parton of type α and taking a momentum fraction z from the parent.

$$P_{qq}(z) = \frac{4}{3}\left(\frac{1+z^2}{1-z}\right) \tag{1.12}$$

$$P_{qg}(z) = \frac{1}{2}\left(z^2 + [1-z]^2\right) \tag{1.13}$$

$$P_{gq}(z) = \frac{4}{3}\left(\frac{1+[1-z]^2}{z}\right) \tag{1.14}$$

$$P_{gg}(z) = 6\left(\left[\frac{1-z}{z}\right] + \left[\frac{z}{1-z}\right] + z[1-z]\right) \tag{1.15}$$

In the next section these splitting functions are employed in evolving the parton distributions since the probability of finding a given parton carrying a certain momentum fraction of the nucleon depends on the probabilities of that parton splitting out of another which carries a higher fraction of the nucleon's momentum.

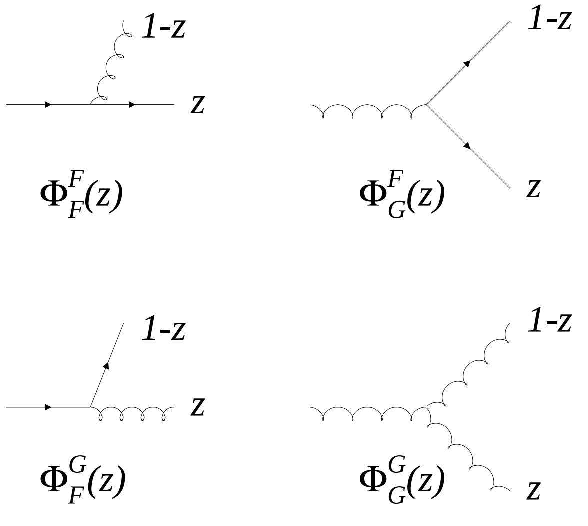

Figure 1.4: The splitting functions are probabilities associated with the emission of a parton, carrying momentum fraction z, by a parent parton.

1.6 The Running of α_S and Factorization

The non-Abelian nature of QCD, giving rise to the triple gauge coupling and the phenomenon of confinement, manifests itself in the "running" of the strong coupling constant, α_S.

$$\alpha_S(Q^2) = \frac{\alpha_S(\mu^2)}{1 + \frac{\alpha_S(\mu^2)}{12\pi}(33 - 2n_f)\log\left(\frac{Q^2}{\mu^2}\right)} \tag{1.16}$$

where the mass-scale parameter μ arises from QCD renormalization[2]. Alternatively,

$$\Lambda^2 = \mu^2 \exp\left[\frac{-12\pi}{(33 - 2n_f)\alpha_S(\mu^2)}\right] \tag{1.17}$$

and then

$$\alpha_S(Q^2) = \frac{12\pi}{(33 - 2n_f)\log\left(\frac{Q^2}{\Lambda^2}\right)} \tag{1.18}$$

where n_f is the number of quark flavours and Λ is an energy scale marking the boundary between quasi-free partons and hadrons, or a "factorization" into perturbative and non-perturbative parts. At high energy scales, which may probe to small distance scales, the coupling constant is small. This enables techniques of perturbation theory to be applied with perturbation series expanded in powers of α_S. At low energy scales, with α_S rising in magnitude, such series are divergent and perturbation theory cannot be applied. In this regime methods of lattice QCD may be attempted. Discussion of lattice QCD and its limitations in the non-perturbative sector may be found elsewhere[7]. In practice, the evolution at energy scales below a perturbative cut-off scale is described using phenomenological models.

1.7 The DGLAP Formalism

Dokshitzer, Gribov, Lipatov, Altarelli and Parisi(DGLAP) have provided descriptions [8, 9, 10, 11] of the way in which parton density functions evolve with $\log Q^2$.

$$\frac{dq_i(x, Q^2)}{d(logQ^2)} = \frac{\alpha_S}{2\pi}\int_x^1 \frac{dy}{y}\left[q_i(y, Q^2)P_{qq}\left(\frac{x}{y}\right) + g(y, Q^2)P_{qg}\left(\frac{x}{y}\right)\right] \tag{1.19}$$

$$\frac{dg(x, Q^2)}{d(logQ^2)} = \frac{\alpha_S}{2\pi}\int_x^1 \frac{dy}{y}\left[\sum_i q_i(y, Q^2)P_{gq}\left(\frac{x}{y}\right) + g(y, Q^2)P_{gg}\left(\frac{x}{y}\right)\right] \tag{1.20}$$

This work was achieved employing a resummation of powers of $\alpha_S \ln Q^2$. However, powers of $\alpha_S \ln(1/x)$ are not resummed and this implies that the DGLAP evolution equations are not applicable at very low values of x, when the $\alpha_S \ln(1/x)$ terms become significant with respect to $\alpha_S \ln Q^2$ terms. In DIS the virtual photon is absorbed by a quark within the proton. The quark line may be connected to the rest of the proton by various partonic configurations. For example see Figures 1.5 and 1.6. The generic leading diagrams, including further partonic emission, are of the partonic cascade type shown in Figure 1.7. The DGLAP formalism implies a strong ordering in the squared transverse momenta, k_{Ti}^2, of the partons of such a cascade whereby the transverse momenta of those partons close to the proton are strongly suppressed. There is also an ordering in x_i, the fraction of the proton momentum carried by a given parton on the cascade, with x_i increasing towards the proton.

$$Q_0^2 \ll k_{T1}^2 \ll ... \ll k_{Ti}^2 \ll ... \ll k_{Tn}^2 \ll Q^2 \tag{1.21}$$

$$x_1 > x_2 > ... > x_i > ... > x_n \tag{1.22}$$

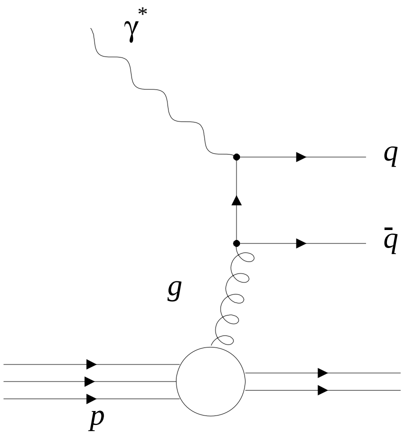

Figure 1.5: A diagram of boson-gluon fusion

1.8 The Double Leading Logarithm Approximation (DLLA)

The DGLAP formalism leads to QCD evolution equations by requiring a strong ordering of the squared transverse momenta of partons emitted along the ladder. This allows the resummation of the $\alpha_S \ln Q^2$ terms associated with the partonic

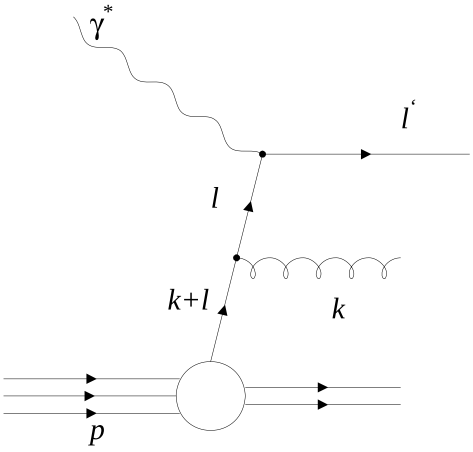

Figure 1.6: Diagram of the leading order QCD compton process

cascade. A strong ordering in the momentum fractions x_i carried by successive partons on the cascade allows a resummation of $\alpha_S \ln(1/x)$ terms. This is the basis for the Double Leading Logarithm Approximation(DLLA). The DLLA corresponds to both the transverse and longitudinal momenta of the partonic emissions being strongly ordered. The DLLA is valid when $\alpha_S \ln Q^2 \ln(1/x) \sim 1$ but $\alpha_S \ln Q^2$ and $\alpha_S \ln(1/x)$ are both small.

The gluon distribution, which dominates the structure function at low x, may be written according to the DLLA, taking account of ladder diagrams with up to r rungs, as the sum[12]

$$xg(x,Q^2) \sim \sum_r \left(\frac{1}{r!}\right)^2 \left(\frac{3\alpha_S}{\pi} \ln Q^2 \ln(1/x)\right)^r \tag{1.23}$$

or:

$$xg(x,Q^2) \sim \exp\left[2\left(\frac{3\alpha_S}{\pi} \ln(1/x) \ln Q^2\right)^{\frac{1}{2}}\right] \tag{1.24}$$

Another description which provides a bridge, between the description of the DGLAP region and that of the BFKL region at low x (see following Section), is that of Ciafaloni, Catani, Fiorani and Marchesini(CCFM). This work involves an angular ordering of the partonic emission[13, 14].

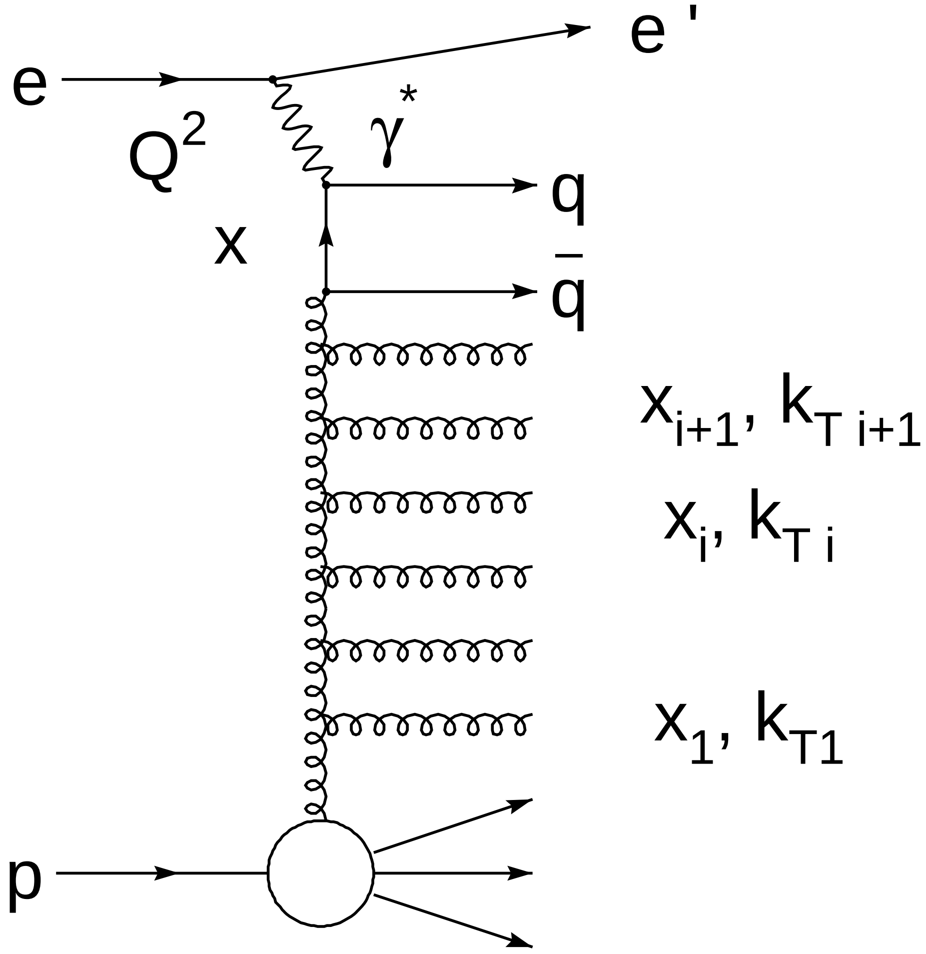

Figure 1.7: The leading diagrams are of the partonic cascade type.

1.9 The Low x Limit - BFKL Formalism

Balitsky, Fadin, Kuraev and Lipatov(BFKL) have produced[15, 16] QCD evolution equations which resum the leading terms in $\alpha_S \ln(1/x)$. This is appropriate at low x where such terms dominate. The BFKL equations require a strong ordering in x_i in order to resum the $\alpha_S \ln(1/x)$ terms but no ordering in the transverse momenta of the partonic cascade. The BFKL equations are therefore appropriate for a less constrained partonic cascade than the DLLA, provided that $\alpha_S \ln Q^2$ is not too large. Successive partons on the cascade have similar squared transverse momenta, the magnitude of which diffuses in a random walk.

$$k_{Ti}^2 \simeq k_{Ti+1}^2 \tag{1.25}$$

$$x_1 \gg x_2 \gg ... \gg x_i \gg ... \gg x_n \tag{1.26}$$

The gluon distribution according to the BFKL formalism may be written as the sum

$$xg(x,Q^2) \sim \sum_r \left(\frac{1}{r!}\right)^2 \left[\frac{3\alpha_S}{\pi} c \ln(1/x)\right]^r \tag{1.27}$$

where c is a constant. By defining $\lambda \equiv \frac{3\alpha_S}{\pi} c$, this may be rewritten

$$xg(x,Q^2) \sim \exp\left[\lambda \ln(1/x)\right] \tag{1.28}$$

which may be simplified to

$$xg(x,Q^2) \sim x^{-\lambda} \tag{1.29}$$

BFKL dynamics predict an $x^{-\lambda}$ behaviour of the gluon density at low x. There is an associated non-ordering of the partonic k_T. These are two signatures which may be used when trying to identify BFKL dynamics in the small x region at HERA. Inclusive measurements of the proton structure function F_2 and transverse energy flow E_T have been consistent with both BFKL and DGLAP predictions[17]. In this thesis it will be demonstrated that it is also possible to investigate the underlying parton dynamics and identify partonic k_T-ordering effects.

1.10 Fragmentation and Hadronisation

Due to "colour confinement", partons emitted from a perturbative cascade must undergo "dressing" of their naked colour. The dressing/hadronisation process is a non-perturbative one. The models used to describe this process are described in the next chapter. Hadronisation involves confinement on the nuclear distance scale of about 1 Fermi($10^{-15}m$). If one applies Heisenberg's Uncertainty Principle then it is possible to convince oneself that the corresponding energy is of the order of 300 MeV.

1.11 Transverse Momentum Spectra and the Underlying Parton Dynamics

The hadronisation process tends to produce additional soft gluons. Their corresponding colour singlet particles are therefore of low transverse momentum also. Detection of high p_T particles is an indication of underlying partonic emission involving high transverse momentum. If the appropriate kinematic domain has been reached then this is more likely to arise from BFKL dynamics, without the k_T-suppression which is inherent to the DGLAP scheme. This forms the basis of motivation for this thesis. An analysis is presented that compares data with predictions incorporating k_T-suppression and non-k_T-ordering.

Chapter 2

Monte Carlo Generators and Simulation

2.1 Introduction to the Monte Carlo Method

In order to make a computer model of a physical system it is assumed that characteristics of the of the system can be described by probability density functions. Once the pdf's are known, a Monte Carlo[1] simulation[18] can proceed by random sampling from the probability density functions. Many simulations are then performed (multiple "trials") and the desired result is taken as an average over the number of observations (which may be a single observation or perhaps millions of observations). In many practical applications, one can predict the statistical error or variance in this average result, and hence an estimate of the number of Monte Carlo trials that are needed in order to achieve a given error or level of accuracy.

In setting up a Monte Carlo simulation of a physical process a number of elements are required and procedures followed. Probability distribution functions (pdf's) must be ascribed to properties of the system. A random number generator uniformly distributed on the unit interval must be available. A sampling rule or prescription for sampling from the specified pdf's, assuming the availability of random numbers on the unit interval, must be given. The outcomes must be accumulated into overall counts for the quantities of interest. An estimate of the statistical error (variance) depending on the number of trials and other quantities may be determined.

In High Energy Particle Physics experiments Monte Carlo simulation of QCD

---

[1] Monte Carlo, the capital city of Monaco is famous for its casinos whose games employ concepts of probability in common with computer simulations of physics processes.

processes is generally factorised into a number of stages. Firstly, a hard subprocess is generated according to probabilities which parameterise our knowledge of the process cross-section. After this stage the system will consist of a few elementary partons and leptons. Secondly, some kind of partonic cascade is generated according to our understanding of the perturbative sector of QCD. Then, once the partonic cascade has evolved into the non-perturbative sector a model must be employed to describe as best as possible the hadronisation process and particle decays so that for a given simulated event we are left with a set of simulated particles emerging from the collision point with different directions and momenta. Finally, this set of particles is fed into a detector simulation which models the response of all our detector subsystems, and possible interactions of the emerging particles with their material. This gives a simulation of the possible response of the experimental detectors to a given event, including the modelling of their components' efficiencies. Generating and simulating many thousands, even millions of events, and averaging gives us an expectation according to the models and theories incorporated within the Monte Carlo simulation.

2.2 Parton Density Functions

Some important phenomenological models are utilised in the Monte Carlo generation of DIS events. In particular, the parton distributions within the proton are taken to be those of Glück, Reya and Vogt[19]. Recent studies by the same authors show that these parton distributions are, for practical purposes, consistent with newer ones developed taking recent data into account[20].

2.3 The LEPTO Event Generator

Many aspects of DIS events have been successfully described by the LEPTO Monte Carlo. A more detailed description of the LEPTO Monte Carlo, including a list of its tunable parameters and defaults may be found elsewhere[21]. In LEPTO the parton level interaction is based upon the standard model electroweak cross sections, which are implemented to leading order. First order QCD matrix elements(ME) for gluon radiation and boson-gluon fusion are implemented.

2.4 Parton Showers

Higher order QCD radiation is treated within the perturbative sector using parton showers(PS) based upon the DGLAP QCD evolution equations. Together with the first order QCD process calculations this forms what is known as the matrix element plus parton showers(MEPS) description.

The parton showers approach has the advantage that arbitrarily high orders in α_S can be simulated though only in the leading $\log Q^2$ approximation as opposed to the exact treatment in fixed order ME calculation. In DIS the struck quark can emit partons both before and after the boson vertex giving rise to initial and final state parton showers, respectively. A parton close to mass-shell in the incoming nucleon can initiate a parton emission cascade, or shower, where in each branching one parton becomes increasingly off-shell with a space-like virtuality ($m^2 < 0$) and the other is on-shell or has a time-like virtuality($m^2 > 0$). This initial state space-like shower results in a space-like quark which interacts with the electroweak boson and turns into an outgoing quark which is either on-shell or has a time-like virtuality. In the latter case a final state, time-like shower will result where the off-shell mass is reduced by branching into daughter partons with decreasing off-shell masses and decreasing opening angles. This shower continues until all partons are essentially on-shell. Any parton with a time-like virtuality from the inital state shower will develop similarly. The behaviour of initial and final state parton showers is similar since they are both based on the branching processes $q \to qg$, $g \to gg$ and $g \to q\bar{q}$ as described by the DGLAP equations in the leading $\log Q^2$ approximation of perturbative QCD.

2.5 The Colour Dipole Model and the Ariadne Interface

The Colour Dipole Model(CDM) as implemented in the Ariadne[22] program describes gluon bremsstrahlung in terms of radiation from colour dipoles between partons, instead of treating the partons as independent emitters. The purpose of the Ariadne Monte Carlo program, which employs the CDM, is to generate the QCD cascade process only and it is interfaced to other programs which generate hard interactions, hadronisation and particle decays. The CDM provides an alternative method to the MEPS method with which to simulate the partonic cascade.

2.5.1 The CDM for $q\bar{q}$ Pairs

Gluons emitted from $q\bar{q}$ pairs, produced for example in e^+e^- collisions, may be treated as radiation from a colour dipole between the q and $\bar{q}$ in an analogous fashion to the production of electromagnetic radiation from an antenna. To a good approximation, the emission of a second, softer gluon, may be treated as radiation from two independent dipoles, one between the q and g and one between the g and $\bar{q}$. In the CDM this process is generalised so that the emission of a third, still softer gluon, is given by three independent dipoles, etc.

The cross section for gluonic emission from such a dipole is proportional to α_S, where the energy scale is taken to be that of the p_T^2 of the emission. The cross section also depends upon the final state energy fractions x_i of the emitting partons in the dipole centre of mass system, where $i = 1$ and 3 denote the initial partons and $i = 2$ the gluon emitted between them, with m_i their respective masses[22]:

$$x_i = \frac{2E_i}{\sqrt{S_{dipole}}} \tag{2.1}$$

$$p_T^2 \equiv S_{dipole}\left(1 - x_1 + \frac{m_1^2 - [m_2 + m_3]^2}{S_{dipole}}\right)\left(1 - x_3 + \frac{m_3^2 - [m_2 + m_1]^2}{S_{dipole}}\right) \tag{2.2}$$

$$\frac{d\sigma}{dx_1 dx_3} \propto \alpha_S\left(p_T^2\right)\left[\frac{(x_1^2 + x_3^2)}{(1 - x_1)(1 - x_3)}\right] \tag{2.3}$$

2.5.2 The CDM in DIS

In DIS the CDM assumes that all QCD radiation may be described as originating from a colour dipole formed between the struck quark and the nucleon remnant. In DIS the struck quark is considered point-like while the nucleon remnant is an extended object. This causes some suppression of emission in analogy with an extended antenna. As gluons are radiated further colour dipoles are created and emit in turn. Successive emission reduces the energy scale of the dipoles to a level where it becomes appropriate for a model of non-perturbative hadronisation to be applied.

2.6 The Linked Dipole Chain Monte Carlo

A recent development based upon concepts of the CCFM equations mentioned earlier is the Linked Dipole(LDC) Chain Monte Carlo[23]. Although the LDC has not been studied in this thesis it should be pointed out that this is an interesting model which allows for sections of increasing and decreasing virtuality along the partonic chain. Initial studies elsewhere [**?**] show that in its present form the LDC does not describe forward jet cross sections and particle spectra perfectly but nevertheless is able to reproduce some other distributions[24].

2.7 The Lund String Model of Fragmentation

Both types of Monte Carlo simulation used were interfaced with the Lund String Model of Hadronisation in order to predict the expected hadronic final states arising from DIS after the parton level calculations within the perturbative sector.

At long distances, QCD becomes strongly interacting and perturbation theory breaks down. In this confinement regime, the coloured partons are transformed into colourless hadrons. The fragmentation process has yet to be understood from first principles, starting from the QCD Lagrangian. In order to describe the process various phenomenological models have been developed, of three main types - string fragmentation, independent fragmentation and cluster fragmentation.

The Lund Model[25] is one of string fragmentation. As q and $\bar{q}$ partons move apart the picture is one of a colour flux tube being stretched between them. QCD studies lend support to a linear confinement picture whereby the energy stored in the colour dipole field between a colour charge and an anticharge increases linearly with separation between them. From hadron spectroscopy, the string constant or energy per unit length is deduced to be $\kappa \approx 1GeV/fm$, effectively a mass density along the string. As the q and $\bar{q}$ move apart, the potential energy stored in the string increases, and the string may break by the production of a new $q'\bar{q}'$ pair. The system then splits into two colour singlet systems $q\bar{q}'$ and $q'\bar{q}$. If the invariant mass of either of these two string pieces is large enough, further breaks may occur. In the Lund String Model the string break-up process is assumed to proceed until on-mass-shell hadrons remain, each hadron corresponding to a small piece of string with a quark on one end and an antiquark at the other. If several partons are moving apart from a common origin, the details of the string drawing become more complicated. For a $q\bar{q}g$ event, a string is stretched from the q via the g to the $\bar{q}$ end. The gluon is a kink on the string.

In one sense hadronisation effects are large since this is where the bulk of the multiplicity comes from. However, the overall energy flow of a high-energy event is mainly determined by the perturbative processes, with only a minor smearing caused by the hadronisation. In the Monte Carlo comparisons with data which follow, both simulations compared with the data employ the Lund model of hadronisation. The significant differences between the two Monte Carlo models arise from the differences in underlying partonic emission simulation.

2.8 QED Radiation and the DJANGO Interface

More details of the DJANGO program may be found elsewhere[26]. Since initial state QED radiation may alter the incident lepton 4-momentum, which is considered known in the evaluation of kinematic variables using the electron method, it is important to be able to simulate this effect. The DJANGO Monte Carlo generator calculates QCD radiative corrections of order $O(\alpha_S)$, electroweak corrections of order $O(\alpha)$ and combined QCD-QED effects of order $O(\alpha\alpha_S)$.

Chapter 3

HERA and the H1 Detector

3.1 The HERA Collider

The Hadron Electron Ring Anlage (HERA) , situated at the DESY laboratory in Hamburg, is composed of two storage rings with a circumference of 6.3 km. Electrons or positrons are accelerated to 27.6 GeV clockwise in one of the rings and protons at 820 GeV circulate anti-clockwise in the other. The beam pipes intersect at two interaction regions along the ring where the electrons and protons are brought into collision with a centre-of-mass energy of $\sqrt{s} = 300.9\,\mathrm{GeV}$. The beams are injected into the rings in a series of bunches separated in time by $96ns$. In 1994 the machine operated with 94 positron bunches and 90 proton bunches. Of these only 84 were in collision. The remaining "pilot" bunches, were used to determine backgrounds due to beam gas and beam wall interactions, where the electron or proton beam interacts with residual gas in the evacuated beam-line or with the material of the beam pipe respectively.

3.2 A Brief Overview of the H1 Experiment

More detailed descriptions of the many and diverse detector systems that form the H1 experiment may be found elsewhere[27]. A diagram showing the various components as they were during the 1994 running period is shown in Figures 3.2 and 3.3. The H1 experiment is designed to be as hermetic as possible, giving almost 4π-coverage around the e^+p interaction region. Because the momenta of the beam particles are not equal as at many collider facilities the detector systems are asymmetrically positioned with the "forward" detectors arranged around the proton direction, in which the centre of mass frame tends to travel(with respect to the laboratory). The main features pertinent to this analysis are the Backward

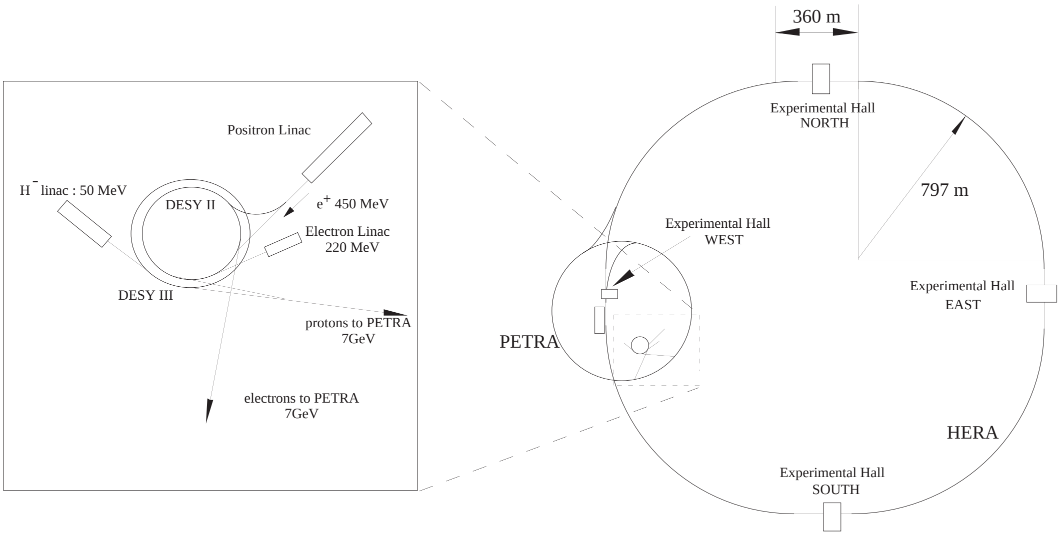

Figure 3.1: The HERA collider.

Electromagnetic Calorimeter in which medium/low Q^2 scattered positrons were detected, and the Central and Forward Tracking Detectors, with their associated trigger chambers, which measured the momenta of the particles emerging from the interaction zone.

The coordinate system. defined with respect to the proton beam direction, is shown in Figure 3.4.

3.3 The H1 Tracking System

3.3.1 Principles

In 1994 all tracking chambers in H1 were drift chambers. In general the drift chambers consist of many drift cells, each cell having a set of anode sense-wires, separated by field shaping wires and enclosed by cathode wires or planes. The electrostatics of the cell are constructed such that there is a uniform electric drift field across the volume of the cell. Charged particles passing through the drift volume of the cell ionize atoms of gas in this volume by imparting a fraction of their kinetic energy in an electromagnetic interaction. The resulting ions then drift towards the cathodes and the electrons towards the sense wires. Close to

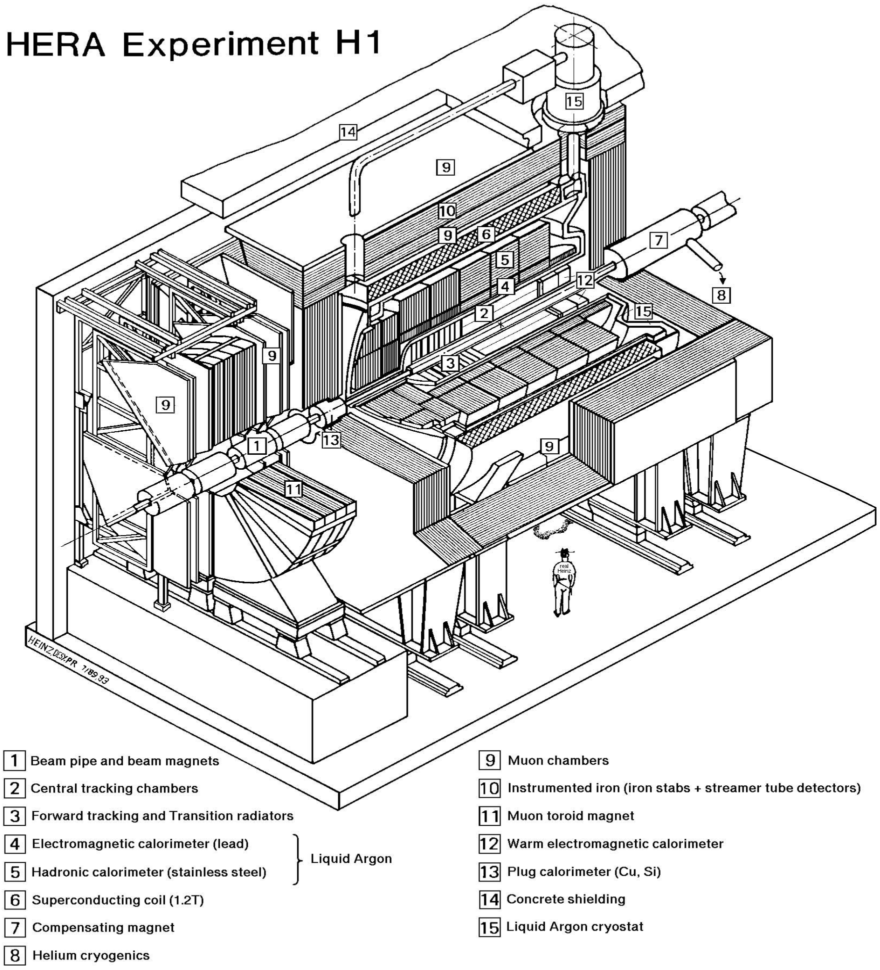

Figure 3.2: The H1 experimental detector systems.

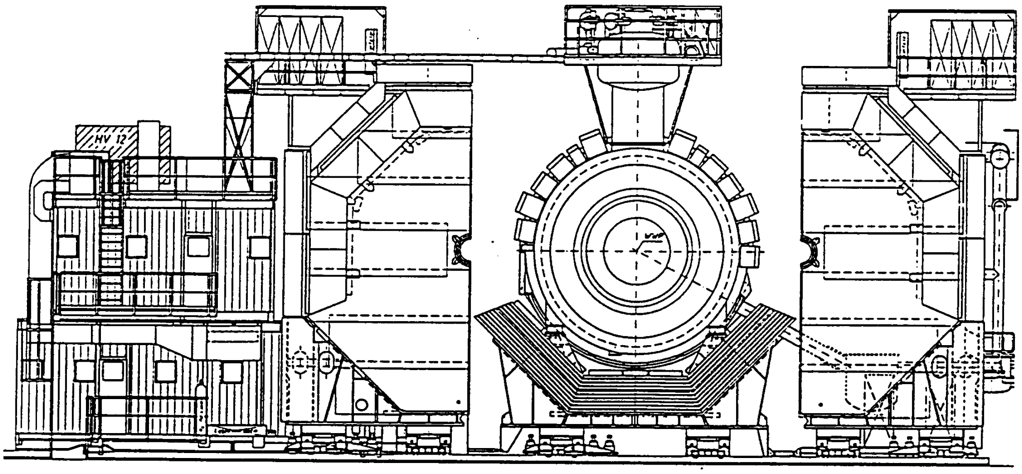

Figure 3.3: Technical drawing of the H1 experiment in cross-section.

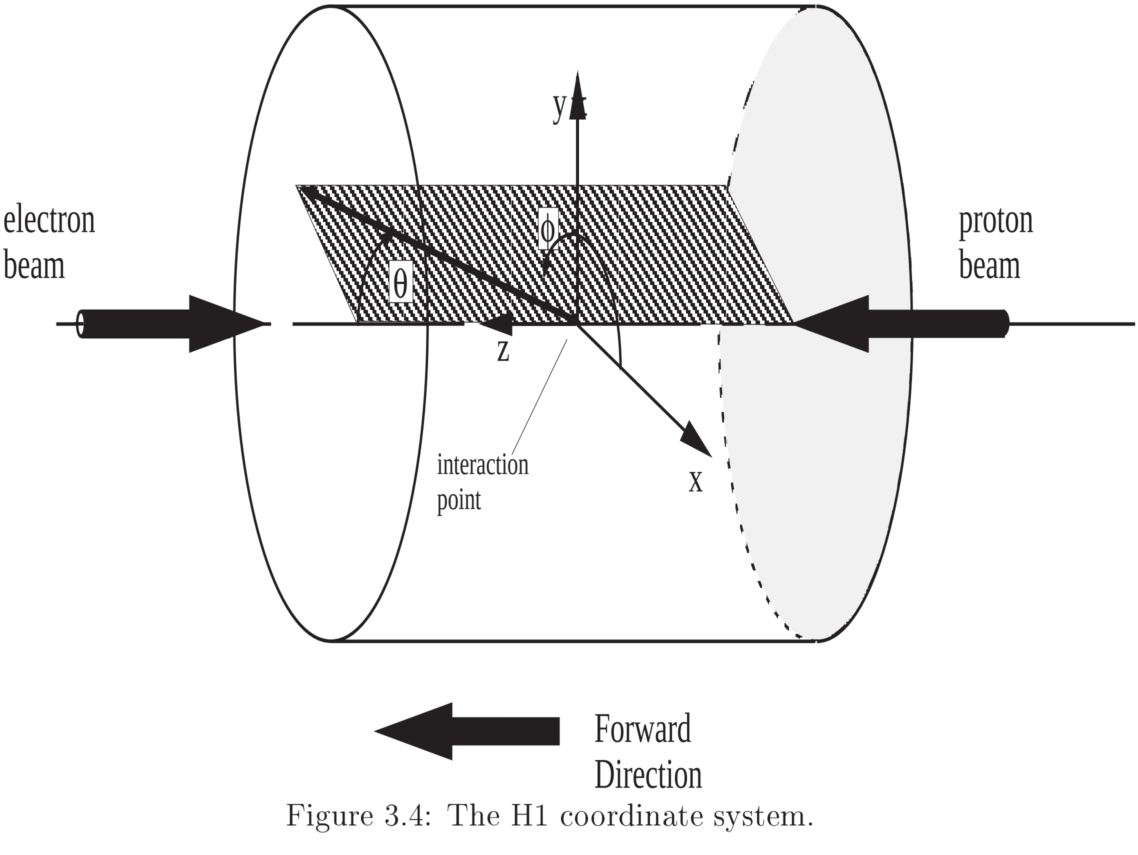

Figure 3.4: The H1 coordinate system.

the sense wires the field strength increases and the accelerating electrons gain sufficient energy to ionize the gas, producing more electrons which in turn are able to further ionize the gas causing an avalanche of electrons. This enables an amplified signal to be collected at the wires. The measured signals are electrical pulses induced by the positive ions drifting away from the sense wires[28]. From the known drift velocity of the electrons within the drift volume and the time of arrival of the track and signals on the sense wires it is possible to reconstruct the track's position in the drift cell. Once a set of track points are established, a charged particle's momentum may be ascertained by virtue of the fact that moving charged particles are accelerated by a magnetic field perpendicular to their motion. The magnetic field in the H1 detector volume is kept as far as possible parallel to the beam so that transverse momentum of charged particles may be measured. The z-component of magnetic field in the H1 volume is shown in Figure 3.5. It is easily shown that the particle's transverse momentum, p_T, measured in GeV/c is given by:

$$p_T = (0.2998) q B_z \rho \tag{3.1}$$

where q is the electric charge of the particle in units of the electronic charge e, B_z is the magnetic field component parallel to the beam and ρ is the radius of curvature depicted by the particles trajectory projected into the xy-plane. Drift chambers are also capable of performing $\frac{dE}{dx}$ measurements for low momentum particles. This is possible as the charge deposited on the wire is proportional to the amount of initial ionisation produced by the particle, which in turn is dependent on the velocity of the particle. The low momentum particles can then be distinguished by comparing the total charge deposited along the length of a track and the particles momentum.

The rate of energy loss with distance traversed of a charged particle of velocity βc and charge ze travelling through a medium of density ρ, atomic number Z, atomic mass A and of effective ionisation potential I, is given by the Bethe-Bloch equation [28]:

$$\frac{dE}{dX} = \frac{2KZ\rho}{A\beta^2}\left[\beta^2 + \ln\left(\frac{I\left(1-\beta^2\right)}{2mc^2\beta^2}\right)\right] \tag{3.2}$$

where

$$K = \frac{2\pi N z^2 e^4}{mc^2} \tag{3.3}$$

-m and e being the electronic mass and charge respectively and N the Avogadro number.

The read out of the sense wires is performed by flash analogue–to–digital converters (FADC) , with a sampling frequency of 104 MHz. This enables the time of arrival of the first electrons to be determined to an accuracy of a few nanoseconds, resulting in a precision in the drift distance of $\sim 200\,\mu$m. To avoid "drift sign ambiguities", the symmetry of the cell is broken by staggering the sense wires alternately about the mid–plane of the cell. The distance from the

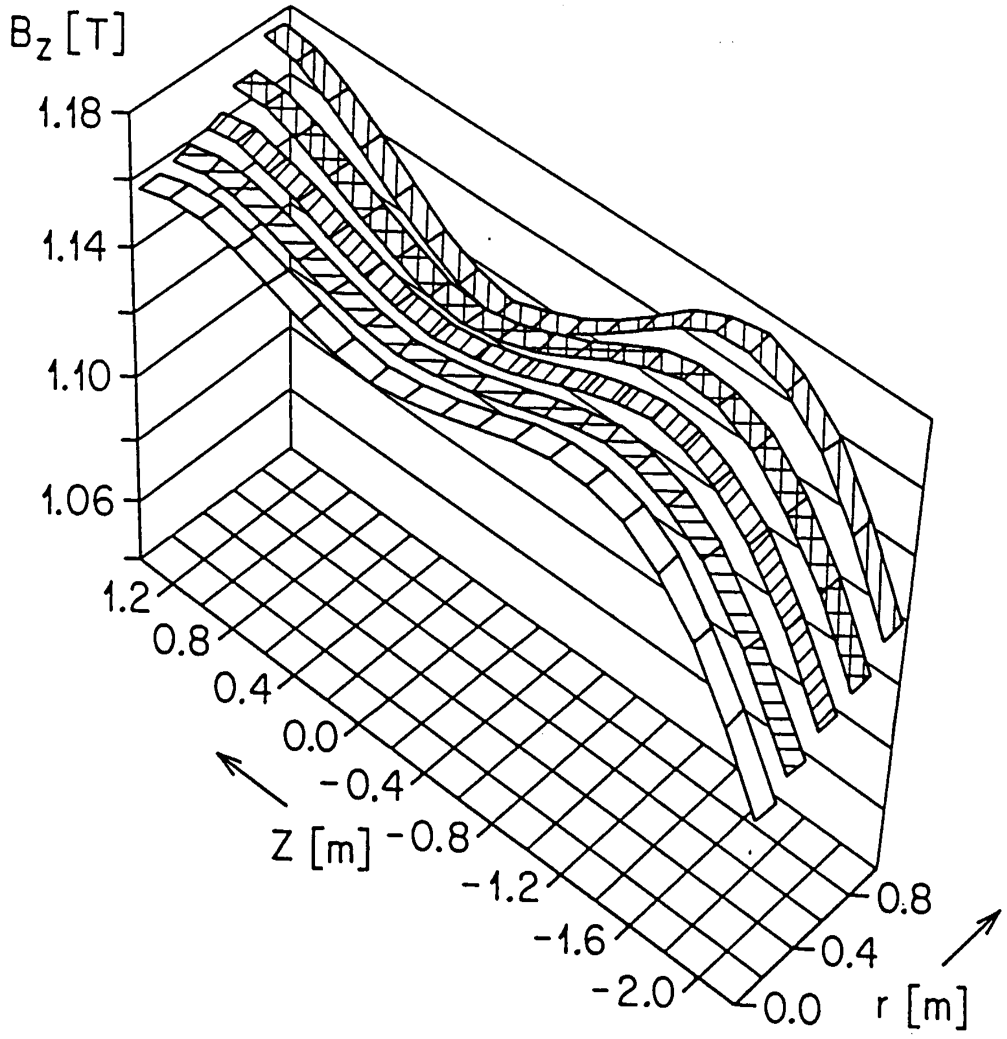

Figure 3.5: Illustration of the z-component of the magnetic field in the H1 detector volume. It is kept as constant and parallel to the beam as possible in order to facilitate transverse momentum measurement of charged particles.

end of the wire to the point at which the ionisation arrived can be calculated from "charge division", by using resistive wire that is read out at both ends of the sense wire. The distance can then be calculated from the ratio of the charges at each end. The resolution on this coordinate is typically of the order of 1% of the sense wire length.

Triggering is performed using multi–wire proportional chambers (MWPCs) which consist of a large collection of wires held at a relatively high potential.

Particles entering the chamber will pass through regions in which the electric field is very high. As the drift distance is small, the signal arrives a few tens of nanoseconds after the particle traverses the chamber, giving a rapid time measurement of the event, ideal for triggering.

The H1 tracking system(shown in figure 3.6) is comprised of the forward tracking detector (FTD) covering the angular range 5° – 25°, the central track detector (CTD), covering the angular range 25° – 155° and the backward proportional chamber (BPC), which covers the angular range 155° – 174°. The FTD and CTD consist of a mixture of drift chambers and multi–wire proportional chambers, for track reconstruction and triggering respectively.

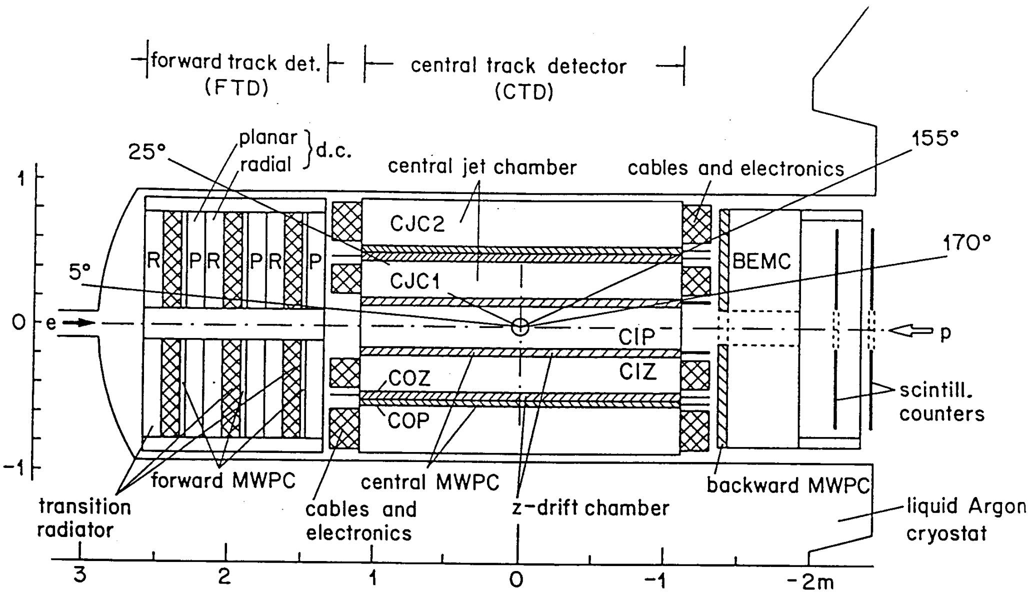

Figure 3.6: Figure showing a r-z cross-section through the H1 tracking detectors.

3.3.2 The Central Track Detector (CTD)

The Central Tracking Detector(cross section shown in figure 3.7), consists of 4 drift chambers and 2 multi–wire proportional chambers. The main drift chambers of the CTD are the central jet chambers, CJC1 and CJC2. The sense wires in the CJC run parallel to the beam axis and the drift cells are tilted at an angle of $\frac{\pi}{6}$ radians to the radial direction. Knowledge of the drift time enables an accurate point to be determined in the $r - \phi$ plane and, as both ends of the sense wire are read out, the z coordinate of the hit can be determined using charge division. CJC1 is divided into 30 cells in ϕ and has 24 sense wires per cell, CJC2 has 60 cells with 32 sense wires per cell.

Two separate drift chambers are used to improve the z coordinate resolution of the tracks found in the CTD, the inner z chamber (CIZ) situated in the inner radius and the outer z chamber (COZ), situated between CJC1 and CJC2. The z chamber drift cells consist of 4 sense wires positioned at different radii that form “rings” around the beam axis. The drift time gives the z coordinate of the hit and charge division gives its position in ϕ. The CIZ consists of 15 drift cells and the COZ 24 drift cells.

The two MWPCs used for triggering on tracks are the CIP situated inside the CIZ and the COP situated between CJC1 and the COZ. Each of these detectors consists of two concentric layers of chambers, with the cathode pads being read out. In the CIP, the pads cover an angle of $\frac{\pi}{4}$ with the two layers rotated by one half pad to increase the angular resolution. Each ϕ sector is divided into 60 pads in z. The COP is divided into 18 pads in z, each pad covering an angular range of $\frac{\pi}{8}$.

3.3.3 The Forward Tracking Detector (FTD)

Further details of the FTD are available elsewhere[29, 27]. The FTD consists of three “super-modules” each containing, in order of increasing z, a planar wire drift chamber (PWDC), a forward multi–wire proportional chamber (FMWPC), a transition radiator and a radial wire drift chamber (RWDC).

Planar Wire Drift Chamber

Each PWDC contains three separate drift chambers, or “orientations”, rotated at $\frac{\pi}{3}$ relative to each other. Each orientation is four wires deep in z, and the wire planes are separated by $6\,mm$ in z. The orientations consist of cuboid drift cells which are $56\,mm$ wide and contain four sense wires sperated in z (see Figures 3.10 and 3.11). As the sense wires are only read out at one end, hits from each of the planes must be combined to give an accurate line segment. These segments can then be linked with segments found in the radial chambers and in the CTD to produce tracks.

Radial Wire Drift Chambers

A radial wire chamber consists of 48 drift cells, each of which contains 12 radially strung sense wires. This results in the maximum drift distance varying from 10 mm at the inner radius to 50 mm at the outer. The sense wires are separated in z by 10 mm and are staggered about the mid–plane of the cell with field shaping wires between each sense wire. The sense wires are connected in pairs around

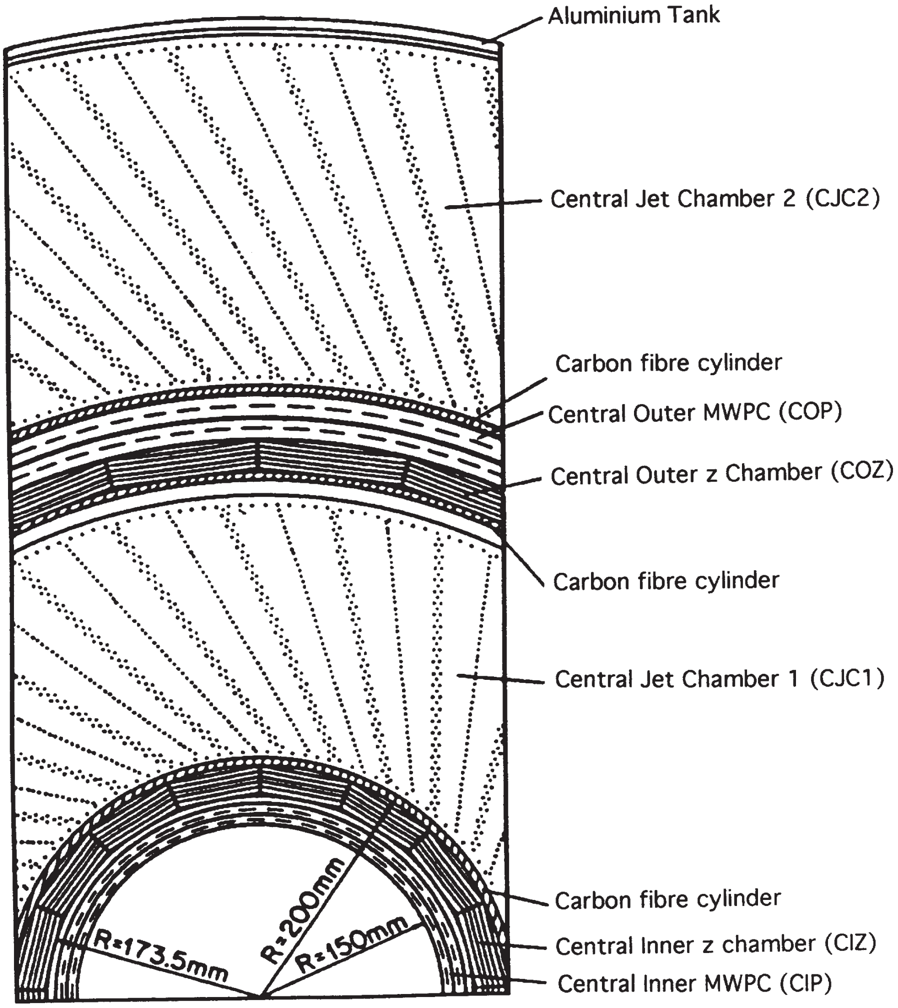

Figure 3.7: A cross-section through the Central Tracking Detector.

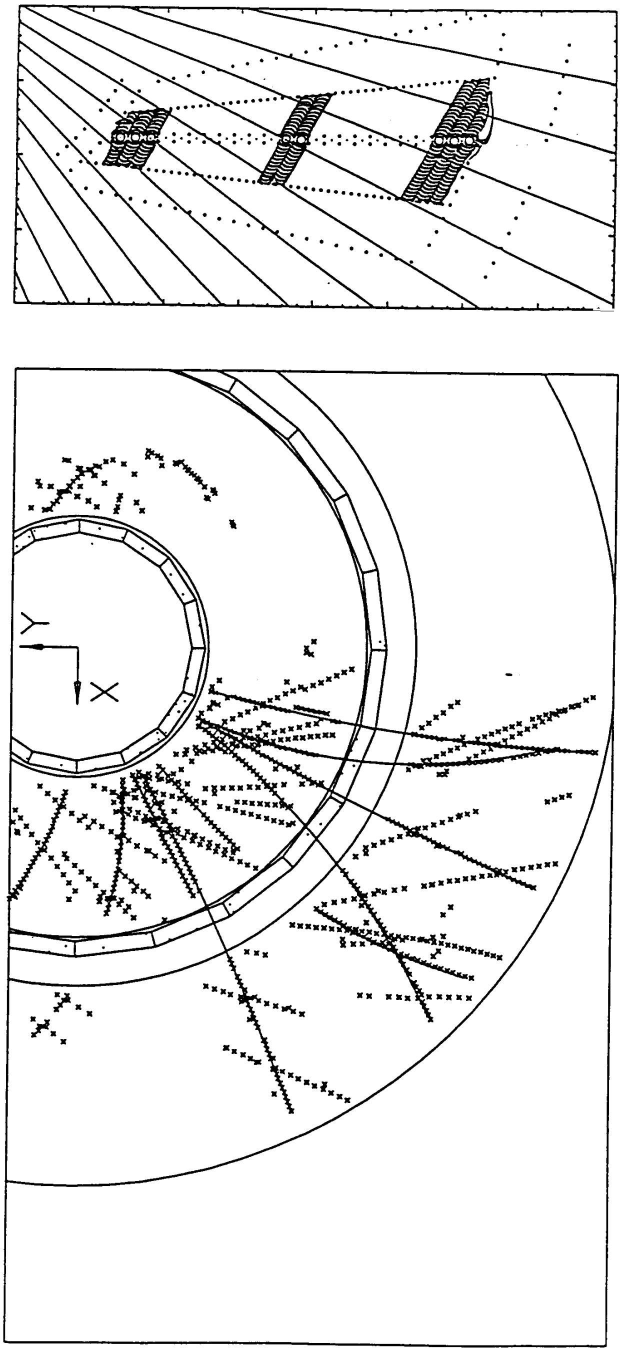

Figure 3.8: Reconstruction of tracks from signals in the Central Tracking Detector

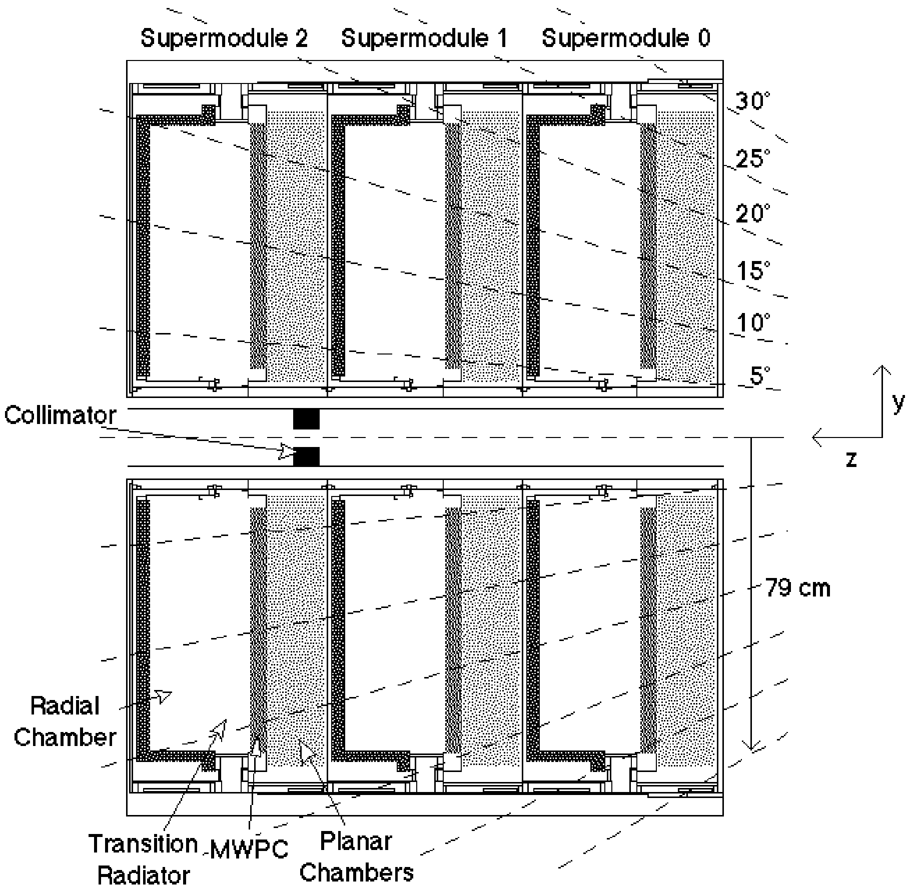

Figure 3.9: The Forward Tracking Detector supermodules.

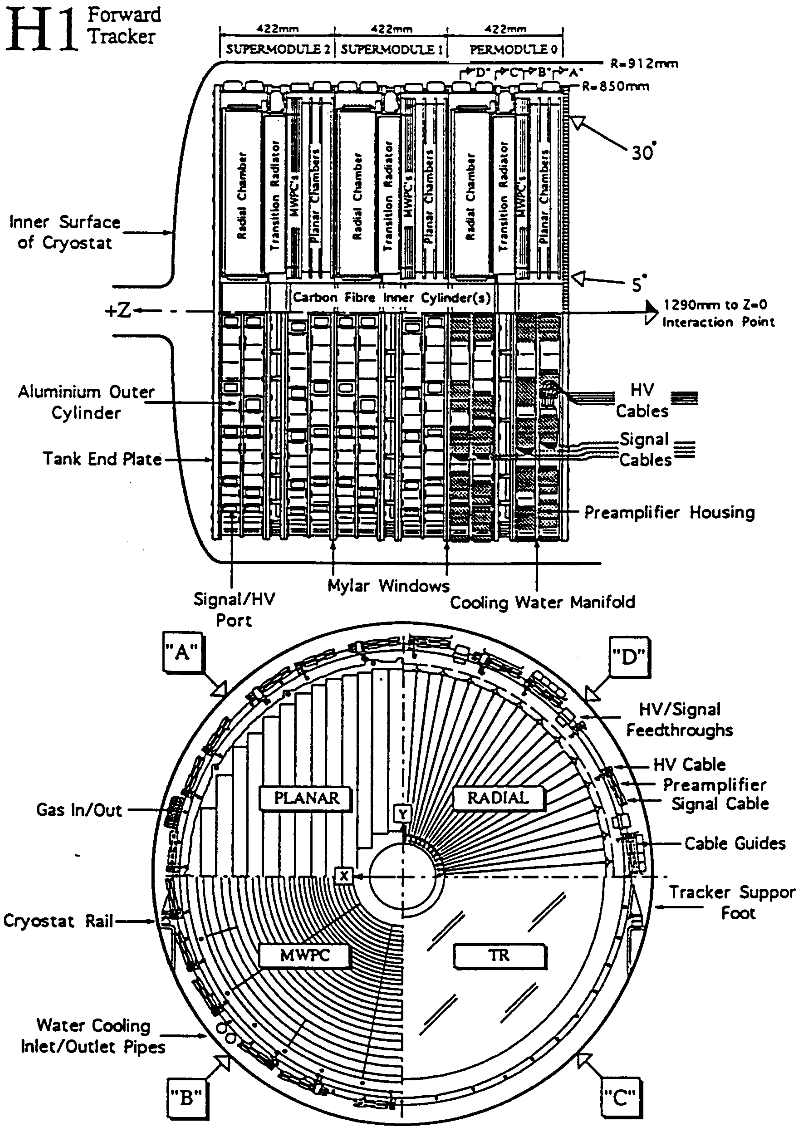

Figure 3.10: Technical drawing displaying the composition of the Forward Tracking Detector systems.

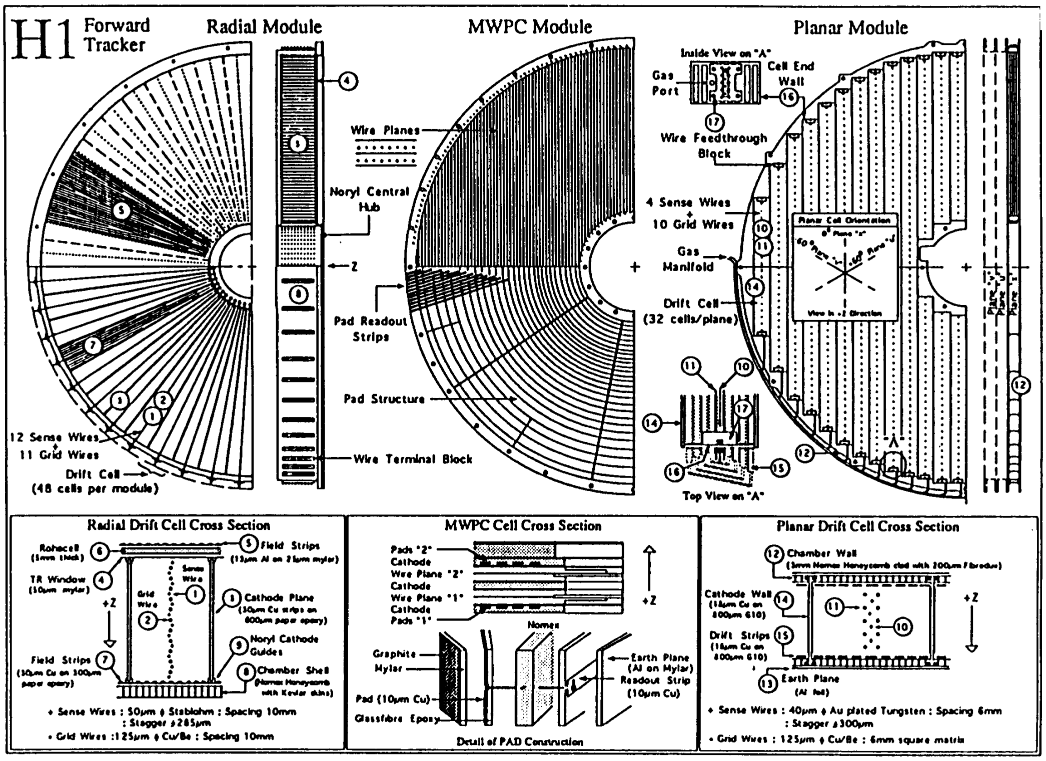

Figure 3.11: Further details of the FTD subsystems.

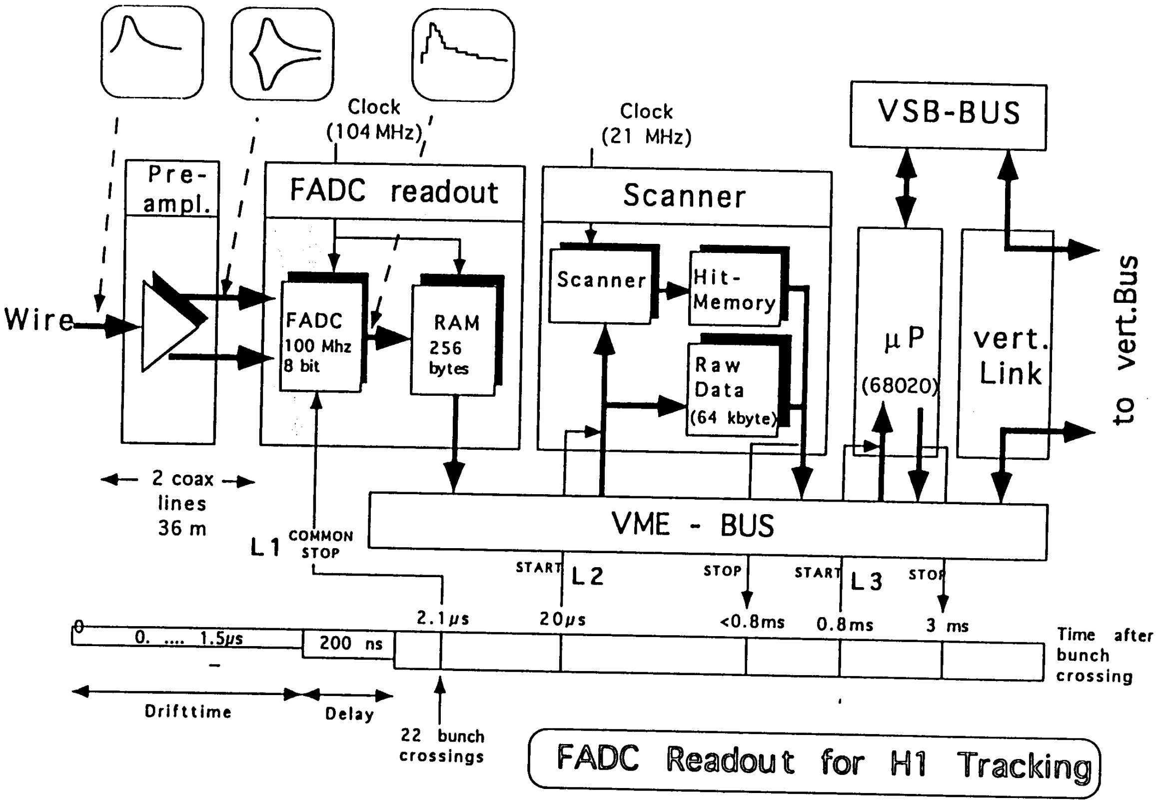

Figure 3.12: Diagram of the readout of the tracking systems.

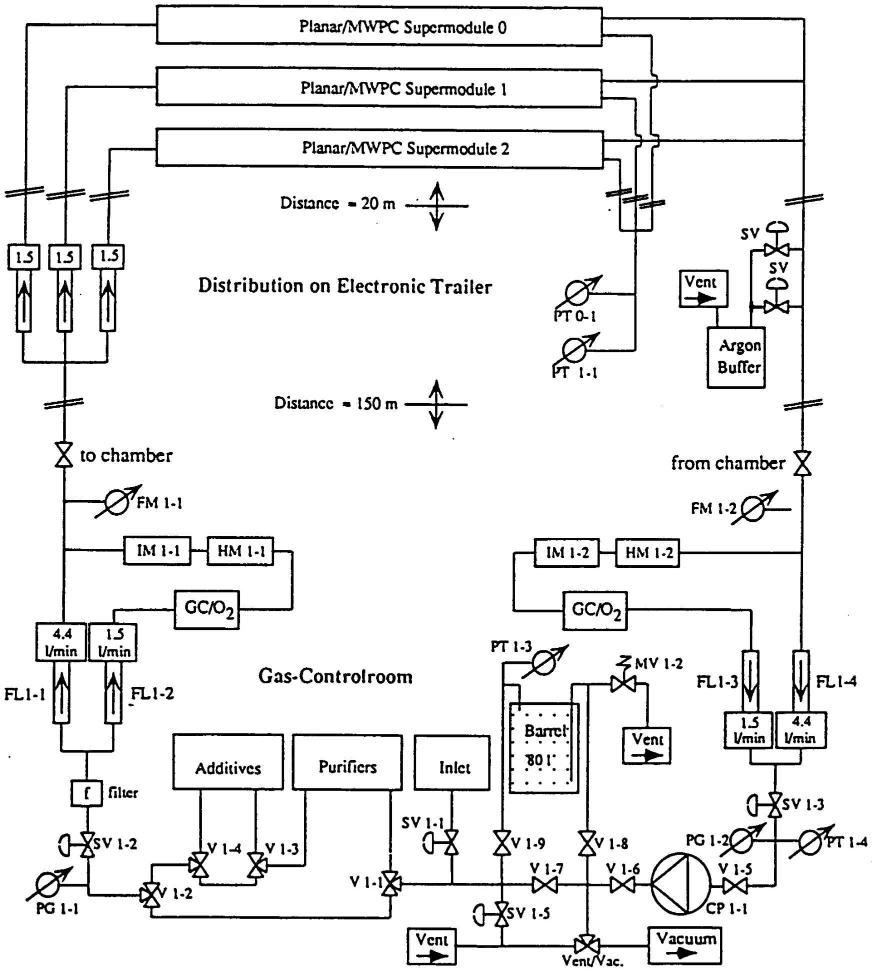

Figure 3.13: The planar chamber gas systems.

the hub and are read out at both ends, enabling the radial coordinate position to be determined using charge division. The ϕ coordinate is determined from the drift time. The track segments can then be reconstructed in the radial chambers and linked to the planar segments giving tracks through the whole of the forward tracker. Particle identification is facilitated by measurements of $\frac{dE}{dx}$.

FMWPCs

The FMWPCs are used to give a fast trigger for forward tracks. The FMWPCs consist of the three drift chambers each of which consists of two wire planes interleaved with three cathode planes separated by 4 mm in z. The fast triggering is achieved by reading out the cathode pads. The radial size of the pads varies between 18 mm at the inner radius to 32 mm at the outer. The inner 16 pads cover an azimuthal angle of $\frac{\pi}{8}$, the outer 4 cover $\frac{\pi}{16}$. There are also two planes of cathode pads in z that are read out, the pads are offset by one half of the pad size in r to increase the effective polar angle resolution.

3.4 Calorimetry

A simple calorimeter consists of two main parts, a material that causes a particle to shower (the absorber), interleaved with a sensitive material which measures the development of the shower.

For high energy electrons and photons interacting with an absorber, the processes of pair production and bremsstrahlung dominate to produce more electrons and photons. The secondary particles then created undergo the same reactions initiating a shower of particles. The development of the shower depends upon the number of radiation lengths of the material it traverses. A radiation length, (X_0), is defined as the mean distance in which a high energy electron loses all but e^{-1} of its initial energy. As the shower progresses and the the energies of the produced particles decrease, the main losses become due to ionization. If the shower is fully contained in the calorimeter then by measuring the total ionization, an estimate can be made of the energy if the incident particle.

For strongly interacting particles, the interactions are dominated by inelastic nuclear collisions. This has the result of producing secondary hadrons which can then undergo further such interactions and a shower develops. The development of a hadronic shower is governed by the interaction length (λ_i) of the material which is usually far greater than X_0. The cascade finally ends when the produced particles have sufficiently small momentum to enable them to be stopped by ionization. It is due to this that hadronic showers are typically more penetrating in depth and have a greater lateral size. About 20% of the energy of an incident hadron however, is lost through the excitation or break up of nuclei, resulting in the production of low energy photons that cannot be detected. This means that most calorimeters have a better response for electromagnetic particles than hadrons of the same energy and this must be corrected.

3.4.1 H1 Calorimetry

There are four separate calorimeters in the H1 detector, the Backward Electromagnetic Calorimeter, the Liquid Argon Calorimeter, the Tail Catcher and the Plug Calorimeter. Figure 3.14 shows the positions of several of these calorimeter systems within the H1 detector.

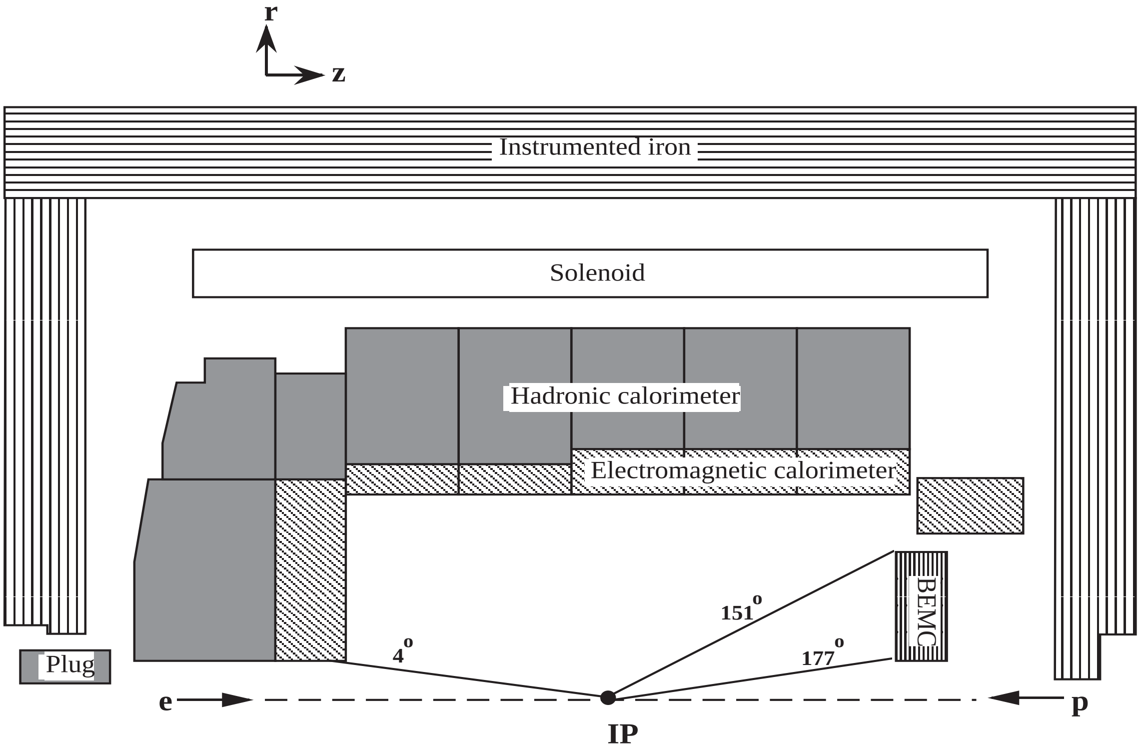

Figure 3.14: The H1 calorimetry detector systems.

3.4.2 The Backward Electro-Magnetic Calorimeter

The BEMC, shown in Figures 3.15 and 3.16, consists of 88 stacks, 64 of which are square in cross–section with a length of 159 mm. On the outer edge of the detector the stacks are triangular and trapezoidal in shape, with triangular stacks around the beam–pipe. Each stack is divided longitudinally into 2.5 mm plates of lead inter-spaced with 4 mm thick sheets of scintillator. There are a total of 50 sampling layers. The scintillators are then read out using wavelength shifters (WLS) that run the entire length of the stack. For the square and trapezoidal stacks four WLS are positioned so that there are two either side of the stack making it possible to find the position of the centre of gravity of a cluster in the BEMC with a precision of the order of 15 mm. On the other two sides of these stacks WLS are used to read out the last 15 sampling layers, allowing a calculation of the depth of the cluster within the stack. The “triangle” stack WLS run the length of the two short sides of the stack.

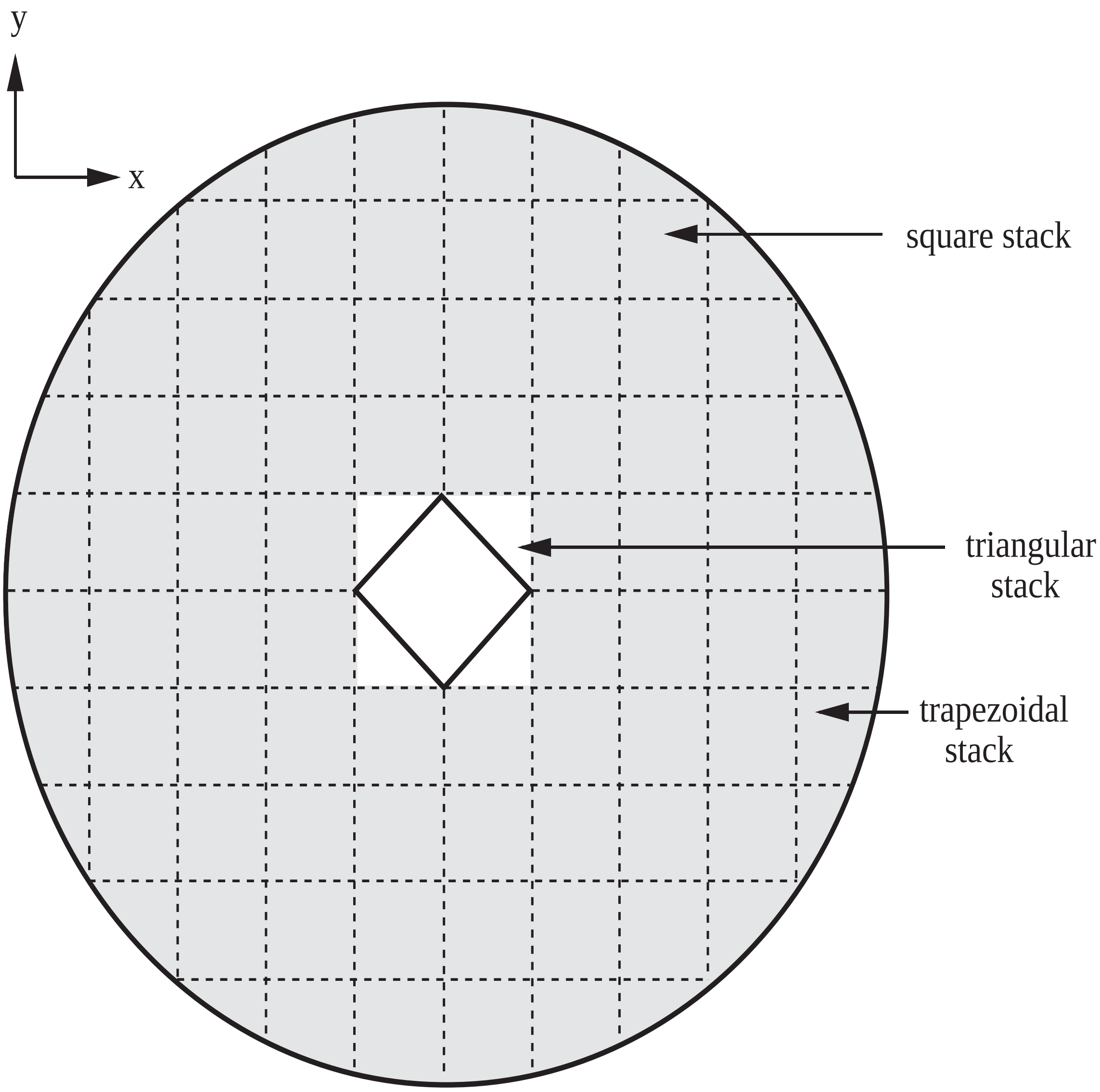

Figure 3.15: Schematic of the Backward Electro-Magnetic Calorimeter.

The BEMC has an effective depth of $22.5\,X_0$ and $0.97\lambda_I$, resulting in an

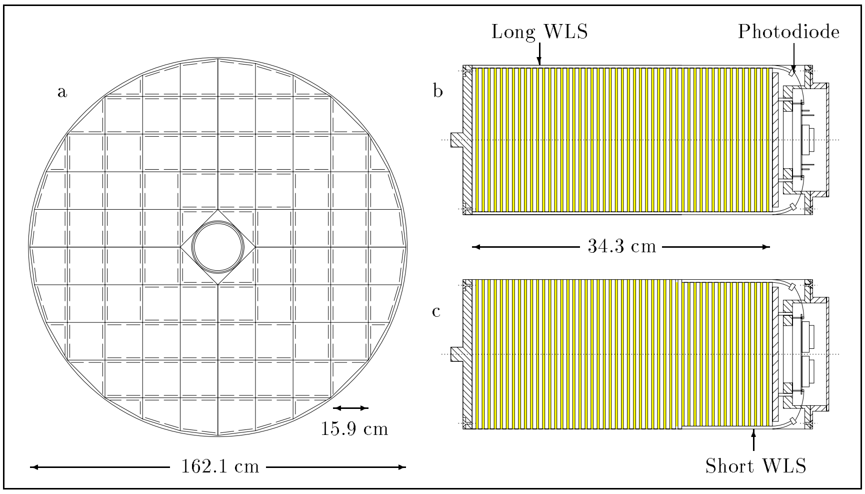

Figure 3.16: Side and end views of the Backward Electromagnetic Calorimeter.

excellent containment of electro-magnetic showers but a poor response to hadronic particles (approximately 30% of incident hadrons leave no significant signal in the BEMC and only $\sim$ 30% of the energy of interacting hadrons is contained).

The resolution of the BEMC is $\sigma_E/E = 10\%/\sqrt{E} \oplus 0.42/E \oplus 0.03$. The overall calibration scale of the BEMC is determined from the kinematic peak obtained from DIS events.

The BEMC is also used for triggering events. The most significant trigger from the BEMC is the BEMC single electron trigger (BSET). For a trigger bit to be set, the signal from the 4 wavelength-shifters on each stack are summed and analysed to provide the energy deposited in the stack for a given bunch crossing. If the energy in the stack is above a high threshold of 2.3 GeV and the stack is the highest energy stack then this is used as a cluster seed. The neighbouring stacks with an energy above a low threshold of 1.3 GeV (which is just above the noise level) are added to form the cluster. .

3.4.3 The Liquid Argon Calorimeter[1]

The Liquid Argon Calorimeter is the main calorimeter in the H1 detector and covers an angular range of $4^o < \theta < 153^o$ and has both an electromagnetic (EMC) and a hadronic section (HAC). It is housed within the main H1 solenoid in order to reduce both the amount of dead material in front of the calorimeter and its overall size and weight. The liquid Argon technique was chosen as it provides a stable response and gives high granularity allowing good separation of hadronic and electromagnetic showers through their shower profiles such that appropriate calibration constants and correction factors can then be applied.

The EMC consists of 2.4 mm thick plates of lead interleaved with 2.35 mm gaps filled with liquid Argon and contains a plane of readout pads from which the signals are taken. The total depth of the EMC is between $20X_0$ and $30X_0$ and has a resolution of $\sigma_E/E = 12\%/\sqrt{E} \oplus 1\%$, where E is in GeV .

The HAC consists of 19mm stainless steel plates which are separated with two volumes of liquid Argon, each 2.4mm thick. The signals are read out from planes of pads on either side of the board separating the two liquid Argon volumes. The total thickness of the HAC varies between $5\lambda_i$ and $7\lambda_i$ and the resolution is $\sigma_E/E = 50\%/\sqrt{E} \oplus 2\%$, where E is in GeV .

For 1994 data taking there was an additional overall normalisation uncertainty in the energy scales, this was $\sim 2\%$ for the EMC and $\sim 5\%$ for the HAC .

3.4.4 The Tail Catcher

In order to measure the energy of hadrons leaking out of the liquid argon calorimeter and the BEMC, eleven of the sixteen layers of streamer tubes in the iron return yoke are equipped with readout pads. The resolution of the system is $\sim \sigma_E/E = 100\%/\sqrt{E}$, where E is measured in GeV .

3.4.5 The Plug Calorimeter

The plug calorimeter is designed to close the gap of acceptance between the beam pipe and the most forward part of the liquid argon calorimeter in the angular region $0.62^o < \theta < 3.32^o$. It consists of nine layers of copper absorber interleaved with eight layers of silicon detectors. The relatively poor resolution of the plug of $\sim \sigma_E/E = 150\%/\sqrt{E}$, where E is measured in GeV , is due to coarse sampling, leakage and the large amount of dead material in front of the detectors that is not fully understood.

3.5 Muon Detection

The magnetic field of the main H1 solenoid is contained, outside the solenoid, in an iron yoke. The iron forms the main structural component of the H1 detector and is also instrumented with 16 layers of Limited Streamer Tubes (LSTs) which are interleaved with 10 layers of iron.

Each LST is a plastic tube with a square cross-section of 1 cm^2 with a single wire running down the middle. The signal is read out either from the wires or from pads or strips that cover the tubes. The threshold energy for a penetrating muon to be reconstructed in the instrumented iron is 1.2 GeV.

In the forward region, $3^o < \theta < 17^o$, for muons with momentum greater than 5 GeV, the forward muon spectrometer is used to enhance muon detection. This detector consists of three drift chamber planes mounted on both sides of a toroidal magnet and provides a momentum measurement up to 200 GeV.

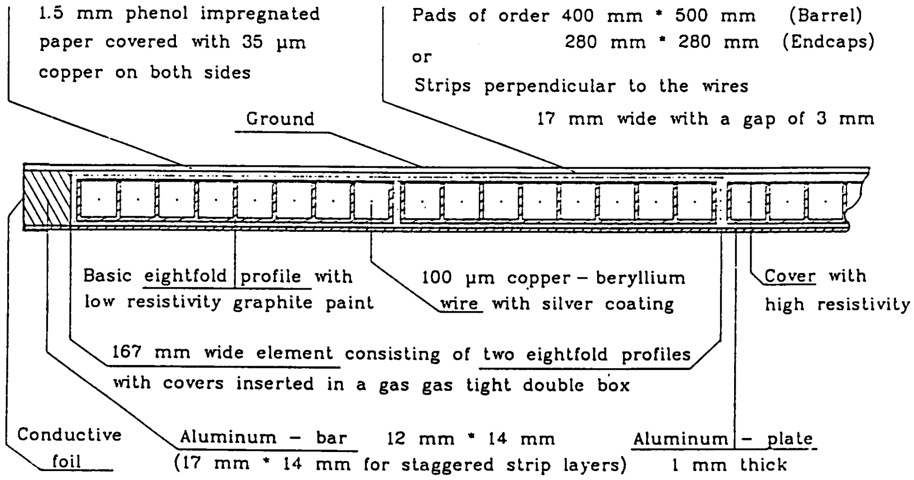

Figure 3.17: Diagram showing the muon chambers.

3.6 Scintillator Systems

There are two arrays of scintillators used in the backward region of the H1 detector to veto triggers due to proton beam induced background.

3.6.1 The Time of Flight Counters

The Time of Flight counters (ToF) are located upstream of the interaction at $z \sim -2$ m. This choice of position represents a compromise between good coverage of the detector and time resolution which is $\sim$ 4ns . It consists of two planes of plastic scintillator mounted perpendicular to the beam pipe. If a proton interacts

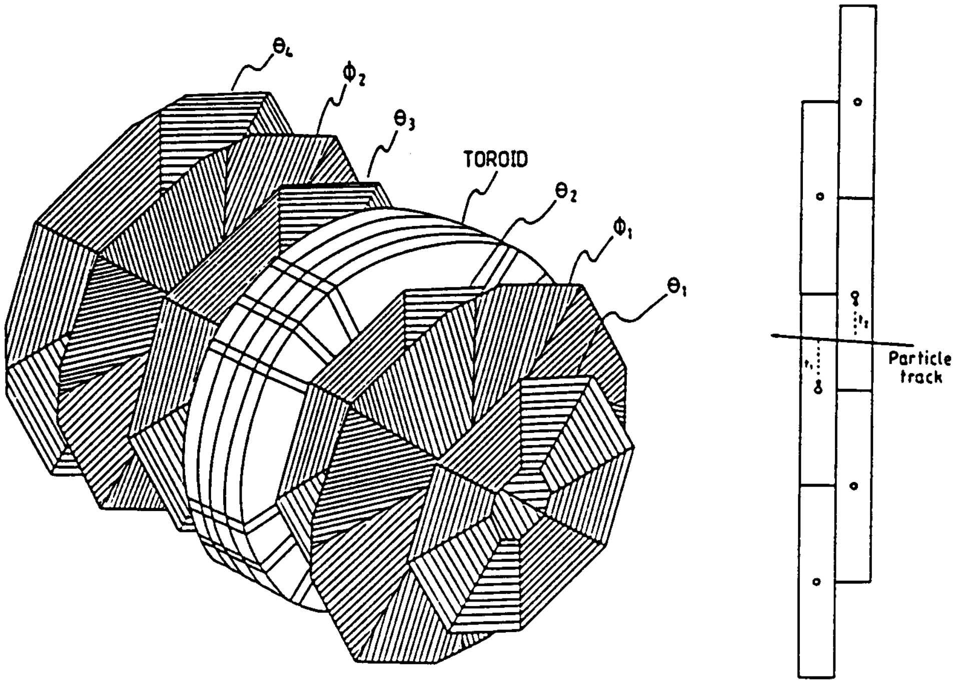

Figure 3.18: Diagram of the Forward Muon detection systems.

with either residual gas or the beam wall before entering the H1 detector, it initiates a spray of particles from that interaction which will pass the ToF at approximately the same time as the proton bunch. For a genuine $e-p$ collision that occurs within the nominal interaction region, the particles produced in this collision will reach the ToF later by $\sim$ 13ns and this time difference is therefore used to veto beam-induced background.

3.6.2 The Veto Walls

Located at $z \sim -6.5$m and $z \sim$ -8.1m are the Inner and Outer Veto Walls. Both of these operate in a similar way to the ToF to reject beam-induced background events. The Outer Veto Wall covers an area of 5 x 4 m^2 and has a timing resolution of $\sim$ 8ns. The Inner Veto Wall extends only 1m from the beam pipe and has a timing resolution of $\sim$ 3ns.

3.7 The Luminosity System

The luminosity in H1 is determined from the Bethe-Heitler process $ep \rightarrow \gamma ep$ which has a large and precisely calculable cross-section . The main source of background is bremsstrahlung from the residual gas in the beam pipe, which has an even larger cross-section and the same signature as $ep \rightarrow \gamma ep$ events. This background was measured using electron "pilot" bunches to be about $\sim$ 10% for 1994 data taking and the luminosity measurement is corrected for this.

The Luminosity System in H1 detects scattered electrons and outgoing photons in coincidence. It contains two Cherenkov counters: the electron tagger (ET) and the photon detector (PD). Since the angular distribution for electrons and photons produced in the Bethe-Heitler process is strongly peaked in the direction of the incident electron beam, the detectors are located near to the beamline and far from the interaction point. Figure 3.19 shows the beam line in the $-z$ direction illustrating the positions of the ET and OD.

A lead absorber and water Cerenkov counter (VC) protect the PD from synchotron radiation in the $+z$ direction and it is shielded from behind by an iron wall from proton beam induced background. The VC can also be used as a veto to select events where the PD signal is due to charged particles or where the photon showers before entering the PD.

A further use for the Luminosity System is the identification of photoproduction events where the electron enters the acceptance of the the ET.

The statistical error on the luminosity measurement is negligible and the total systematic error is dominated by uncertainties in the acceptance calculation, background subtraction, trigger efficiency and energy calibration of the detectors to give a total systematic error for 1994 data taking of ~ 1.5% .

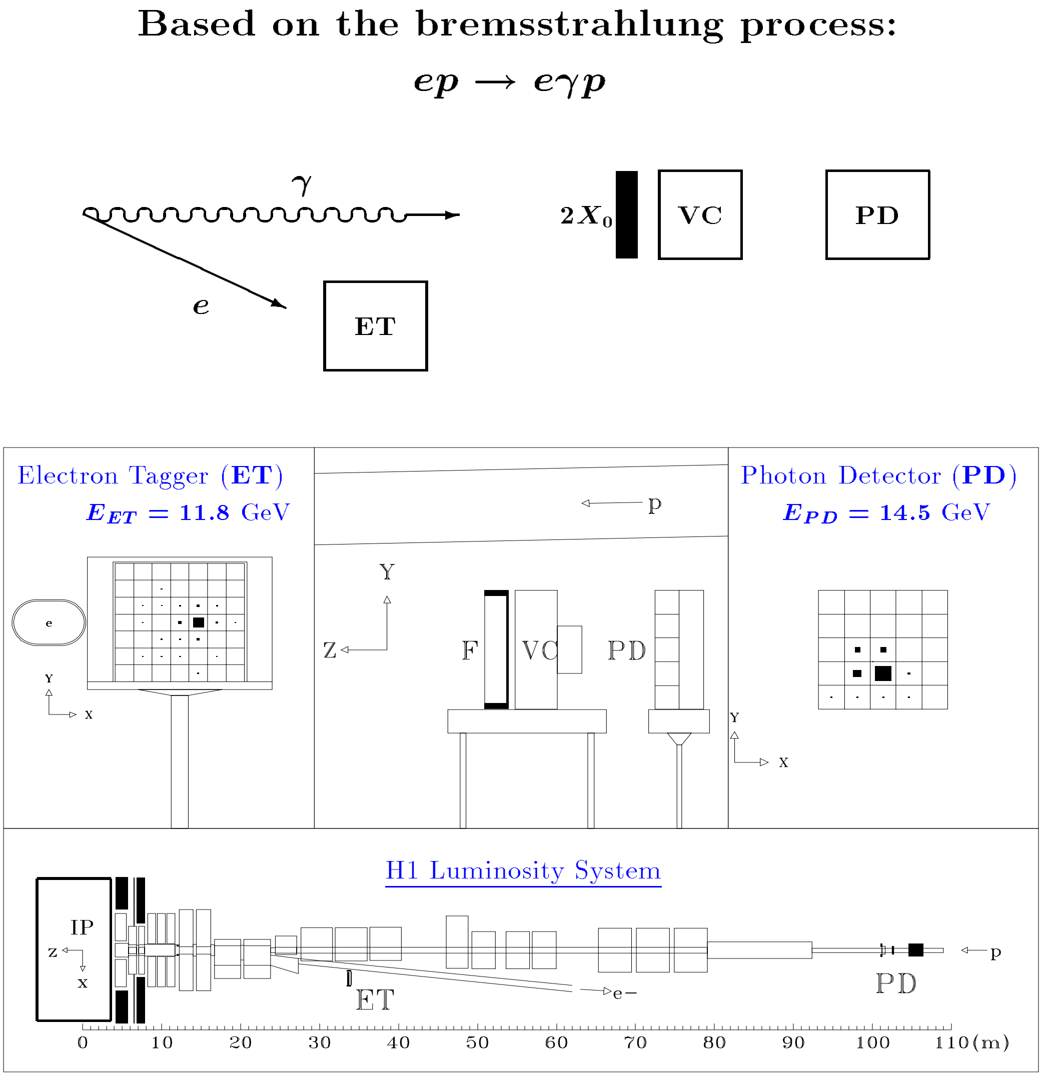

Figure 3.19: An $x - z$ view of the luminosity monitors.

Chapter 4

Event Selection

4.1 Introduction

The data presented were collected during the proton-positron collisions of the 1994 HERA running period. The corresponding integrated luminosity is 1.3 pb^{-1}. Positrons were used instead of electrons since any positively charged ionic pollution produced in the beampipe from an imperfect vacuum would tend to drift away from the beams of like electric charge, consequently improving the leptonic beam lifetime. Positrons of energy E_{el}=27.6 GeV were collided with protons of energy E_p=820 GeV resulting in a centre of mass energy, $\sqrt{s}$=300.9 GeV available.

4.2 Trigger Selection

Bunch crossings occur within H1 with temporal separation of only 96 ns and the read-out time of all the sub-detectors is around 1 ms. It is therefore important to filter out background events as quickly as possible before reading out all the information available. Data from the last 27 to 35 bunch crossings, depending on the individual detector subsystem, are stored in a 'pipe-line' memory. If the hardware logic at the first level trigger decides the event is possibly an interesting ep collision then the pipe-line is stopped and read out, rendering the detector effectively 'dead' during this period.

The on-line background rejection was envisaged to consist of four separate stages of sophistication, with preceding levels taking less time to make decisions on whether or not to reject an event. During the data-taking of 1994 only levels 1 and 4 were implemented.

4.2.1 Level 1 Trigger

There are a number of different first level trigger elements designed to recognise different aspects of an event which may suggest that it contains interesting physics. The L1 trigger attempts to identify low Q^2 DIS event candidates using the BEMC Single Electron Trigger (BSET)[30]. The purpose of this trigger is to recognise scattered positrons in the BEMC.

The BEMC[31] is cylindrical, or circular when viewed in the x,y-plane. It has 50 layers of scintillator interleaved with 49 layers of lead in the z-direction. The circular cross-sectional area is divided into 88 sections (see Figure 3.15), forming 'stacks' in the z-direction. Most of these stacks are square prisms but at the perimeter of the cylinder they are trapezoidal prisms. The cylinder has a diamond-shaped hole extending along its axis and the innermost stacks are triangular prisms.

The BSET trigger searches for a stack in which energy deposited exceeds a threshold of $\sim$2.3 GeV. If all its neighbouring stacks detected energy exceeding a second threshold of $\sim$1.3 GeV, above the noise level, then all these energies are clustered. The pedestal subtracted noise level is found to be 140 MeV per stack. This is a fluctuation and can be positive or negative. Combining the noise from several stacks is therefore achieved by addition in quadrature. Since a cluster usually contains 9 stacks the noise per cluster is at the level of 420 MeV[32]. An event is then designated a low Q^2 DIS candidate if it contains at least one BEMC cluster with energy greater than 7 GeV.

4.2.2 Level 4 Trigger

The L4 algorithm employs a fast version of the H1REC[33] program to reconstruct the events. Events accepted by the BSET trigger at L1 are then rejected if they contain three or more reconstructed tracks in the CTD which originated from a point outside the detector region and having a negative z-position. Events with only one or two such tracks but with no additional tracks originating from the nominal interaction point are also rejected. These events are likely to be due to interaction of the proton beam with either the beam-pipe or residual gas within it (see Figure 4.1).

4.3 Event Reconstruction

The full read-out information from accepted events is employed by the H1REC package which attempts to reconstruct the scattering process which occurred,

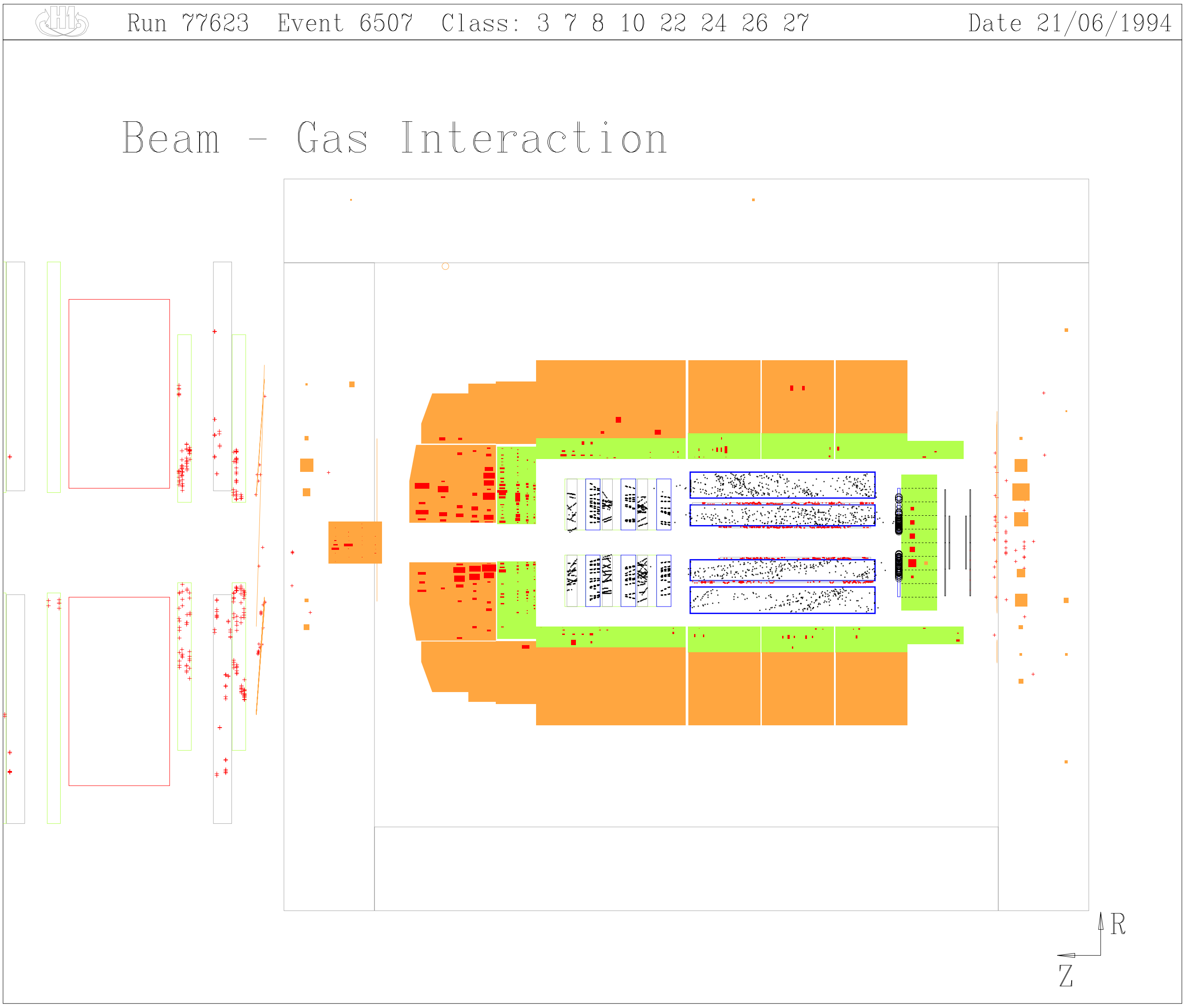

Figure 4.1: A typical beam-gas event with a vertex lying outside the main H1 detector volume.

associating 4-momenta to the tracks and clusters deposited by the emerging particles.

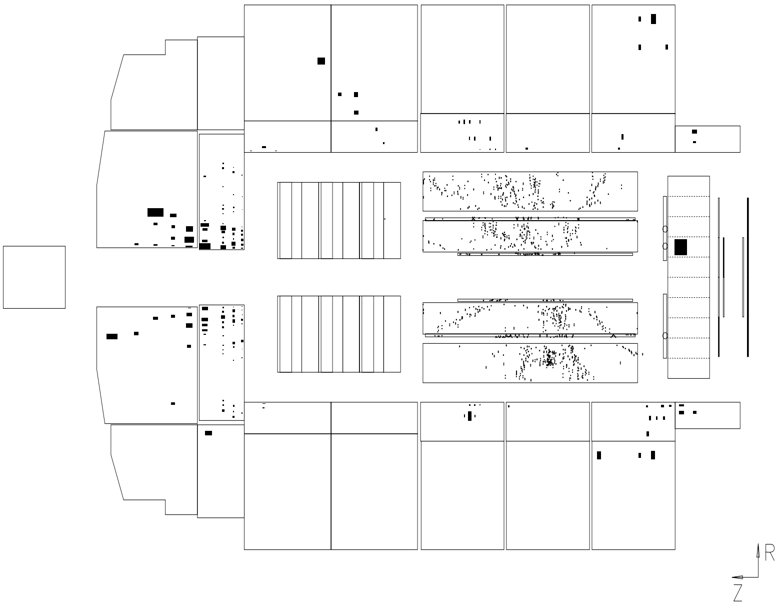

Figure 4.2: A typical low Q^2 DIS event. A substantial deposit of energy from the absorption of the scattered positron is visible in the BEMC. Tracks clearly emanate from the nominal interaction point. The energy deposits in the very forward calorimetry are due to the proton remnant.

4.3.1 Central Tracking

Digitized charge pulses due to the passage of an ionizing particle are integrated to obtain a total deposited charge, Q, and the leading edge of the pulse gives a time, t, at which the pulse arrived at the wire. The distance of the track from the wire may be deduced from knowledge of this time. The position of the track along the direction of the wire is arrived at using the charge division method. A pattern recognition algorithm is employed to find track segments consisting of spacepoints which lie on a circle in the x,y-plane. Different track segments are then combined to form candidate tracks which are then fitted with helical trajectory parameters. The central track selection constraint cuts employed were:

- $p_T > 0.15\,GeV$, ensuring low momentum tracks which might spiral around on themselves in the magnetic volume are cut out.

- $\theta \leq 158°$, eliminating the track of the scattered positron from the track sample.
- $d.c.a. < 2.0\,cm$. The distance of closest approach of the circle described by the track in the x,y-plane to the primary vertex position is limited in order to reject tracks originating at a secondary vertex.
- $\frac{\delta\kappa}{\kappa} < 1.0$, eliminating any tracks which are of blatantly poor curvature measurement and therefore transverse momentum resolution.

4.3.2 Forward Tracking

Selecting reliable tracks in the Forward Tracking Detector is especially difficult. In the forward region there is additional danger of contamination by tracks originating not from the interaction point but from secondary interactions with dead material which exists between the endwall of the Central Jet Chamber and also from the collimator labelled C4 which exists around the beamline and within the Forward Tracking Detector(see Figure 4.3). A detailed description of track finding in the FTD is available in [29]. In order to eliminate secondaries from the sample a number of constraining cuts were applied to the tracks:

- $p > 0.5\,GeV/c$. This cut rejects many of the secondaries which are typically of low momenta, but is not so high as to reject good tracks, which have a steeply falling distribution.
- $\theta > 8°$, so as not to include tracks at the edge of the angular acceptance where reconstruction efficiency deteriorates.
- R0 $< 5.0\,cm$. R0 is the radial distance from the vertex of the position on the track where z=0. It is used analogously to the d.c.a. constraint on central tracks, rejecting secondaries.
- number of forward planar segments ≥ 2, in order to ensure good reconstruction.
- $\frac{\chi^2_{track}}{d.o.f.} \leq 25.0$, rejecting poor track fits.
- $\frac{\chi^2_{vertex}}{d.o.f.} \leq 10.0$, rejecting poor fits of the track to the vertex.
- $\frac{\delta p}{p} < 1.0$, eliminating tracks which are of poor momentum resolution.

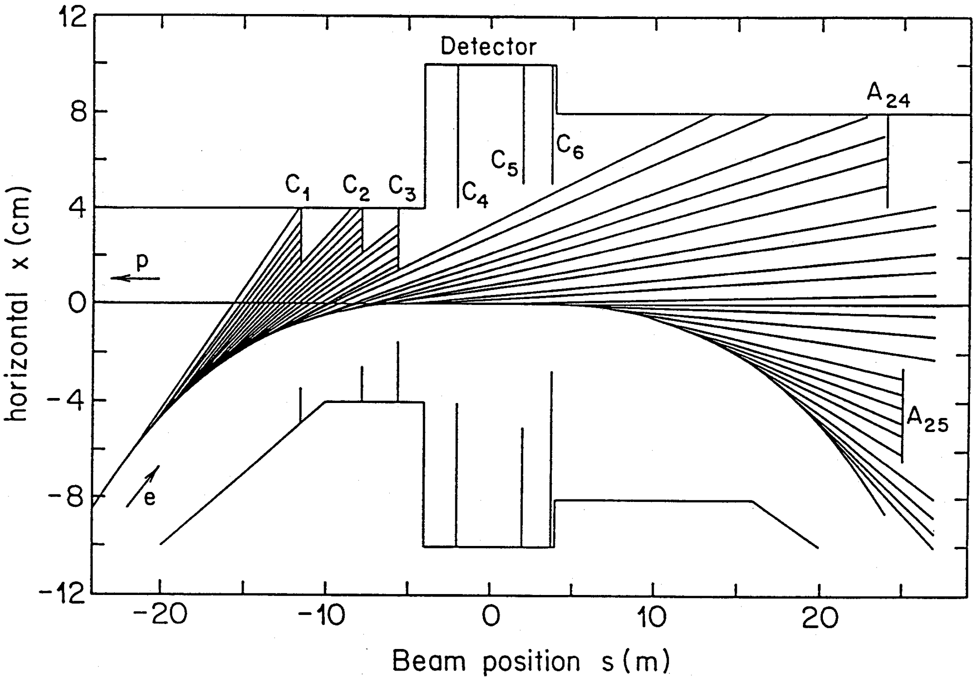

Figure 4.3: Diagram showing the beam collimators near the H1 detector systems. Significant levels of synchrotron radiation arise from the charged lepton beam necessitating shielding of the detectors.

4.3.3 Combined Tracks

When all the central and forward tracks are reconstructed an attempt is made to combine forward and central tracks which have similar parameters. A number of cuts are required in order to make a combination:

- $p_T > 0.15\,GeV/c$, ensuring the removal of low momentum tracks, which might spiral around on themselves in the magnetic volume.
- $\frac{\chi^2_{vertex}}{d.o.f.} \leq 10.0$, rejecting poor fits of the track to the vertex.
- $\frac{\chi^2_{link}}{d.o.f.} \leq 15.0$, rejecting combined candidates which do not demonstrate a sufficiently strong link between forward and central parts.
- $\frac{\delta p}{p} < 1.0$, eliminating tracks which are of poor momentum resolution.

When a combination is successfully made then it is ensured that there is no double counting. The combined track parameters are kept, and the corresponding central or forward track parameters discarded.

Distributions of track quality variables are shown in Figures 4.4, 4.5 and 4.6.

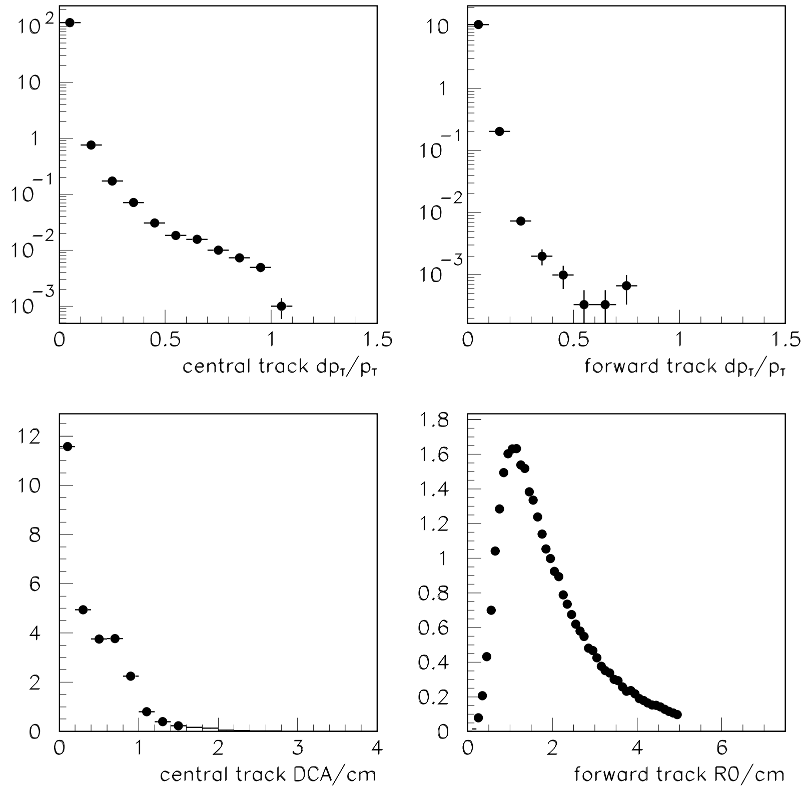

Figure 4.4: Control plots of track selection quantities after application of track quality constraints. Fractional errors on transverse momenta of central(upper left) and forward(upper right) tracks are shown with a logarithmic ordinate scale showing a strong peak indicating low errors. The central track DCA distribution(lower left) and the forward track R0 distribution(lower right) are also presented. In each case the ordinate scale shows the number of tracks per event which satisfy the relevant track selection constraint.

4.3.4 Vertex Reconstruction

The x,y-position of the collision vertex is known to be stable over several runs and is determined by a fit to all long, high momentum CJC tracks which can be extrapolated close to the nominal interaction point in a given run. However, the z-position needs to be determined every event. Using the x,y-constraint of the vertex, tracks are fitted in the r,z-plane to determine the z-position. The

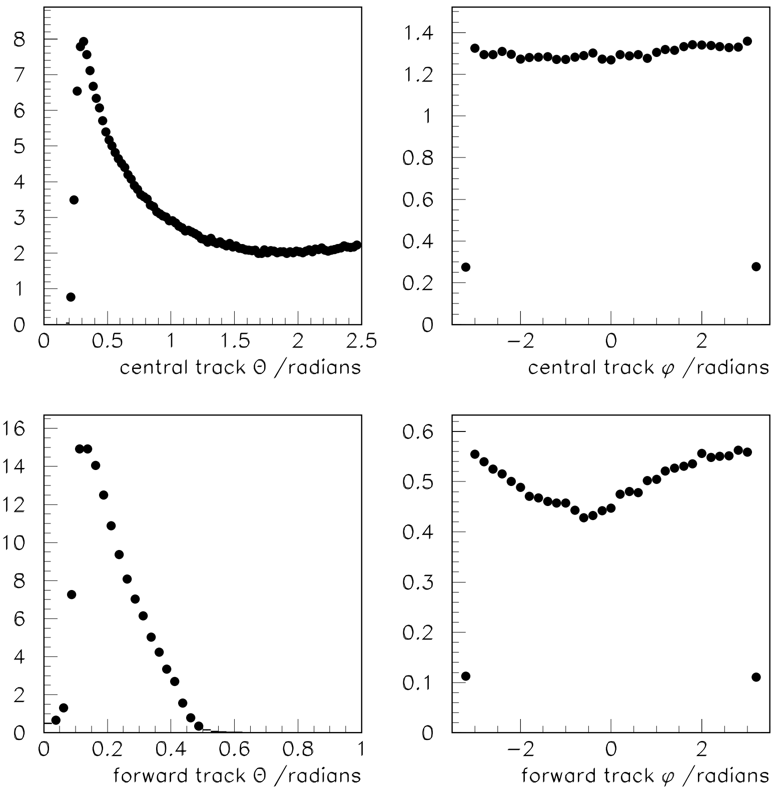

Figure 4.5: Theta(left) and phi(right) distributions of central(above) and forward(below) tracks. The ordinate scales shows the number of tracks per event.

z-vertex distributions from the data, and from Monte Carlo modelling, are shown in Figure 4.7.

4.4 Reconstruction of Kinematic Quantities at HERA

In Neutral Current electron/positron-proton DIS the kinematic variables may be arrived at indirectly through the measurement of some related experimental observables. At HERA the 4-momentum of the incident electron/positron is known to a high degree of accuracy and its energy and direction after scattering may be measured by the detector systems of an experiment surrounding the collision point. If the incident and scattered positron relativistic energies are E_e and E'_e

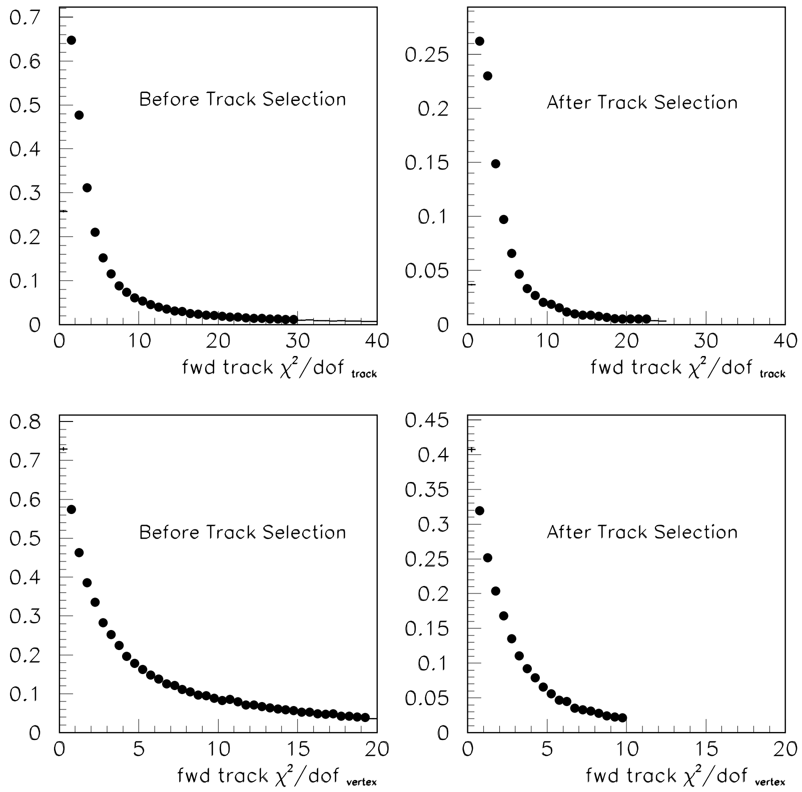

Figure 4.6: The $\chi^2/d.o.f.$ distributions for the fit to forward tracks(upper plots) and for the forward track fit to the vertex(lower plots). In each case the left hand plot shows the distribution before track selection and the right hand plot shows the distribution after selection. The vast majority of tracks are well within the constraints and are of good quality. The ordinate scales shows the number of tracks per event.

respectively and the incident proton is also noted to be highly relativistic, then it is easy to express the Lorentz invariants in terms of the energy and direction of the scattered positron, E'_e and θ_e:

$$Q^2 = 4E_eE'_e\cos^2\left(\frac{\theta_e}{2}\right) \tag{4.1}$$

$$y = 1 - \left[\frac{E'_e}{E_e}\right]\sin^2\left(\frac{\theta_e}{2}\right) \tag{4.2}$$

$$x = \frac{E_eE'_e\cos^2\left(\frac{\theta_e}{2}\right)}{E_p[E_e - E'_e\sin^2\left(\frac{\theta_e}{2}\right)]} \tag{4.3}$$

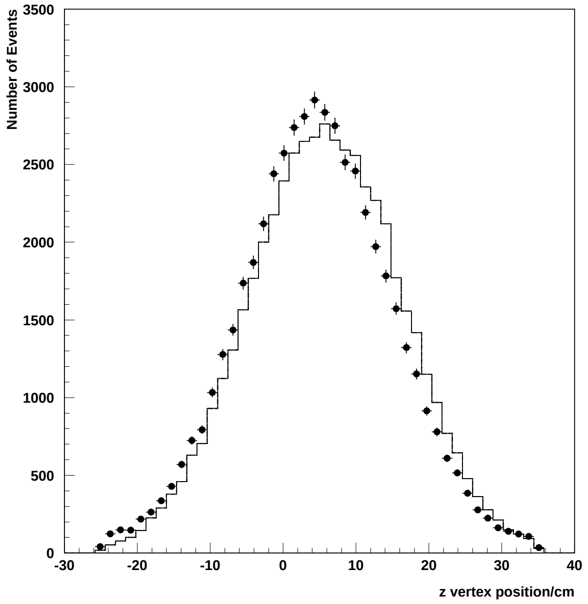

Figure 4.7: The z-vertex distribution for the low Q^2 data(points) and the CDM Monte Carlo(full line).

This method of reconstruction is known as the electron method and is employed in the work presented. There are other methods and they are described elsewhere.

4.5 Off-line low Q^2 DIS Event Selection

In this analysis deep inelastic scattering(DIS) events have been selected in the range $5 < Q^2 < 50\ GeV^2$, in which the scattered positron is observed in the BEMC. The events were triggered by detection of at least 4.0 GeV within the BEMC. In order to exclude events originating from beam gas interactions and off-course beam particle collisions with the beampipe walls, as well as the background from photoproduction, a number of cuts have been applied to the data sample. The scattered positron, defined as the most energetic BEMC cluster, must have an energy E'_{el} greater than 12 GeV and a polar angle θ_{el} below 173° in order to ensure high trigger efficiency and a small photoproducton background. Diffractive events, which involve the transfer of a colourless object known as the pomeron and result in a rapidity gap with minimal activity in the forward region are excluded from this study by requiring that an energy deposit $E_{fwd} > 0.5$ GeV is detected in the calorimetry within the forward angular range $4.4° < \theta < 15.0°$. The resulting kinematic range covered is displayed in Figure 4.8.

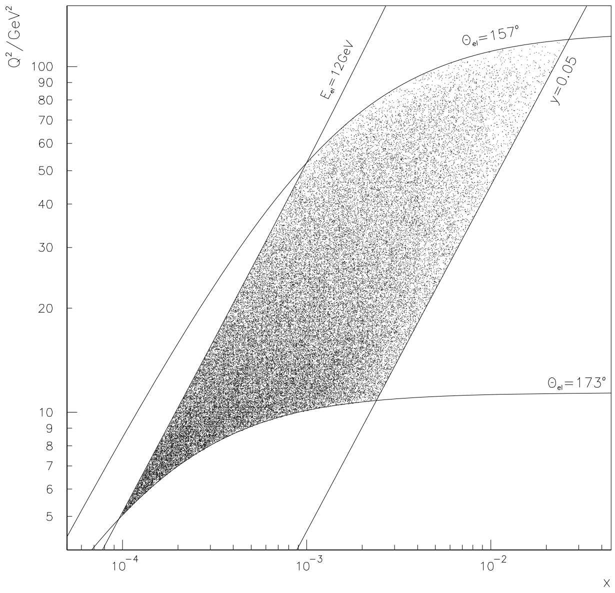

Figure 4.8: The x, Q^2-plane showing the influence of kinematic cuts on the DIS data sample.

In order to optimise luminosity collection the protons and leptons are accelerated at HERA in many bunches. However, the procedure by which this compression is achieved can lead to the formation of satellite bunches within the tails of the main proton bunches. The particles in these satellite bunches may interact with the lepton beam outside of the designated collision region, and would not be sufficiently contained in the detector volume of H1. In order to exclude these events as well as those originating from beam gas interactions and beam-wall interactions, the z-vertex position, as reconstructed from charged tracks, must lie within 30 cm of its average value. An additional method employed in rejecting some of these background events was to require no veto from the time-of-flight(ToF) counters.

Photoproduction events[34], in which the scattered lepton escapes undetected down the beampipe, may mimic low Q^2 DIS events if a hadron fakes the signal of a scattered lepton in the BEMC. While the BEMC was very opaque to electrons or positrons, having a depth of 22.5 X_0 and comparatively transparent to hadrons[1] with a depth of 0.97 λ_I the photoproduction events occur

---

[1] In addition the response to hadronic showers was low with approximately 30% of incident hadrons leaving no significant signal and only about 30% of the energy of interacting hadrons being contained.

at a higher rate than the DIS events and consequently contribute a troublesome background nevertheless. As well as the E'_{el} cut described above some other cuts have been employed to reduce this background. The shape of electromagnetic showering as opposed to hadronic showering may be employed to select events with good scattered leptons. Also, association of the BEMC cluster with a BPC point is required to confirm the electric charge of the scattered lepton candidate. Specifically, the lateral size of the positron cluster, calculated as the energy weighted radial distance of the cells from the cluster centre, must be less than 4 cm, while a reconstructed BPC space point is required to lie within 3.5 cm of the cluster centre of gravity. The radial coordinate of the BPC hit must be less than 60 cm, corresponding to a scattered lepton angle above 157°, thus ensuring full containment of its electromagnetic shower in the BEMC. Further reduction of photoproduction background and removal of initial state radiation events, in which an energetic photon is radiated from the incident lepton altering its energy significantly and thereby corrupting the kinematic reconstruction via the electron method, is achieved by requiring $\sum_{i=1}^{n} (E - p_z)_i > 30$ GeV, with the sum extending over all particles i measured calorimetrically in the event.

4.5.1 The $\Sigma(E - p_z)$ Cut

For the relativistic beam particles,

$$P_z^p \approx E^p, P_z^e \approx -E^e \tag{4.4}$$

So,

$$\sum_{total} (E - P_z) = (E^p + E^e) - (P_z^p + P_z^e) \approx 2E^e \tag{4.5}$$

However, H1 is not a perfect 4π detector and particles may escape down the beampipe in the proton(+) or positron(-) directions.

$$E^{det} = (E^p + E^e) - (E^+_{lost} + E^-_{lost})) \tag{4.6}$$

$$P_z^{det} = (P_z^p + P_z^e) - (P^+_{z\ lost} + P^-_{z\ lost}) \tag{4.7}$$

But, for relativistic particles lost down the beampipe in the proton direction,

$$P^+_{z\ lost} \approx E^+_{lost} \tag{4.8}$$

And conversely,

$$P^-_{z\ lost} \approx -E^-_{lost} \tag{4.9}$$

Therefore,

$$\sum_{total} (E^{det} - P_z^{det}) = 2E^e - 2E^-_{lost} \tag{4.10}$$

In a photoproduction event the scattered positron is lost in the backward direction, so $\Sigma(E - P_z) \ll 2E^e$. If a proton from the relativistic beam interacts with a stationary particle in the beampipe or beampipe wall then $E \approx E^p$ and $P_z \approx P_z^p \approx E^p$, in which case $\Sigma(E - P_z) \approx 0$. The $\Sigma(E - P_z)$ distribution is shown in Figure 4.9.

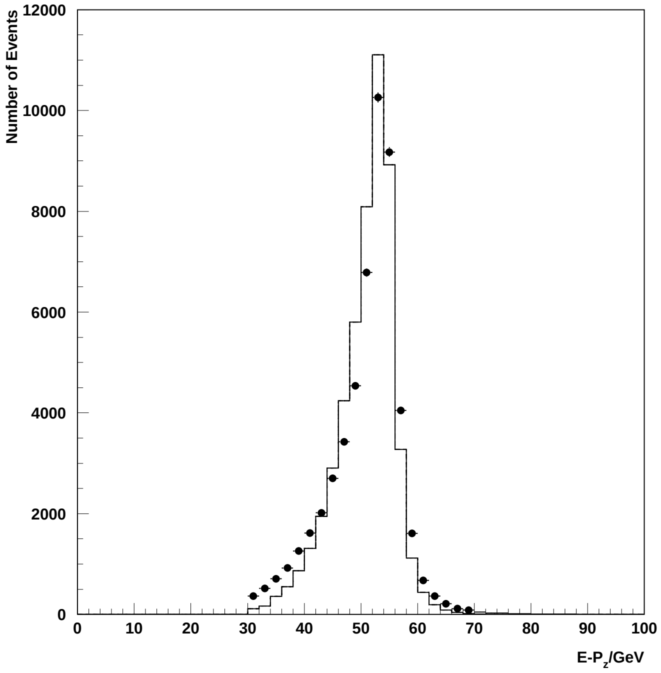

Figure 4.9: $\Sigma(E - P_z)$ distribution for the data, displayed as points, and CDM Monte Carlo prediction after simulation of the H1 detector systems, displayed as a full line.

4.5.2 The Cut in y

The kinematic variables are arrived at using the electron method employing the equations:

$$Q^2 = 4EE' \cos^2\left(\frac{\theta_{el}}{2}\right) \tag{4.11}$$

$$y = 1 - \left(\frac{E'}{E}\right)\sin^2\left(\frac{\theta_{el}}{2}\right) \tag{4.12}$$

$$x = \frac{Q^2}{sy} \tag{4.13}$$

It is easily shown that the resolution in y is given by the expression

$$\frac{\delta y}{y} = \frac{1-y}{y}\left(\frac{\delta E'}{E'} \oplus \frac{\delta\theta_{el}}{\tan\left[\frac{\theta_{el}}{2}\right]}\right) \tag{4.14}$$

In order to ensure good resolution in y a lower bound cut on y is made: $y > 0.05$.

4.6 Monte Carlo Selection

After event generation using the Monte Carlo method, simulation of the H1 detector systems and reconstruction of the event objects is performed using the same software as that used for reconstruction of true experimental data. All the event selection cuts applied to the Monte Carlo samples were the same as those applied to the data and similarly for the track selection cuts. Two Monte Carlo samples were used: LEPTO 6.4 Matrix Element + Parton Showers and LEPTO 6.4 with the Colour Dipole Model as implemented by ARIADNE 4.08. The Lund string model for hadronisation was employed in both Monte Carlo samples. Kinematic quantities and observables and their correlation between Monte Carlo generator and reconstructed levels are shown in Figure 4.10.

4.7 Summary of Event Selection

In summary, the event selection used consists of the following constraints:

- $\theta_{el} < 173°$
- $E'_{el} > 12$ GeV
- $E_{fwd} > 0.5$ GeV

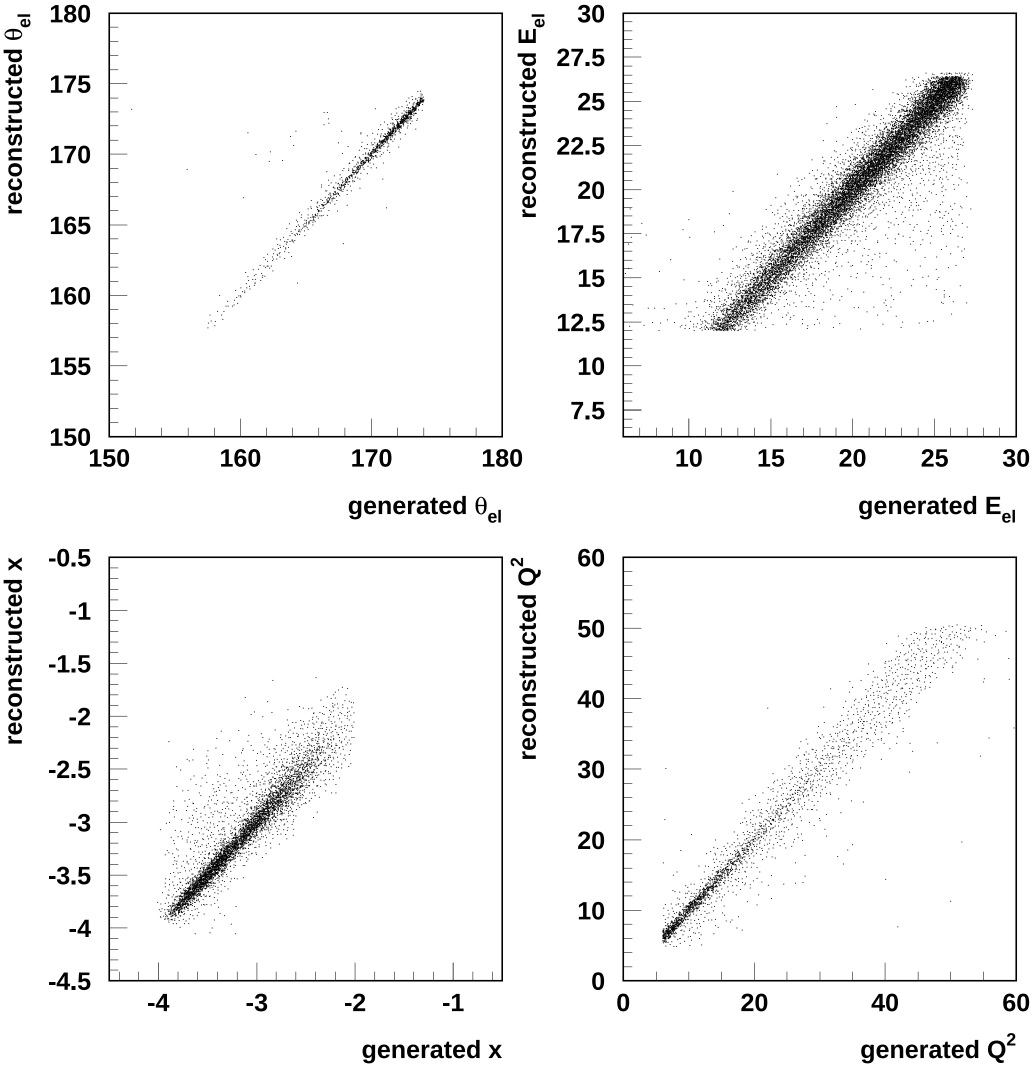

Figure 4.10: Correlation between reconstructed and generated kinematic quantities (CDM Monte Carlo).

- zvtx within 30 cm of average
- size of positron cluster < 4 cm and must be associated with a reconstructed BPC point
- radial coordinate of BPC hit < 60 cm, corresponding to a positron angle $\theta_{el} > 157°$
- events are triggered by requiring > 4 GeV in the BEMC
- no veto from ToF counters
- $\sum_{i=1}^{n} (E - p_z)_i > 30$ GeV
- $0.05 < \mathrm{y} < 0.6$

Chapter 5

Results

Results are presented for the hadronic centre of mass system(CMS), i.e. the rest system of the proton and the exchanged boson, where the direction of the exchanged boson defines the positive z'-axis. It should be noted that there is a tendency for this direction to be opposite to that of the proton and that therefore negative values of η^{cms} tend to be more "forward", or more in the proton direction, whereas η^{lab} is defined to be positive in the proton direction. If θ and θ' are polar angles with respect to the proton and boson directions respectively then pseudorapidity in the laboratory and CMS frames are defined as follows:

$$\eta^{lab} = -\ln\left(\tan\left[\frac{\theta}{2}\right]\right) \tag{5.1}$$

$$\eta^{cms} = -\ln\left(\tan\left[\frac{\theta'}{2}\right]\right) \tag{5.2}$$

By counting the numbers of measured tracks, n, entering different p_T-bins according to their reconstructed p_T a charged particle transverse momentum spectrum is formed. This is then normalised to the number of events selected, N, to form the quantity $(1/N)(dn/dp_T)$ in different x, Q^2 ranges, arranged to make use of the kinematic domain made available by the event selection cuts(see Figure 4.8). The nine x, Q^2-bins used are defined in Table 5.1. Since more negative values of η^{cms} indicate an angular region which would tend to contain partonic emission further developed along the emission ladder, the spectra are formed in different ranges of CMS pseudorapidity in order to investigate their variation in the context of the evolution of the partonic emission ladder. The results presented in this thesis are in terms of p_T^{cms}, the momentum component in the CMS frame transverse to the direction of the exchanged boson.

Bin Number	Range in x	Range in Q^2
1	0.0001-0.0002	5-10 GeV^2
2	0.0002-0.0005	5-10 GeV^2
3	0.0002-0.0005	10-20 GeV^2
4	0.0005-0.0008	10-20 GeV^2
5	0.0008-0.0015	10-20 GeV^2
6	0.0015-0.0040	10-20 GeV^2
7	0.0005-0.0014	20-50 GeV^2
8	0.0014-0.0030	20-50 GeV^2
9	0.0030-0.0100	20-50 GeV^2

Table 5.1: Definition of the 9 x, Q^2 bins in which results are presented.

5.1 Correction Factors

The measurements provided by the detector systems of the H1 experiment, as in any experiment, are not perfect in the sense that they cannot exactly identify the flux of particles emerging from the *ep* collision zone. Clearly no detector system is 100% efficient. There are boundaries within the detector arrangement which reduce the hermeticity of the experiment. And where there is good coverage the physics processes occurring within detector regions involve an element of chance as to whether or not recognisable signals are produced by particles traversing the volume. And when signals are produced numerous mathematical operations must be performed by computer programs in order to recognise a track from the many signals and accompanying noise. The algorithms cannot be perfect at recognising tracks and noise may produce fake tracks, or obscure and confuse real tracks. Therefore, the measurement of experimental variables such as p_T-spectra does not reproduce the true distribution existing in nature. It would be wrong to compare measurements directly with the best theories of nature without taking account of all the inefficiencies involved and in order to solve this problem correction factors are applied to the data.

The Monte Carlo programs already described provide predictions according to current theory for physics events occurring in collisions, their consequent emergent particles and the distribution of associated measurable variables. This is sometimes known as the distribution at “generator level”. After these particles are generated they may be passed through a detector simulation[35] which describes what signals would be produced in the detector systems given the particles generated, on an event-by-event basis. This requires a detailed description of all the various detector efficiencies and material within the experiment. Subsequently, these signals are processed by the event reconstruction programs[33] which recognise tracks and try to build up a picture of the event, as seen through the "eyes" of this particular measuring apparatus. The 4-momenta of reconstructed particles may be used to produce a physics distribution which is a full simulation of a measured data distribution. Ideally this distribution produced at "reconstructed level" would tend to that observed in the experimental data. For each bin i in a histogrammed variable a correction factor may be applied to actual measured data in order to obtain the best possible understanding of the natural distribution:

$$(Corrected\ Population)_i = (Corr.\ Factor)_i \times (Measured\ Population)_i \tag{5.3}$$

where

$$(Corr.\ Factor)_i = \frac{(Generator\ Level\ Population)_i}{(Reconstructed\ Level\ Population)_i} \tag{5.4}$$

This procedure naturally requires good Monte Carlo modelling of efficiencies, geometric acceptance and detector material. The correction factors employed here also take into account decay of particles with an invariant lifetime, τ_0, less than 8 ns (e.g. $\Lambda \longrightarrow \pi^+\pi^-$ and $K_s^0 \longrightarrow p\pi$ with $\tau_0 > 8\ ns$ are conventionally "H1 stable"). The resulting corrected data may be compared more meaningfully with the distributions generated according to a given theory since they do not depend upon a given experimental arrangement.

Plots are presented showing the bin-by-bin corrections applied to the p_T-spectra in the relevant η^{cms} ranges. Correction factors have been formed utilising Monte Carlo samples of both MEPS and CDM types with their equally weighted average used. The factors arising from both Monte Carlo types are in good agreement. In any case, a systematic error is added to the final p_T-spectra in order to account for small differences (see Section 5.4 and Table 5.7). In the ranges $1.5 < \eta^{cms} < 2.5$ and $0.5 < \eta^{cms} < 1.5$ the correction factors (shown in Figures 5.1 and 5.2) are all very close to unity and their distribution smooth and flat. In the more forward range $-0.5 < \eta^{cms} < 0.5$ the corrections are larger (shown in Figure 5.3) since it is more difficult to reconstruct these tracks. The correction factors become larger than unity because of the fall off in geometric acceptance and the requirements of the track selection leading to a reduction in tracking efficiency. This contributes to the larger statistical error bars on the correction factors of some of the less populated bins. The systematic errors on the correction factors are almost always smaller than their corresponding statistical errors (see Section 5.4).

The lowest p_T-bin ($0.0 - 0.2\,GeV/c$) may be ignored since the track selection constraint on momentum falls effectively within this bin and renders the corresponding correction factors meaningless.

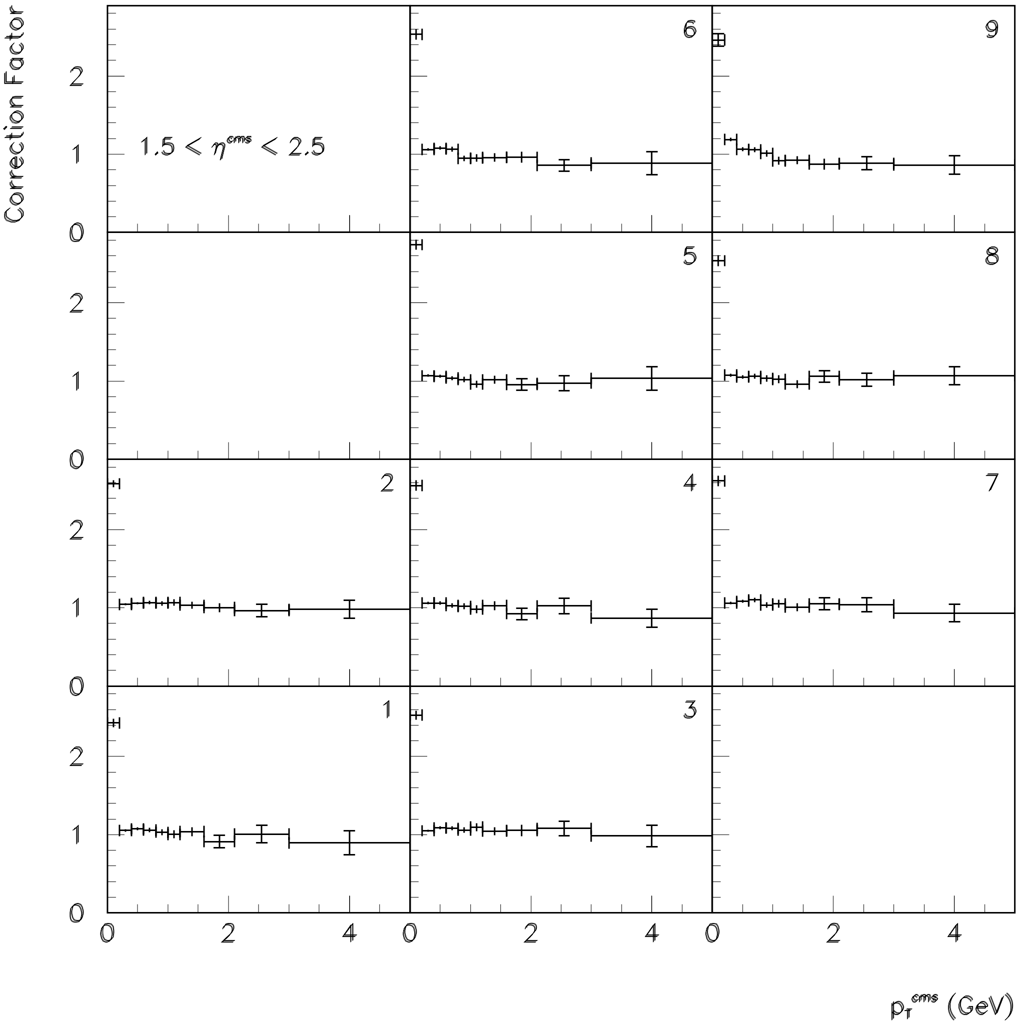

Figure 5.1: Correction factors for transverse momentum spectra in the CMS pseudorapidity range 1.5 - 2.5 shown in the nine x, Q^2-bins employed, the numbers of which are printed in the upper right-hand corners.

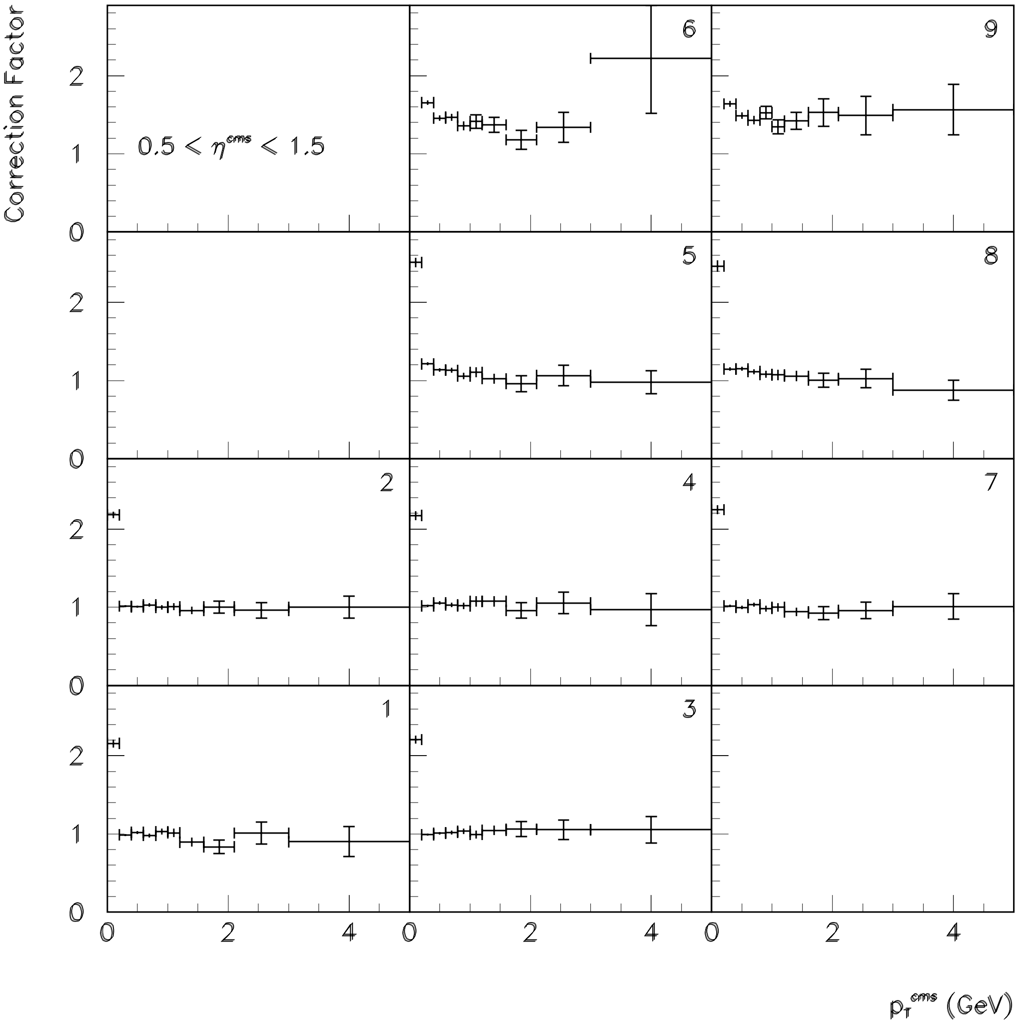

Figure 5.2: Correction factors for transverse momentum spectra in the CMS pseudorapidity range 0.5 - 1.5 shown in the nine x, Q^2-bins employed.

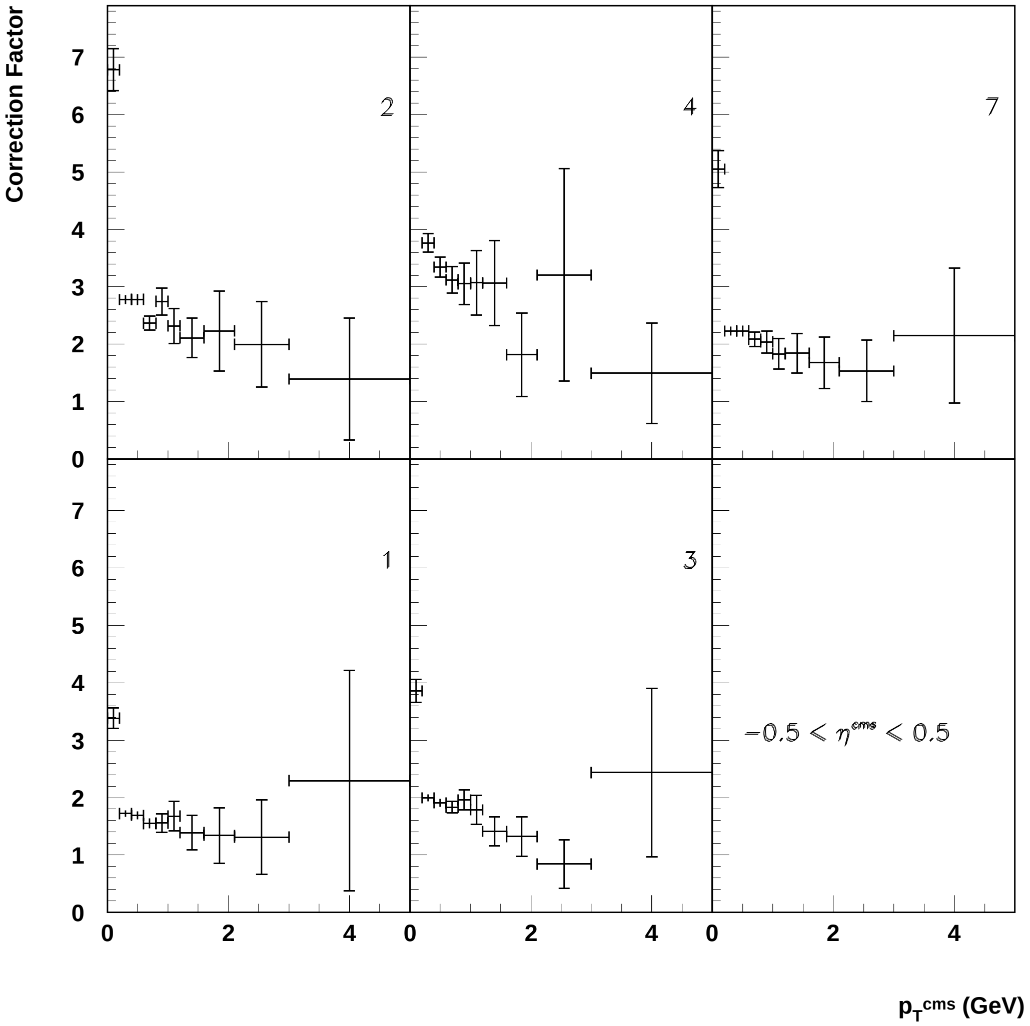

Figure 5.3: Correction factors for transverse momentum spectra in the CMS pseudorapidity range -0.5 $< \eta^{cms} <$ 0.5 shown in the five x, Q^2-bins employed in studying this η^{cms}-range.

5.2 Bin Migrations and Bin Purities

In detector simulation and track reconstruction there will be a smearing effect on our knowledge of the transverse momentum of generated particles. In a histogram of p_T the tracks contributing to a given measured p_T bin will not necessarily originate from that bin. Indeed there is likely to be migration both into and out of a given bin. These effects were monitored using Monte Carlo, comparing transverse momentum of individual tracks both at generator and reconstructed level, and bin migration matrices were formed. A global migration matrix formed using all tracks available, which passed the track selection constraints, showed very high purity in all the p_T bins. Forward tracks were also studied in isolation and a migration matrix produced from these tracks alone showed that in the highest p_T bins there is quite low forward track purity. In order to combat this problem the binning was optimised to improve forward track bin purities as much as possible. This is the reason for the increasing binwidths in the p_T-spectra, as well as combating the reduced statistics of the high p_T-bins. Tables 5.2 and 5.3 show the migration matrices for all track types as well as for forward tracks alone and the corresponding bin purities, defined as:

$$(Purity)_i = \frac{(No.\ of\ Tracks\ in\ Rec.\ Bin\ i\ Originating\ from\ Gen.\ Bin\ i)}{(No.\ of\ Tracks\ in\ Rec.\ Bin\ i\ Irrespective\ of\ Origins)} \tag{5.5}$$

5.3 Contribution of the Forward Tracking Detector

The FTD allows greater angular coverage and makes an exclusive measurement in the very forward region of H1 closer to the proton remnant, allowing coverage of an extra unit in pseudorapidity which is unattainable using the CTD. Moreover, this extra unit of rapidity is exactly central in the CMS frame where it has been proposed that BFKL effects might be more pronounced[36]. In order to demonstrate a smooth transition between the CTD and FTD systems the η^{cms} distribution of all tracks is shown in Figure 5.4.

The relative contributions of the Central Tracking Detector and the Forward Tracking Detector systems are presented as percentages of all tracks contributing in each of the kinematic bins and in different pseudorapidity regions (Tables 5.4 and 5.5). In order to make a measurement in the more forward range, $-0.5 < \eta^{cms} < 0.5$, the Forward Tracking Detector is essential.

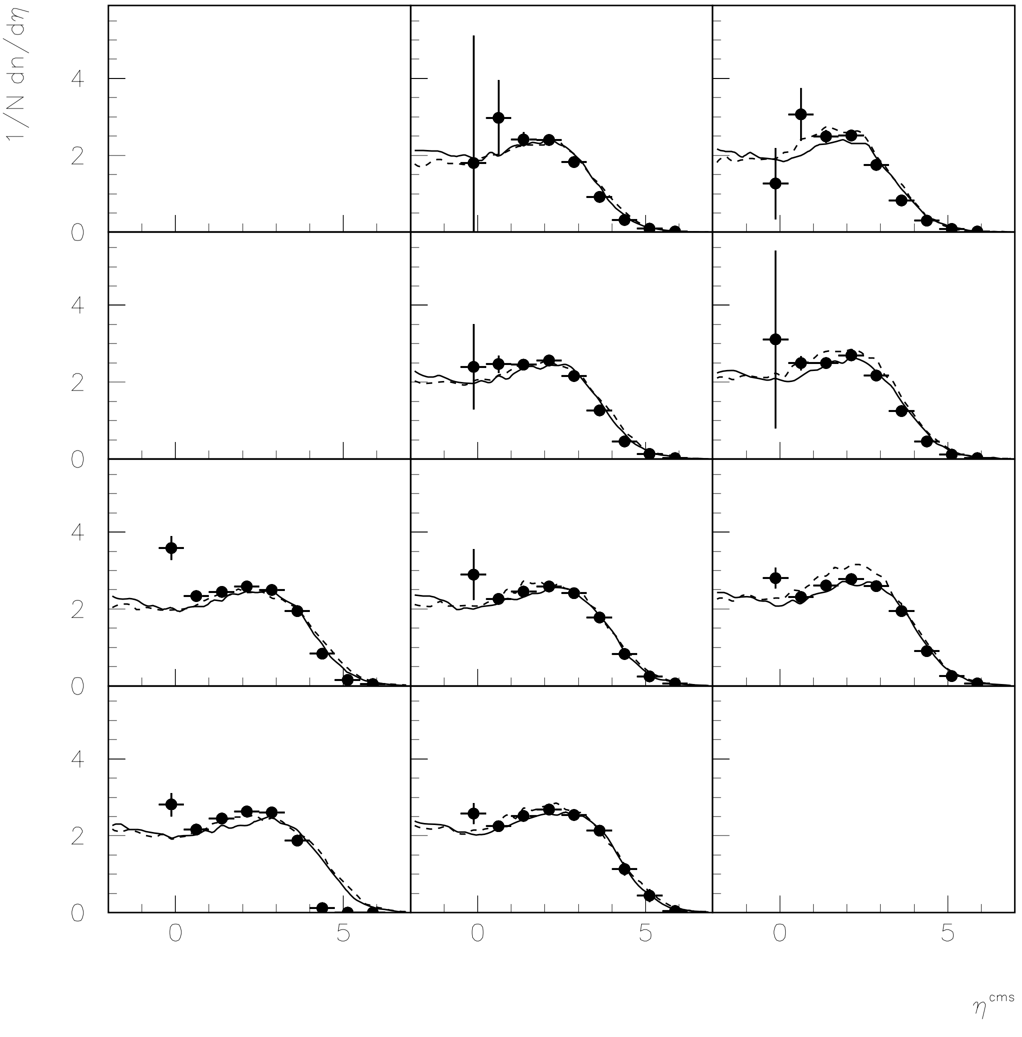

Figure 5.4: Pseudorapidity distributions of tracks in the CMS frame displayed in the same 9 x, Q^2 ranges as the transverse momentum spectra. Data(points) are shown superimposed on the CDM(full line) and MEPS(dashed line) Monte Carlo predictions.

Low p_T	0.0	0.2	0.4	0.6	0.8	1.0	1.2	1.6	2.1	3.0
High p_T	0.2	0.4	0.6	0.8	1.0	1.2	1.6	2.1	3.0	5.0
Generated p_T bin	Reconstructed p_T bin - all track types									
	1	2	3	4	5	6	7	8	9	10
1	10244	979	57	33	10	5	5	5	6	3
2	818	28091	848	66	25	10	9	3	3	6
3	174	944	17704	692	42	20	30	6	6	4
4	70	78	611	9596	412	18	10	5	1	3
5	36	45	35	333	5209	318	21	7	3	2
6	18	22	12	14	185	2965	191	10	2	1
7	10	15	9	8	14	123	3336	148	5	3
8	5	8	2	5	2	2	60	1815	70	6
9	1	4	2	2	1	3	5	45	1139	36
10	2	4	1	0	0	0	0	0	25	525
> 5 GeV/c	0	0	0	0	0	0	0	0	0	12
Bin Purity	90%	93%	92%	89%	88%	86%	91%	89%	90%	87%

Table 5.2: Migration matrix produced from a Monte Carlo sample using all tracks passing the track selection. The minimum and maximum p_T for each bin are shown in GeV/c.

5.4 Systematic Errors

As well as the statistical errors, various systematic errors have been added in quadrature. These have been evaluated in different ways - by altering constraints in the event selection criteria, by altering constraints in the track selection criteria and by altering parameters in the simulation.

5.4.1 Varying the Forward Track Selection Through the R0 Constraint

The quality of forward tracks selected for analysis is sensitive to variation of the R0 constraint, which essentially requires the track to point to the vertex. A significant problem in selecting forward tracks is that a large number of secondary particles produce background signals which may confuse the measurement of primary tracks originating at the collision vertex. The secondaries arise mainly from two sources, interactions of primary particles with the material within the detector system, for example in the end-wall separating the CTD from the FTD, and also from a beam collimator “C4” situated roughly central within the FTD

Low p_T	0.0	0.2	0.4	0.6	0.8	1.0	1.2	1.6	2.1	3.0
High p_T	0.2	0.4	0.6	0.8	1.0	1.2	1.6	2.1	3.0	5.0
Generated p_T bin	Reconstructed p_T bin - forward tracks only									
	1	2	3	4	5	6	7	8	9	10
1	5126	1068	111	25	12	6	4	3	7	3
2	785	5262	552	72	34	7	13	5	6	2
3	154	607	2686	338	37	11	15	2	6	2
4	99	110	434	1239	220	22	10	10	3	1
5	51	39	53	268	602	131	18	2	5	1
6	36	17	16	29	169	259	90	8	5	2
7	21	15	10	9	18	110	267	45	5	7
8	6	2	0	3	4	6	46	102	28	3
9	3	2	0	0	0	0	4	20	62	8
10	1	1	0	0	0	0	0	0	5	20
> 5GeV/c	1	0	0	0	0	0	0	0	0	1
Bin Purity	82%	74%	70%	62%	55%	47%	57%	52%	47%	40%
Purity Error	2%	1%	2%	2%	3%	4%	4%	6%	7%	11%

Table 5.3: Migration matrix produced from a Monte Carlo sample of just forward tracks passing the track selection. The minimum and maximum p_T for each bin are shown in GeV/c. Because of low statistics in some of the bins the statistical error on the purity is also shown.

Track Types	Central Tracks	Combined Tracks	Forward Tracks
Kinematic bin 1	94%	6%	0%
Kinematic bin 2	89%	9%	2%
Kinematic bin 3	93%	6%	1%
Kinematic bin 4	83%	12%	5%
Kinematic bin 5	61%	21%	18%
Kinematic bin 6	39%	23%	38%
Kinematic bin 7	91%	7%	2%
Kinematic bin 8	71%	18%	11%
Kinematic bin 9	41%	21%	38%

Table 5.4: Table showing relative contributions of the CTD and FTD in the pseudorapidity range $0.5 < \eta^{cms} < 1.5$ and in the 9 kinematic bins where transverse momentum spectra are presented.

Track Types	Central Tracks	Combined Tracks	Forward Tracks
Kinematic bin 1	35%	22%	43%
Kinematic bin 2	23%	20%	57%
Kinematic bin 3	28%	23%	49%
Kinematic bin 4	14%	12%	74%
Kinematic bin 7	25%	18%	57%

Table 5.5: Table showing relative contributions of the CTD and FTD in the forward pseudorapidity range $-0.5 < \eta^{cms} < 0.5$ and in the 5 kinematic bins where transverse momentum spectra are presented.

and causing secondaries to spray upwards into the FTD. This problem may be minimised by vetoing tracks which are not directed clearly towards the collision vertex. The quantity used to do so is R0, the normal distance from the vertex of the circle described in the x-y plane by the extrapolated forward track. The default track selection used requires $R0 < 5.0$ cm. By constructing p_T-spectra with this constraint doubled and halved to 10.0 cm and 2.5 cm and subtracting from the spectra produced with the default track selection a bin-by-bin systematic error was arrived at. In each case the spectra arising from data were corrected using Monte Carlo employing identical selection. This is a check on how loosening and tightening of the track selection criteria affects the final p_T-spectra.

5.4.2 Varying the Central Track Selection Through the DCA Constraint

A similar procedure is followed in order to constrain central tracks to originate near the vertex. The distance of closest approach(DCA) of the vertex perpendicular to the projected central tracks is calculated and the default track selection requires this quantity to be less than 2.0 cm. In order to evaluate to what extent the spectra are sensitive to this parameter a bin-by-bin systematic error was evaluated by calculating the difference between the corrected spectra formed employing the default track selection and those formed requiring DCA to be less than 1.0 cm.

5.4.3 Altering the Number of Forward Planar Segments

Another method of improving forward track selection quality was the requirement of at least two planar segments instead of one on each track.

Each planar chamber, contributing to each of the three FTD supermodules, individually again consists of three “orientations” which divide the planar chamber into layers in the z-direction. The orientations consist of four wire planes perpendicular to the z-axis and separated in the z-direction. Within a given wire plane the wires run parallel to eachother but the three different orientations have their wire-directions rotated by 60 degrees with respect to one another. The four wire planes in an orientation all have their wires parallel with groups of four wires separated in z housed together in a cuboid drift box.

Tracks are reconstructed from “segments” which are groups of signals indicative of a line of ionisation through the three orientations forming a planar chamber[37]. Since there is no charge division, signals in at least two orientations are required in order to define a line segment. The third orientation is needed to reduce the large hodoscope ambiguity. Within a given orientation at least three out of a possible four hits are needed in order to resolve the drift sign ambiguity, the sense wires being slightly staggered in alternating directions perpendicular to the central axis. A primary planar segment is defined by at least three hits in all three orientations. After all primary segments are isolated the remaining hits are used to form all possible combinations with two orientations containing at least three hits each. These are extrapolated into the missing orientation and if one or two hits are found there this collection is dubbed a secondary segment. All remaining intersections of two orientations are labelled tertiary segments. While primary segments are immediately considered tracks, secondary segments are also quite reliable but tertiary segments might well be random coincidences.

Primary and secondary segments, even if unattached to other segments, are treated as tracks. However, tertiary segments are only used when associated with tracks already containing a primary or secondary planar segment identified in another supermodule. In order to further improve the forward track quality the minimum number of forward planar segments required by the track selection was increased to two. This reduced forward track statistics by 40-50% but reduced bin migration.

The difference between corrected spectra formed employing a forward track selection requiring two planar segments and those employing spectra formed from one requiring only one planar segment was calculated on a bin-by-bin basis and used as an additional systematic error.

5.4.4 Varying the Forward Track Selection Through a χ^2 Constraint

In fitting a track as best as possible through the points identified in the detectors, residuals are combined to form a χ^2 quantity. This should reasonably match the number of degrees of freedom(d.o.f.) of the fit. The default track selection employs a loose constraint on the χ^2 per d.o.f. requiring it to be less than 25.0. The difference in corrected spectra formed employing the default track selection and those formed requiring the χ^2 per d.o.f. to be less than 15.0 was calculated and employed on a bin-by-bin basis as a further systematic error.

5.4.5 Varying the Combined Track Selection Through a χ^2 Constraint

As well as tracks measured solely in the Forward Tracking Detector or the Central Tracking Detector there are some tracks which pass through both. An attempt is then made to combine such tracks and obtain a better measurement of the particle which produced the signals. There is a constraint on the χ^2 quantity associated with the linking procedure. The χ^2 per d.o.f. is constrained by default to be less than 15.0. The difference between corrected spectra produced employing the default track selection and those produced using a constraint of 10.0 instead was calculated on a bin-by-bin basis and provides another systematic error in this analysis.

5.4.6 Uncertainty in the BEMC Energy Scale

During the 1994 running period there was an uncertainty in the BEMC energy scale evaluated to be 1.6%. Since the scattered positrons for the data selected for this analysis were measured in the BEMC, and these measurements used to calculate x, Q^2 and the boost to the CMS frame, this influences the results. In order to evaluate the systematic error arising from this uncertainty the measured positron energy was altered artificially by ± 1.6%. The consequent spectra were subtracted from the default spectra and the largest of the resulting differences used as systematic errors on a bin-by-bin basis.

5.4.7 Altering the Scattered Positron Energy Constraint to Account for Uncertainty in Photoproduction Contribution

At low Q^2 photoproduction($Q^2 \approx 0$) events dominate the cross-section and, since the hadronic debris from such events may enter the BEMC and possibly fake a scattered positron, photoproduction is a source of unwanted background in the DIS sample. In order to evaluate the associated systematic error the constraint on minimum scattered positron energy was varied from a nominal 12 GeV to 14 GeV where it is known that photoproduction background is negligible. The

x, Q^2 bin	1	2	3	4	5	6	7	8	9
No. +ve Tracks	15819	20748	32592	24138	24692	11379	29948	21847	9084
No. -ve Tracks	15429	20254	31740	23672	24038	11080	29632	21248	8932
Difference	2.5%	2.4%	2.6%	1.9%	2.6%	2.6%	1.1%	2.7%	1.7%

Table 5.6: Balance of positive and negative track populations across the 9 x, Q^2 bins.

resulting spectra were subtracted from the default distributions to arrive at a bin-by-bin systematic error.

5.4.8 QED Radiation

It is possible that the emission of a photon from the positron could alter the results since, particularly in the case of initial state radiation, the incident positron energy might be altered to such an extent that kinematic quantities calculated assuming an incident positron energy of 26.7 GeV would be erroneous. In general any final state QED radiation would tend to be almost collinear with the recoiling positron and consequently would tend to be detected along with the e^+, so preserving the measurement of the recoil positron energy. This was shown to be a negligible effect by incorporating the Django program[26]. A corresponding small systematic error has been added by calculating the difference in p_T-spectra produced using Django with and without QED radiation and on a bin-by-bin basis.

5.4.9 Differences Between Positive and Negative Tracks

Numbers of positive and negative tracks entering the 9 x, Q^2 bins were found to be roughly balanced and are tabulated in table 5.6. The overall p_T-spectra produced from positive tracks only are consistent with those produced from negative tracks only. A corresponding systematic error has been added on a bin-by-bin basis to reflect any small differences between the p_T-spectra produced from negative tracks alone and those produced from positive tracks alone. The differences between the corrected default spectra and the single charge-sign spectra corrected using Monte Carlo reconstructed level single charge-sign spectra were calculated for each p_T-bin individually and the largest of the two charge-sign differences was chosen as a systematic error contribution for a given p_T-bin.

5.5 Summary of Contributions to the Error Measurement

Table 5.7 presents the contributions to the total error as percentages of the signal which have been calculated individually on a bin-by-bin basis. These contributions are tabulated for each of the η^{cms} ranges for which p_T-spectra are presented. The different contributions, added together in quadrature to form the total error, are the statistical error, the systematic error to take into account differences in forming spectra from oppositely charged tracks, the systematic error indicating the spread in correction factor when formed from different Monte Carlo types, the systematic error associated with varying the number of forward track planar segments requirement, the systematic error to take into account photoproduction background, the systematic error to take into account QED radiation, the systematic error to take into account uncertainty in BEMC energy scale, the systematic error associated with variation of the forward track χ^2 constraint, the systematic error arising from altering the track selection R0 constraint, that from altering the DCA constraint and the systematic error arising from variation of the combined track χ^2-link requirement.

In each η^{cms} range the statistical error rises steadily with p_T since the bin populations are falling. In fact this also affects the calculation of the sytematic errors since they are evaluated on a bin-by-bin basis according to the difference in signal of the default spectra and comparison spectra whose highest p_T-bins tend to have a large error due to low statistics. This means that the systematic errors attached to the highest p_T-bins are less well-known. The percentage contributions presented in Table 5.7 indicate the range over the whole p_T-spectrum and across all x, Q^2-bins but may neglect uncharacteristically high contributions in some of the individual bins. This is to give a better idea of the relative contributions of the various systematic errors evaluated. In any case, in forming the total errors of the p_T- spectra presented, these uncharacteristically high contributions have also been added in quadrature and are likely to be safe over-estimates.

The systematic error due to photoproduction background gains significance toward the low x, Q^2-bins which is indicated in the percentage ranges shown for the upper bound tabulated.

The systematic error associated with variation of the R0 requirement in the track selection is practically negligible except in the very lowest p_T-bins which might suffer from contamination of secondaries. Again, the lowest p_T-bin should be ignored since the track selection constraint on momentum falls effectively within this bin and renders the corresponding correction factors meaningless.

Pseudorapidity range	$-0.5 < \eta^{cms} < 0.5$	$0.5 < \eta^{cms} < 1.5$	$1.5 < \eta^{cms} < 2.5$
Statistical error	1-30%	1-20%	1-15%
Syst. error of charge sign	<15%	<10%	<5%
MC correction factor	<10%	<10%	<5%
# fwd. plan. segments	<10%	<10%	<5%
photoprod. background	<5-10%	<1-10%	<1-3%
QED radiation	<5%	<5%	<5%
BEMC energy scale	<5%	<5%	<5%
Forward track fit χ^2	<5%	<2%	<2%
Track selection R0	<1%	<1%	<1%
Track selection DCA	<1%	<1%	<1%
Combined track link χ^2	<1%	<1%	<1%

Table 5.7: Various contributions to the total error on the p_T-spectra presented as percentages of the signal in different ranges of η^{cms}.

5.6 Discussion

5.6.1 Transverse Momentum Spectra and Evidence Against DGLAP k_T-Suppression at Low x

Charged particle transverse momentum spectra, normalised to the number of events selected in the relevant x, Q^2-range, are presented in various η^{cms} ranges and within 9 bins of Bjorken-x and Q^2(see Figures 5.5, 5.6 and 5.7). The p_T-spectra are observed to fall off exponentially and are presented with a logarithmic ordinate scale. In each η^{cms} domain there is a clear preference of the data for Monte Carlo simulation employing the CDM description over that based upon the MEPS model. This preference is more pronounced towards the central region in η^{cms}, away from the current region. In the central pseudorapidity region DGLAP evolution would tend to suppress the transverse momentum. This preference is particularly emphatic towards low x where the MEPS Monte Carlo fails to describe the p_T-spectra. Statistical error bars were added in quadrature with systematic errors evaluated on a bin-by-bin basis. Where visible, the inner error bar represents the extent of the statistical error contribution to the total error.

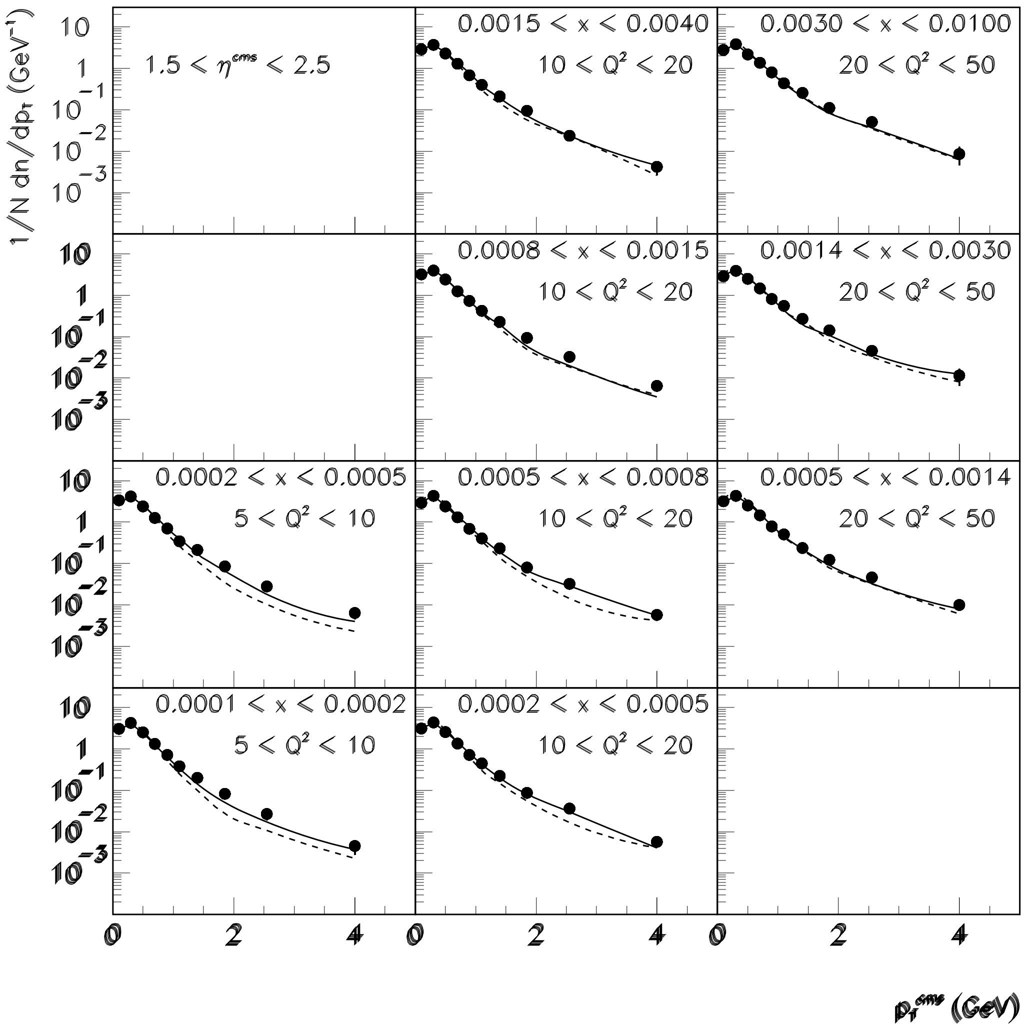

Figure 5.5: Transverse momentum spectra of charged tracks across the x, Q^2 range. Data are compared with CDM Monte Carlo(full line) and MEPS(dotted line). These plots were made in the pseudorapidity interval 1.5 to 2.5 in the CMS frame.

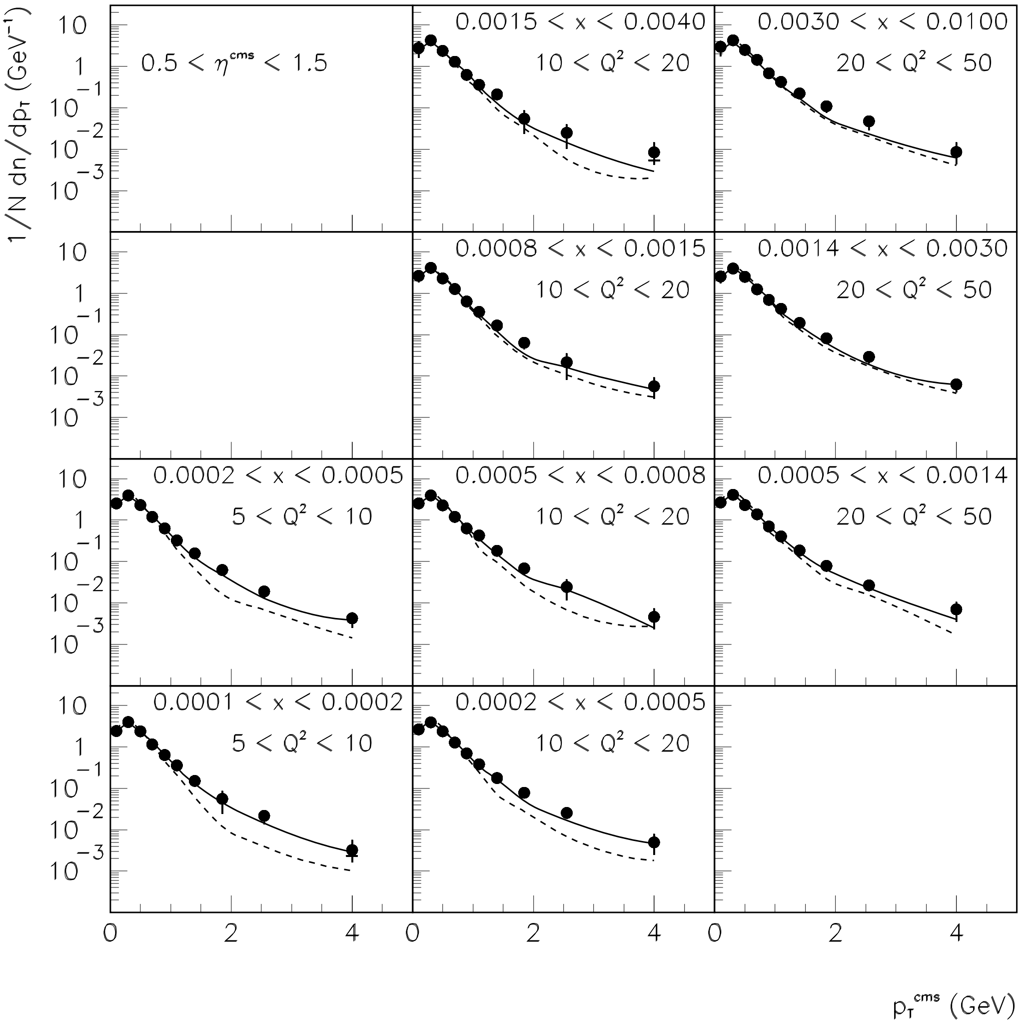

Figure 5.6: Transverse momentum spectra of charged tracks across the x, Q^2 range. Data are compared with CDM Monte Carlo(full line) and MEPS(dotted line). These plots were made in the pseudorapidity interval 0.5 to 1.5 in the CMS frame.

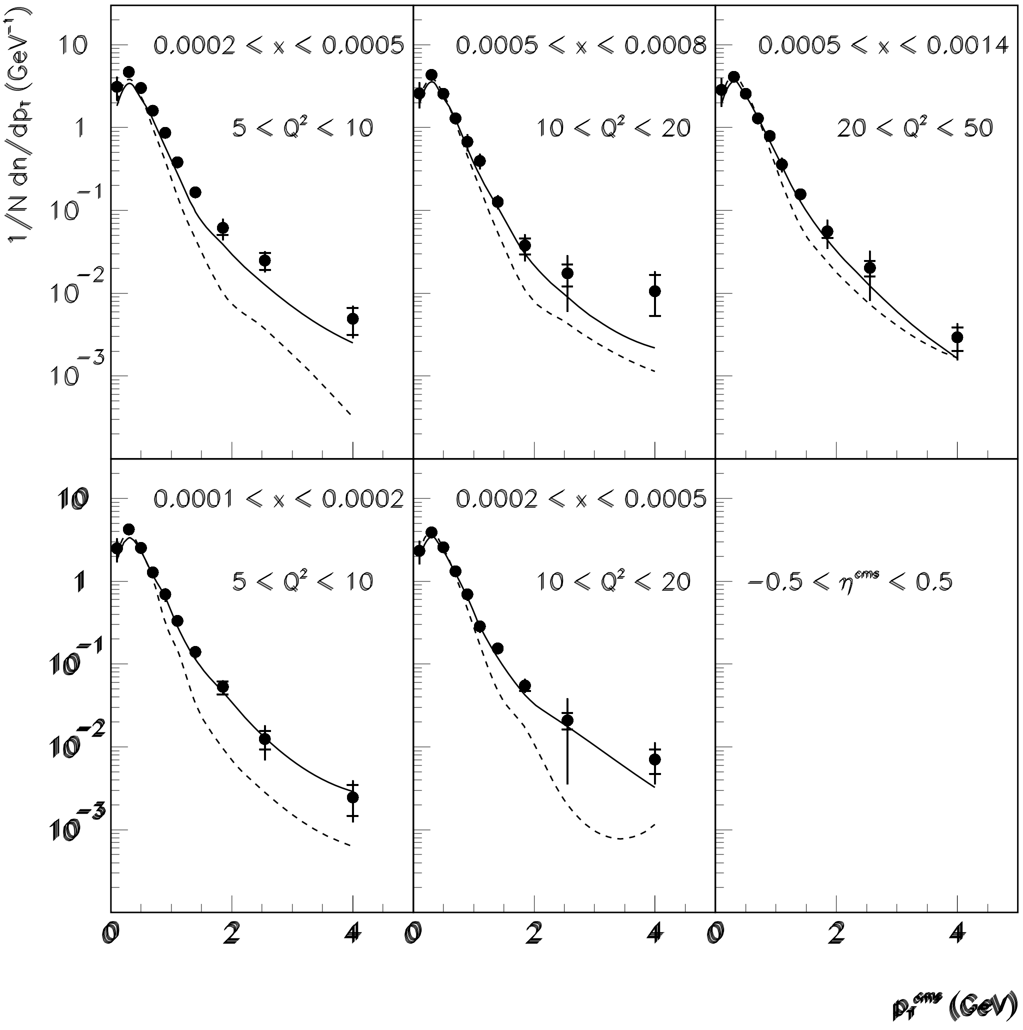

Figure 5.7: Transverse momentum spectra of charged tracks across the x, Q^2 range. Data are compared with CDM Monte Carlo(full line) and MEPS(dotted line). These plots were made in the pseudorapidity interval -0.5 to 0.5 central in the CMS frame.

5.6.2 Comparison of Transverse Momentum Spectra in Different Kinematic Regions

Transverse momentum spectra were compared between various kinematic bins in x, Q^2. Plots have been compared for tracks in the pseudorapidity range $1.5 < \eta^{cms} < 2.5$. Comparing regions of high and low x, differing by a factor 6 in x, at approximately the same $Q^2 \approx 14\, GeV^2$, it appears(see Figure 5.8) that the transverse momentum spectra were slightly harder towards low x, though only minimally so with little statistical significance. This might be understood as representative of increased gluonic activity at low x.

A further comparison was made between bins 2 and 7, between which Q^2 varies by a factor 3, from 9 to 29 GeV^2, while $W^2 \approx 32000\, GeV^2$ is held constant and large. It is observed that the transverse momentum spectrum becomes harder at large Q^2(see Figure 5.9).

A third comparison is presented between the transverse momentum spectra of bins 6 and 8, keeping $x \approx 0.0021$ roughly constant whilst doubling the magnitude of Q^2 from 15 to 32 GeV^2(see Figure 5.10).

5.6.3 Comparison with BFKL Calculation

Until recently no BFKL Monte Carlo has been generally available and the best method of investigating whether or not BFKL-like effects are observed was to compare data with the CDM Monte Carlo in juxtaposition with MEPS, noting the relevance of their different partonic k_T-ordering. However, the CDM Monte Carlo does not involve any resummation of $\log(1/x)$ terms which is fundamental to the BFKL description and any conclusions drawn must therefore be made carefully. Recently[12, 36], some BFKL-based calculations, incorporating next-to-leading order fragmentation functions provided by Binnewies et al[38], have become available which may be compared with the data presented here. In particular, the authors J.Kwiecinski, S.C.Lang and A.D.Martin recommend comparison in the range $-0.5 < \eta^{cms} < 0.5$. Such a comparison has now been performed with the utilisation of the Forward Tracking Detector and is presented in Figure 5.11. Traces showing a prediction with the BFKL resummation of $\log(1/x)$ terms switched on(upper trace) and off(lower trace)[12] are compared with p_T-spectra measured in the central CMS pseudorapidity range and in x, Q^2-ranges matching those of bins 1-3 defined earlier. It is easily noted that the data shows a marked preference for the BFKL calculations of bins 2 and 3. In bin 1 there is some ambivalence which is yet to be understood.

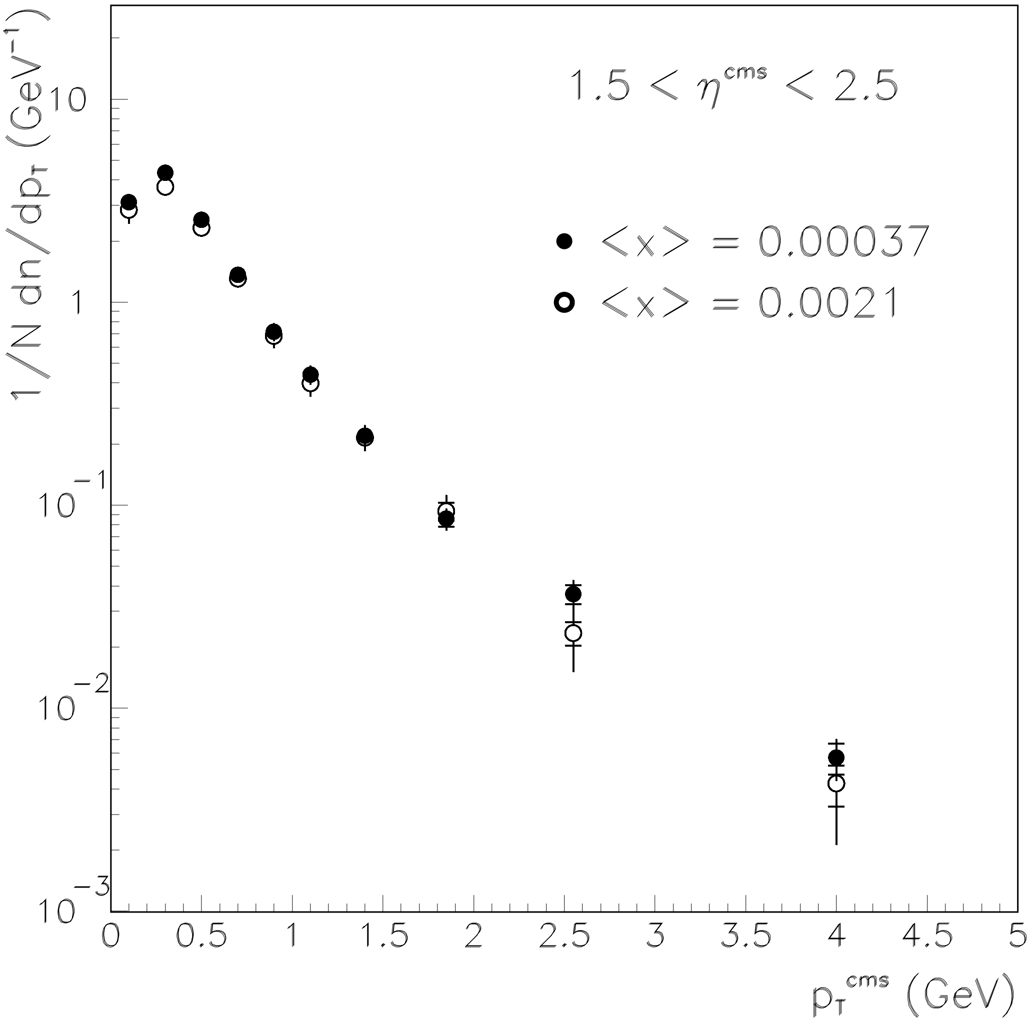

Figure 5.8: Comparison of p_T-spectra at high x (bin 6) and low x (bin3) for a fixed $Q^2 \approx 14\,GeV^2$

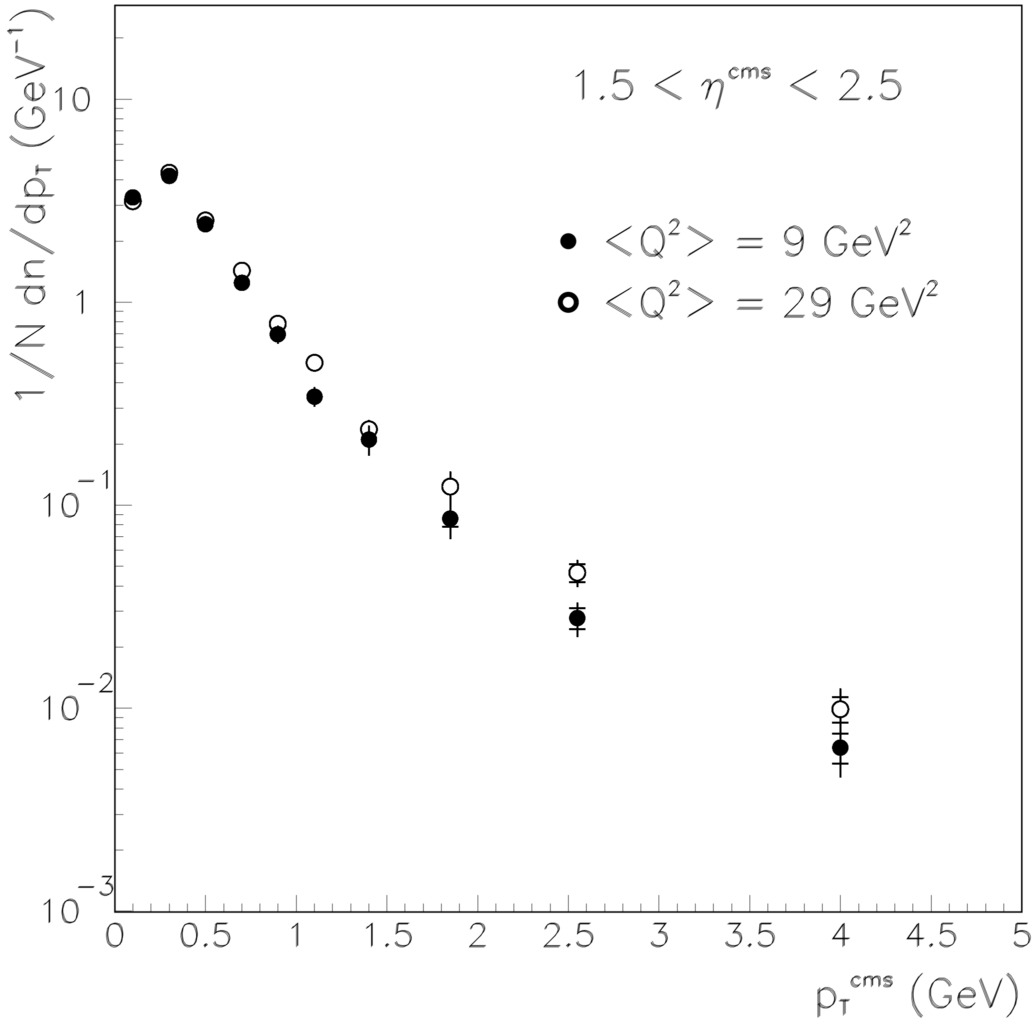

Figure 5.9: Comparison of p_T-spectra at different Q^2 values (bins 2 and 7) for fixed, large $W^2 \approx 32000\,GeV^2$

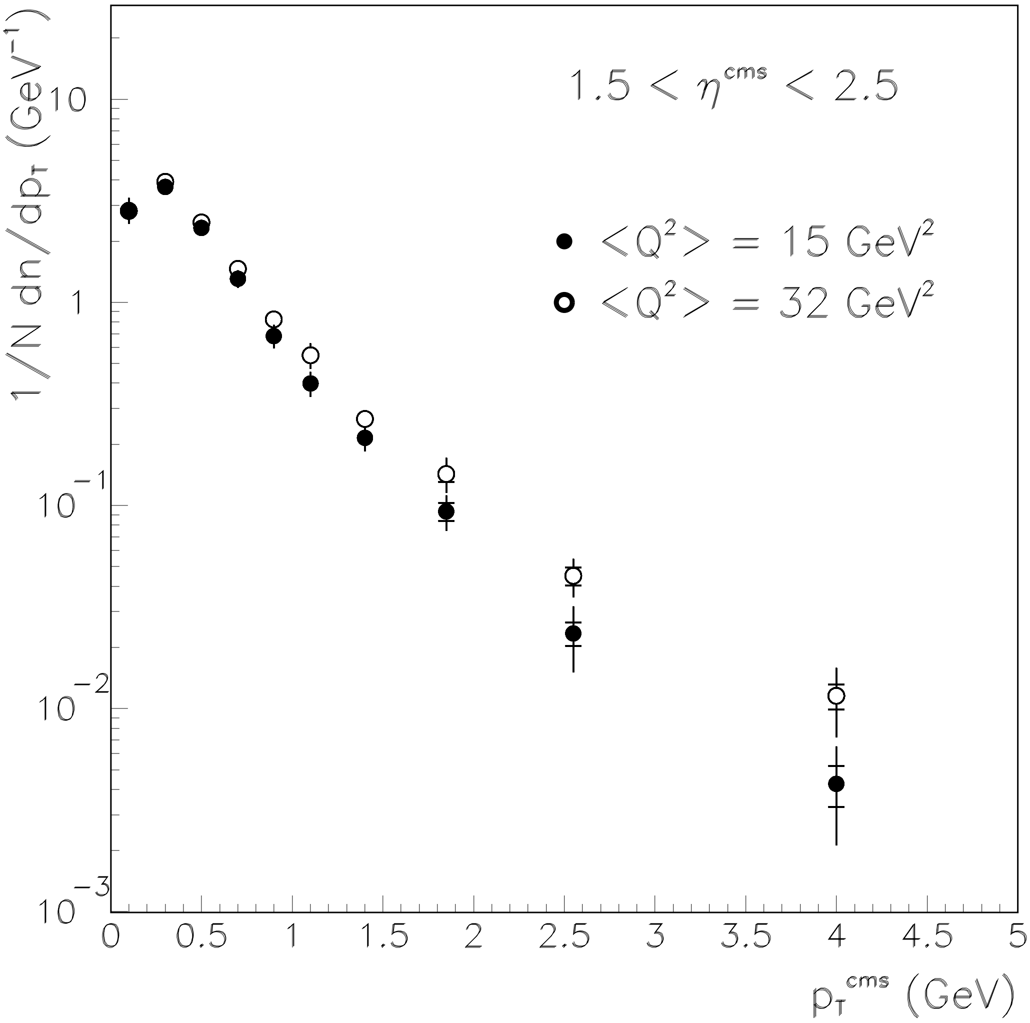

Figure 5.10: Comparison of p_T-spectra at different Q^2 values (bins 6 and 8) for fixed, large $x \approx 0.0021$

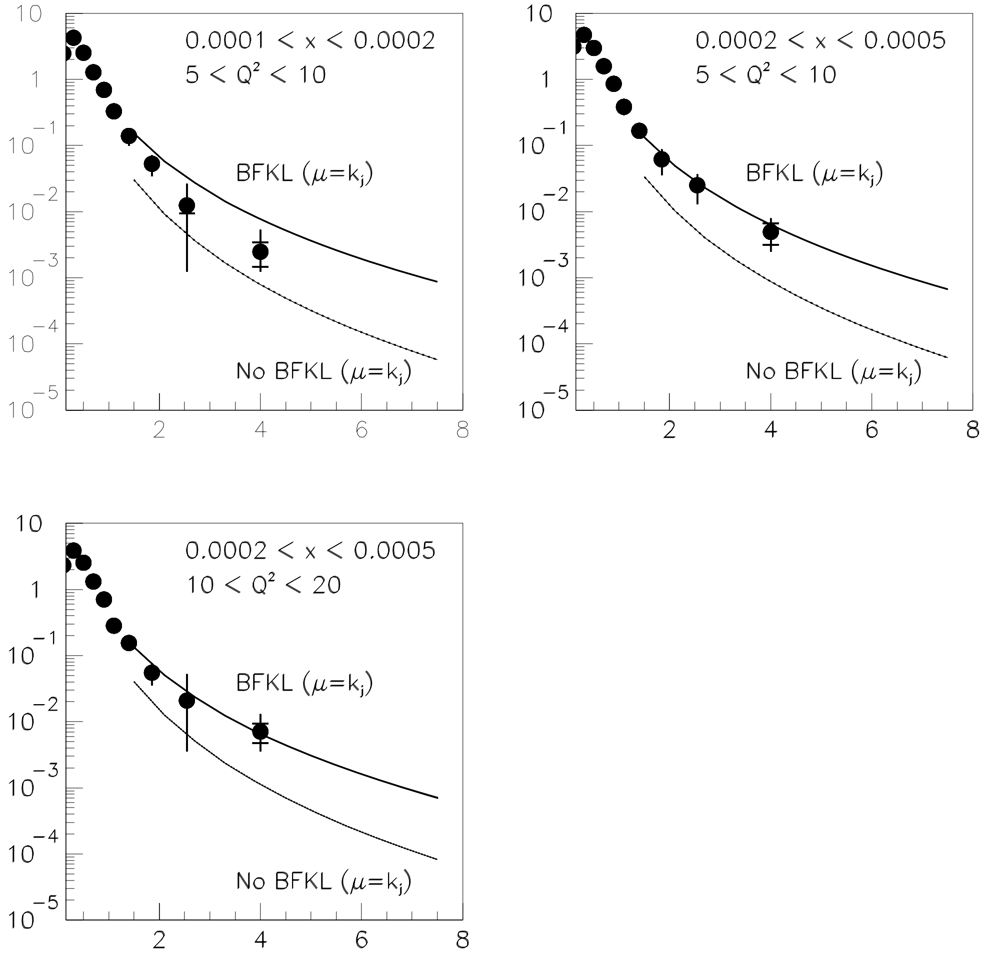

Figure 5.11: Comparison of H1 data with BFKL calculations made in the central CMS pseudorapidity range $-0.5 < \eta^{cms} < 0.5$, and in x, Q^2-bins 1-3.

Chapter 6

Conclusions

The Monte Carlo model based upon DGLAP parton showers fails to describe the data at low x.

The CDM model is similar to BFKL with respect to the non-ordering of partonic k_T and describes the p_T spectra of the data much better at low x. BFKL equations should become applicable at some low x value due to their resummation of $\alpha_S \log(1/x)$ terms. The question is have we reached these values at HERA?

Although in previous studies, of inclusive variables such as the structure function $F_2(x, Q^2)$ and transverse energy flow[17], MEPS has managed to describe the data at low x, it does not manage to describe p_T spectra in this regime. This may be understood by considering the distinction between hard partons likely to be emitted in a non-k_T-ordered partonic cascade. These are distinct from the abundant emission of low energy (soft) partons arising from the hadronisation process. The emission of such soft gluons will be of lesser significance to a high k_T initial parton, having less bearing on its ensuing 4-momentum and consequently upon the corresponding high p_T of a resulting leading charged hadron. Study of the high transverse momentum charged particles is a useful method to investigate the underlying parton dynamics because such particles are unlikely to arise exclusively from hadronisation effects.

Recent work elsewhere[36] purports to show a preference of charged particle p_T-spectra from previously published H1 data for a BFKL calculation in x, Q^2-bins identical to bins 1-3 in this analysis for tracks within the pseudorapidity range 0.5< η^{cms} <1.5 [1]. The authors of [36] recommend studying the range -0.5< η^{cms} <0.5 which has been accomplished here. The resulting comparison shows data favouring the BFKL calculation.

In order to make a measurement in this rapidity interval the FTD has been successfully employed in conjunction with the other detector systems available to the H1 experiment. The harsh conditions of tracking in the forward region, the rejection of secondaries and the identification of well-selected forward and combined tracks might be better accomplished with an upgraded FTD including further orientations and/or additional wire planes within planar chambers. This would lead to a greater efficiency of planar segment finding and therefore more efficient track selection. The subject of FTD upgrade is discussed elsewhere[39].

In summary, measurement of charged particle p_T-spectra in positron-proton collisions do not agree with MEPS Monte Carlo predictions in the regime of low Bjorken-x, whilst Colour Dipole Model predictions are consistent. A recent BFKL calculation also compares favourably with the data. It may be concluded that there is evidence that non-k_T-ordered partonic emission is being observed at HERA and this is broadly consistent with the predictions of Balitsky - Fadin - Kuraev - Lipatov low x QCD evolution.

References

[1] H1 Collaboration. "Measurement of Charged Particle Transverse Momentum Spectra in Deep Inelastic Scattering". *Nucl Phys B485*, 1997.

[2] Francis Halzen and Alan D. Martin. *Quarks and Leptons: an Introductory Course in Modern Particle Physics.* John Wiley and Sons, 1984.

[3] D.H.Perkins. *Introduction to High Energy Physics.* Addison Wesley, 1986.

[4] D.Griffiths. *Introduction to Elementary Particles.* J.Wiley and Sons, 1987.

[5] Y.L.Dokshitzer V.A.Khoze, A.H.Mueller and S.I.Troyan. *Basics of Perturbative QCD.* Editions Frontieres, 1991.

[6] G.Miller et al. "Inelastic Electron-Proton Scattering at Large Momentum Transfers". *Phys. Rev. D*, 5(1972)528.

[7] Greiner and Schaeffer. *Quantum Chromodynamics.* Springer, 1995.

[8] V.N.Gribov and L.N.Lipatov. *Soviet Journal of Nuclear Physics*, 15(1972)438.

[9] L.N.Lipatov. *Soviet Journal of Nuclear Physics*, 20(1975)95.

[10] G.Altarelli and G.Parisi. *Nucl.Phys.B*, 126(1977)298.

[11] Y.L.Dokshitzer. *Soviet Phys. JETP*, 46(1977)641.

[12] S.C.Lang. *Studies of Final States in Small x Deep Inelastic Scattering.* PhD thesis, University of Durham, September 1997.

[13] M.Ciafaloni. *Nucl.Phys.*, B296(1987)259.

[14] F.Fiorani S.Catani and G.Marchesini. *Nucl.Phys.*, B336(1990)18.

[15] E.A.Kuraev L.N.Lipatov and V.S.Fadin. *Phys. Lett. B*, 60(1975)50.

[16] Y.Y.Balitsky and L.N.Lipatov. *Soviet Journal of Nuclear Physics*, 28(1978)822.

[17] H1 Collaboration. "Transverse Energy and Forward Jet Production in the Low x Regime at HERA". *Phys.Lett.*, B356(1995)118.

[18] M.N.Rosenbluth A.H.Teller N.Metropolis, A.W.Rosenbluth and E.Teller. "Equation of State Calculations by Fast Computing Machines". *Journal of Chemical Physics*, 21(1953)1087-1092.

[19] A.Vogt M.Glück, E.Reya. "Dynamical Parton Distributions of the Proton and Small-x Physics". *Z.Phys.C67*, 433-448,1995.

[20] A.Vogt M.Glück, E.Reya. "Dynamical Parton Distributions Revisited". *hep-ph/9806404*, 1998.

[21] A.Edin G.Ingelman and J.Rathsman. "Lepto 6.5 - A Monte Carlo Generator for Deep Inelastic Lepton-Nucleon Scattering". *Comput. Phys. Commun.*, 101(1997)108-134.

[22] Leif Lonnblad. "Ariadne Version 4: A Program for Simulation of QCD Cascades Implementing the Color Dipole Model". *Comput. Phys. Commun.*, 71(1992)15-31.

[23] H.Kharriza and L.Lönnblad. Ldcmc version 1.0. *LU-TP 97-34*, 1997.

[24] H.Kharriza and L.Lönnblad. The Linked Dipole Chain Monte Carlo. *JHEP03*, (1998)006.

[25] T.Sjöstrand. *Computer Phys. Commun.*, 82(1994)74.

[26] H.Spiesberger K.Charchula, G.A.Schuler. "Combined QED and QCD Radiative Effects in Deep Inelastic Lepton Proton Scattering: the Monte Carlo Generator DJANGO6". 1994.

[27] H1 Collaboration. "The H1 Detector at DESY". *Nucl. Instr. and Meth. A386*, 1997.

[28] F.Sauli. "Principles of Operation of Multiwire Proportional and Drift Chambers". *CERN-77-09*, 1977.

[29] S.Burke et al. "Track finding and fitting in the H1 Forward Track Detector". *Nucl. Instr. and Meth.*, A373:227–260, June 1995.

[30] J.Ban et al. "The BEMC Single Electron Trigger". *H1 Internal Note*, H1-07/92-235, July 1992.

[31] BEMC Group. "The H1 Backward Electromagnetic Calorimeter(BEMC)". *H1 Internal Note*, H1-08/92-233, August 1992.

[32] J.P.Phillips. *Deep Inelastic Structure of Diffraction.* PhD thesis, Univ. of Manchester, 1995.

[33] G.Bernardi(Ed.). "'HERA01.H1REC.DOC' and files therein". *DESY central IBM*, 1993.

[34] T.Ebert. *Hadronic Energy Flow in Deep Inelastic Electron Proton Scattering and Proton Structure at Low Bjorken x.* PhD thesis, University of Liverpool, 1995.

[35] J.Meyer(Ed.). "'HERA01.H1SIM.GUIDE'". *DESY central IBM*, 1991.

[36] A.D.Martin J.Kwiecinski, S.C.Lang. "Single Particle Spectra in Deep Inelastic Scattering as a Probe of Small x Dynamics". *hep-ph/9707240*, 1997.

[37] S.Burke. "How to Use Forward Tracks". *H1 Internal Note*, 1993.

[38] B.A. Kniehl J.Binnewies and G.Kramer. *Phys. Rev.*, D52(1995)4947.

[39] H1 Collaboration. "Proposal to Upgrade the H1 Forward Track Detector". *Proposal 750*, 1998.